Spatio-temporal pattern formation in reaction-diffusion systems coupled with convection and geometrical effect

Hiroyuki KITAHATA

Abstract

To understand how living organisms maintain their lives, it is important to regard the living organisms as nonequilibrium open systems, since organisms live through the dissipation of the chemical energy of the nutrition. So far, a number of studies on physics under nonequilibrium open conditions have been performed both experimentally and theoretically. Among these studies, spatio-temporal self-organization has been one of the most interesting topics. As a theoretical model of spatio-temporal pattern formation, reaction-diffusion systems are widely adopted. Under the framework of such a reaction-diffusion system, spontaneous pattern formation can be generated theoretically. So far a number of experimental, numerical, and theoretical studies have been performed on reaction-diffusion systems.

Reaction-diffusion equations can be adopted only when the field is fixed. Thinking of the phenomena in the real world, however, the field itself usually moves. We introduce this effect by adding the advection term to the reaction-diffusion equation. It can be said that this is the natural extension of the reaction-diffusion system. In this thesis, the mutual coupling between pattern formation in reaction-diffusion systems and convective flow is investigated. As the scales of the flow velocity and propagating-wave velocity are comparable, the novel phenomena can be seen both experimentally and theoretically.

On the other hand, in the theoretical studies, the boundary effects are rarely considered. In order to discuss on the pattern formation such as a target pattern, a spiral pattern, etc., there is no need to think about the boundary. In these studies, the effects of boundaries should be avoided and a lot of efforts have been made to eliminate the boundary effects. In the real world, however, the boundary of the field often affects the behavior of the whole system. If the typical scale of the system is comparable to the characteristic length of the pattern, the boundary effect is quite large.

Thus, the main topics in this thesis are the convective flow coupled with reaction-diffusion systems and boundary effects on reaction-diffusion systems. These two effects are important in order to understand the phenomena in the real world. In this thesis some experimental results are exemplified and theoretical discussion and/or numerical modeling are made for each system from the viewpoint of the reaction-diffusion systems with convective and/or boundary effects.

This thesis is based on the following original papers. The chapters which include the contents of the papers are indicated:

Published papers

[1]   H. Kitahata, R. Aihara, N. Magome, and K. Yoshikawa, Convective and periodic motion driven by a chemical wave, *J. Chem. Phys.*, **116**, 5666 - 5672 (2002): Chapters 3 and 4.

[2]   H. Kitahata, Spontaneous motion of a droplet coupled with a chemical reaction, *Prog. Theor. Phys. Suppl.*, in press: Chapter 4.

[3]   H. Kitahata, S. Hiromatsu, Y. Doi, S. Nakata, and M. R. Islam, Self-motion of a camphor disk coupled with convection, *Phys. Chem. Chem. Phys.*, **6**, 2409 - 2414 (2004): Chapter 5.

[4]   H. Kitahata and K. Yoshikawa, Chemo-mechanical energy transduction through interfacial instability, *Physica D*, **205**, 283 - 291 (2005): Chapter 6.

[5]   H. Kitahata, R. Aihara, Y. Mori, and K. Yoshikawa, Slowing and stopping of chemical waves in a narrowing canal, *J. Phys. Chem. B*, **108**, 18956 - 18959 (2004): Chapter 7.

[6]   H. Kitahata, A. Yamada, S. Nakata, and T. Ichino, Propagation of photo-sensitive chemical waves on the circular routes, *J. Phys. Chem. A*, **109**, 4973 - 4978 (2005): Chapter 9.

Reference papers

[7]   H. Kitahata, N. Magome, and K. Yoshikawa, Convective flow driven by chemical reaction, *Proc. Slow Dyn. Compl. Sys. (AIP Proc.)*, **708**, 430 - 431 (2004): Chapter 3.

[8]   S. Nakata, Y. Doi, and H. Kitahata, Synchronized motion of a mobile boundary driven by a camphor fragment, *J. Colloid. Interface. Sci.*, **279**, 503 - 508 (2004): Chapter 5.

[9]   S. Nakata, S. Hiromatsu, and H. Kitahata, Multiple autonomous motions synchronized with complex formation, *J. Phys. Chem. B*, **107**, 10557 - 10559 (2003): Chapter 6.

[10]   K. Nagai, Y. Sumino, H. Kitahata, and K. Yoshikawa, Mode selection in the spontaneous motion of an alcohol droplet, *Phys. Rev. E*, **71**, 065301 (2005): Chapter 6.

[11]   Y. Sumino, H. Kitahata, K. Yoshikawa, M. Nagayama, S.-i. M. Nomura, N. Magome, and Y. Mori, Chemo-Sensitive Running Droplet, *Phys. Rev. E*, **72**, 041603 (2005): Chapter 6.

[12]   H. Kitahata and K. Yoshikawa, Spatio-temporal pattern formation with oscillatory chemical reaction and continuous photon flux on a micrometre scale, *J. Phys.: Condens. Mat.*, **17**, S4239 - S4248 (2005): Chapter 6.

Contents

Part I

General Introduction

Chapter 1

Introduction

In this chapter, the perspective of this thesis is shown. The thesis includes mainly two topics: convective flow coupled with reaction-diffusion systems, and the boundary effects on reaction-diffusion systems. The importance of these two topics is depicted. Then, the outline of this thesis is presented.

1.1   Perspective

To understand how living organisms maintain their lives, it is important to regard the living organisms as nonequilibrium open systems, since organisms live through the dissipation of the chemical energy of chemical substances such as adenosine triphosphate (ATP) and so on [13,14]. So far, a number of studies on physics under nonequilibrium open conditions have been performed both experimentally and theoretically.

Among these studies, spatio-temporal self-organization has been one of the most interesting topics. As a theoretical model of spatio-temporal pattern formation, reaction-diffusion systems are widely adopted. In the framework of reaction-diffusion systems, it is assumed that the concentrations of chemical components or other physical quantities are defined at every point, i.e., local equilibrium is achieved, and the temporal changes in these physical quantities are described as the combination of the local dynamics (reaction) and transportation from/to the neighborhood proportional to the gradient (diffusion).

Typically, a reaction-diffusion equation for a N-component system is written as

$$\frac{\partial c_i}{\partial t} = f_i(c_1, c_2, \cdots, c_i, \cdots, c_N) + D_i \nabla^2 c_i, \tag{1.1}$$

where c_i is the physical quantity such as concentration of the chemical component, D_i is a diffusion constant and $f_i(c_1, c_2, \cdots, c_i, \cdots, c_N)$ is the summation of the local dynamics of the chemical reaction regarding the i-th component.

Under the framework of such a reaction-diffusion system, various spontaneous pattern formation can be predicted theoretically. A wave or wave packets

can propagate on the reaction field and forms fascinating patterns such as a target pattern or a spiral pattern. These patterns have been analytically studied based on the phase reduction, bifurcation theory, and so on [15,16]. On the other hand, Turing proposed a novel framework of pattern formation called a "Turing pattern"; i.e., a static pattern can be generated in a two-or-more-component system when the diffusion constants are quite different from each other [17].

There are also a large number of experimental systems which can be described as reaction-diffusion systems. Belousov-Zhabotinsky (BZ) reaction is one of them [18, 19]. The detailed introduction of BZ reaction is in Chapter 2. The oxidization pattern of carbon monoxide on platinum substrate [20], the pattern of combustion wave [21] or some other systems have also been studied. In these systems, the chemical wave propagation and/or spatio-temporal patterns can be observed. As for the Turing pattern, Ouyang et al. and de Kepper et al. have found the Turing patterns using the chemical reaction in the gel systems [22,23]. So far, there are many reports on the novel spatio-temporal pattern formation such as inward spirals [24], multiarm spirals [25], etc.

In the living organisms, it was said that the spatio-temporal self-organization is essential for the patterns on the animal skin, such as zebras, tigers and seashells [26]. Kondo et al. showed that the Turing pattern is seen in the pattern on the skin of a fish [27]. Today, many examples of such pattern formation in the living organisms have been found [28]. One of the most famous one is the pulse propagation on the nerve cells [29, 30]. It has been well established that, in cable-like nerve cells, pulses on the membrane propagate at a constant velocity and amplitude. With the physiological measurements, the phenomenological model called the Hodgkin-Huxley equation was established [29]. These equations are reduced to FitzHugh-Nagumo equation by adiabatic approximation [31–33]. The FitzHugh-Nagumo equation with a diffusion term has been widely used as a theoretical model for nerve systems. Therefore, reaction-diffusion systems are often used for a model of living organisms.

Reaction-diffusion equations, however, can be adopted only when the field is fixed. In the other words, the spatial transport is allowed only through diffusion. Thinking of the phenomena in the real world, the field itself usually moves. For example, the chemical reaction inside a cell should be affected by the protoplasmic streaming, and the solution in the reactor is often stirred. Thus, it is important to consider the motion of the field itself.

We introduce this effect by adding the advection term to the reaction-diffusion equation. It can be said that this is the natural extension of the reaction-diffusion system.

If the flow velocity and the typical scale of the change in the spatio-temporal pattern, such as the velocity of propagating chemical waves, are quite different, or if the typical length of the change in flow direction and the typical length of the pattern are quite different, there seems to be no interesting phenomena. For example, if the flow is much faster than the chemical wave propagation, the chemical components or other physical quantities are stirred, and become

uniform, which results in no pattern formation. If the flow direction is almost uniform throughout the system, there seems to be no effects on pattern formation but the pattern is transferred as a whole.

In this thesis, the mutual coupling between pattern formation in reaction-diffusion systems and convective flow are investigated. As the scales of the flow velocities and the propagating wave velocity are comparable, the novel phenomena can be seen both experimentally and theoretically. This coupling between reaction-diffusion systems and convective flow is the first topic in this thesis. The coupling between reaction-diffusion systems and convective flow can be regarded as an experimental model where chemical energy is transduced into mechanical motion.

On the other hand, in the theoretical studies, the boundary effects are rarely considered. In order to discuss on the pattern formation such as a target pattern, a spiral pattern, etc., there is no need to think about the boundary. In these studies, the effects of boundaries should be avoided and a lot of efforts have been made to eliminate the boundary effects.

In the real world, however, the boundary of the field often affects the behavior of the whole system. If the typical scale of the system is comparable to the characteristic length of the pattern, the boundary effect is quite important. In the experiments using BZ reaction, the change in the behavior in a narrow space was reported using a gel system [34, 35], a droplet system [36], a bead system [37, 38], etc.

As in the above paragraph, the nerve systems can be treated as reaction-diffusion systems. In recent years, based on the advances in experimental techniques, it is getting clearer that the manner of this pulse propagation critically depends on the thickness or width of the nerve cells. For example, it has been reported that the dendritic shape of nerve cells strongly affects the propagation of an excited wave [39–41].

In this thesis, thus, using BZ reaction as an experimental model, the boundary effects on chemical wave propagation are exemplified. The typical size of the system is around 100 μm to 1 mm, which corresponds to the typical width of one chemical wave. This boundary effects on reaction-diffusion systems are second topic in this thesis.

As a summary, the main topics in this thesis are the convective flow coupled with reaction-diffusion systems and boundary effects on reaction-diffusion systems. These two effects are important in order to understand the phenomena in the real world as reaction-diffusion systems. In this thesis, some experimental results are exemplified and theoretical discussion and/or numerical modeling are made for each system from the viewpoint of the reaction-diffusion systems with convective and/or boundary effects.

1.2   Outline of the thesis

In this section, the outline of this thesis is presented.

In Chapter 2, three important topics for discussion in this thesis are introduced: Reaction diffusion systems, BZ reaction, and Marangoni convection due to the surface tension difference.

This thesis includes mainly two topics: convective flow coupled with reaction-diffusion systems and boundary effects on reaction-diffusion systems. These two topics correspond to Parts II and III, respectively.

Part II includes four chapters. In Chapter 3, the convective flow induced by the repetitive change in interfacial tension in BZ reaction is exemplified. The characteristics of the convection are reproduced by numerical calculation based on the reaction-diffusion equations coupled with convection. The contents of this chapter are published in References [1] and [7]. In Chapter 4, the spontaneous motion of a droplet of BZ reaction medium is shown. The mechanism is discussed related to the convection inside the droplet. The contents of this chapter are published in References [1] and [2]. In Chapter 5, the spontaneous motion of a camphor grain is firstly discussed. Then, the convective flow induced by the surface tension gradient due to the nonuniform camphor layer on the water surface is exemplified, and numerically reproduced by the reaction-diffusion equation coupled with convection. At last, the effects of the convection to spontaneous motion are presented. The contents of this chapter are published in References [3], [8], and [4]. Chapter 6 includes three topics: the spontaneous motion of an alcohol droplet on the aqueous phase, the spontaneous motion of an oil droplet on a glass substrate in surfactant solution, and the spontaneous motion of a phenanthroline disk coupled with chemical reaction. These are the examples of spontaneous motion induced by the interfacial tension difference. The contents of this chapter are published in References [10], [11], [4], and [9].

Part III includes three chapters. In Chapter 7, the slowing and stopping of the chemical wave in the narrowing glass capillary is exemplified in BZ reaction. The mechanism is theoretically analyzed related to the surface-volume ratio. The contents of this chapter are published in References [5] and [12]. In Chapter 8, the narrowing reaction field is achieved by the designed illumination on photosensitive BZ reaction medium. The alternative disappearing of chemical waves is exhibited at a certain light intensity. In Chapter 9, the geometry of chemical wave propagating on a circular ring is studied. The two chemical waves on two connected circular rings are also discussed from the viewpoint of synchronization. The contents of this chapter are published in Reference [6].

The contents in this thesis are summarized and the future problems are shown in Part IV.

Chapter 2

Background

In this chapter, three topics are introduced, which are important for
the discussion in this thesis: Reaction-diffusion systems, Belousov-
Zhabotinsky reaction, and Marangoni convection induced by the sur-
face tension difference.

2.1 Reaction diffusion systems coupled with convection

In studies on spatio-temporal self-organization in nonequilibrium open systems,
reaction-diffusion systems are often used as representative model systems. The
advantage of a reaction-diffusion system is that spatio-temporal pattern forma-
tion can be described using simple equations regarding the dynamics of the local
concentrations of the chemicals. Thus, the dynamics of the system can be de-
scribed as the combination of the local dynamics and transportation from/to
the neighborhood proportional to the gradient, or diffusion.

The diffusion term is derived as follows. Diffusive flow $\mathbf{J}$ is assumed to
be proportional to the gradient of the concentration or some other physical
quantities, c,

$$\mathbf{J} \propto -\nabla c. \tag{2.1}$$

From the equation of continuity,

$$\frac{\partial c}{\partial t} = -\nabla \cdot \mathbf{J}, \tag{2.2}$$

the diffusion equation

$$\frac{\partial c}{\partial t} = D\nabla^2 c \tag{2.3}$$

is obtained, where D is a positive constant called a "diffusion constant".

On the other hand, the local dynamics of a chemical reaction can be described
using ordinary differential equations based on the mass-action law, which states

that the reaction rate is proportional to the product of the concentrations of the reactants.

Taking these two terms into consideration, a reaction-diffusion equation is derived:

$$\frac{\partial c}{\partial t} = f(c) + D\nabla^2 c, \tag{2.4}$$

where $f(c)$ is the dynamics of the chemical reaction. For an N-component system, this equation can be easily extended:

$$\frac{\partial c_i}{\partial t} = f_i(c_1, c_2, \cdots, c_i, \cdots, c_N) + D_i\nabla^2 c_i. \tag{2.5}$$

Under the framework of the reaction-diffusion systems, the local concentrations of the chemical reagents can be described only on a fixed field. In the real world, however, convective motion of the field is often observed: for example, as in the chemical reactions in a stirred solution and the biochemical reactions in cytoplasm. To consider this convective motion, an advection term should be introduced to the reaction-diffusion equations. The flow $\mathbf{J}$ at the point with a field velocity of $\mathbf{v}$ is

$$\mathbf{J} = -D\nabla c + c\mathbf{v}, \tag{2.6}$$

instead of eq. (2.1). Based on the conservation of the chemical components, the dynamics of c can be written as

$$\frac{\partial c}{\partial t} = D\nabla^2 c - \nabla \cdot (c\mathbf{v}). \tag{2.7}$$

Here, if the volume of the field is incompressive (for example, the reaction in a solution),

$$\nabla \cdot \mathbf{v} = 0, \tag{2.8}$$

the advection term can be written as $\mathbf{v} \cdot \nabla c$ instead of $\nabla \cdot (c\mathbf{v})$.

Overall, the dynamics of c in the incompressive field can be written

$$\frac{\partial c}{\partial t} = D\nabla^2 c - \mathbf{v} \cdot \nabla c. \tag{2.9}$$

By adding the local dynamics of the chemical reaction, or the reaction term, the reaction-diffusion-advection equations for the N-component system can be written as

$$\frac{\partial c_i}{\partial t} = f_i(c_1, c_2, \cdots, c_i, \cdots, c_N) + D_i\nabla^2 c_i - \mathbf{v} \cdot \nabla c_i. \tag{2.10}$$

This can be regarded as a reaction-diffusion-advection equation [12].

2.2　Belousov-Zhabotinsky reaction

Belousov-Zhabotinsky reaction (BZ reaction) is famous as an experimental model system for a reaction-diffusion system. In 1951, Belousov found the oscillatory

(a)   (b)

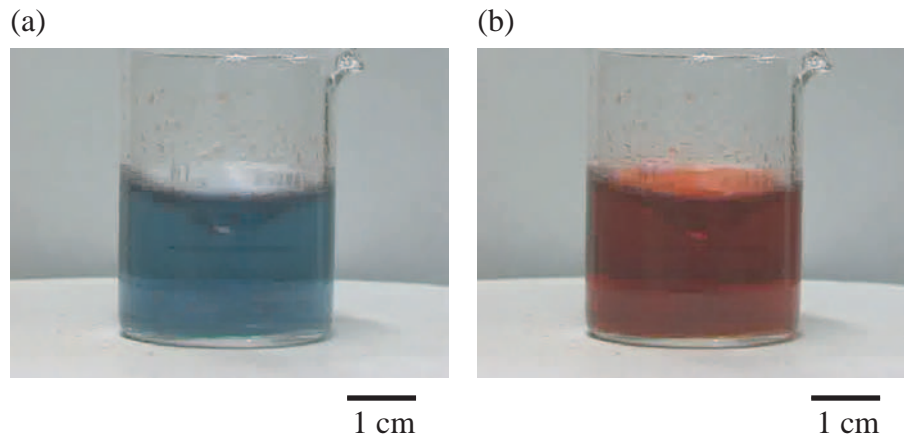
1 cm   1 cm

Figure 2.1: Rhythmic change in color in BZ reaction. When the solution is stirred, the solution oscillates between the (a) oxidized state (blue) and (b) reduced state (red).

behavior in color of the solution, when he made an experiments to make a model chemical system for metabolic pathways (TCA cycle). Belousov used citric acid as a reactant and cerium as a catalyst. In this reaction, the solution is changed between white and yellow. Unfortunately, Belousov's observation was not widely known, since people did not believe his experimental results. In 1964, Zhabotinsky used the catalyst of iron complex, i.e., ferroin, and reproduced Belousov's results. By using ferroin, the change in color is much easier to observe: the solution changes between red and blue as shown in Fig. 2.1. In 1970, he observed the spontaneous pattern formation in the solution, as BZ solution was allowed to stand [18]. For example, chemical waves propagate as concentric rings, or with a shape of spiral, which are called a target pattern, and a spiral pattern, respectively (Fig. 2.2) [19]. Then, Gáspár found that BZ reaction can be sensitive to the light intensity by using ruthenium complex as a catalyst $(Ru(bpy)_3^{3+})$ [42–45].

BZ reaction is an oscillatory chemical reaction between the oxidized state and reduced state. In the reaction process, an autocatalytic process is said to be the most important. This autocatalysis induces the nonlinearity in the chemical reaction, which enables chemical oscillation as a limit cycle oscillation in nonlinear systems.

There were a lot of studies on the mechanism of BZ reaction by considering all the elementary processes. In 1972, Field, Körös, and Noyes proposed that ten main processes are important for BZ reaction [46]. This model is called the FKN model. Based on this model, the kinetic equations on the concentrations of the products, reactants, and intermediates are derived, though this is so complicated. By adiabatic approximation on the fast processes, we can get a simpler model with a smaller number of variables.
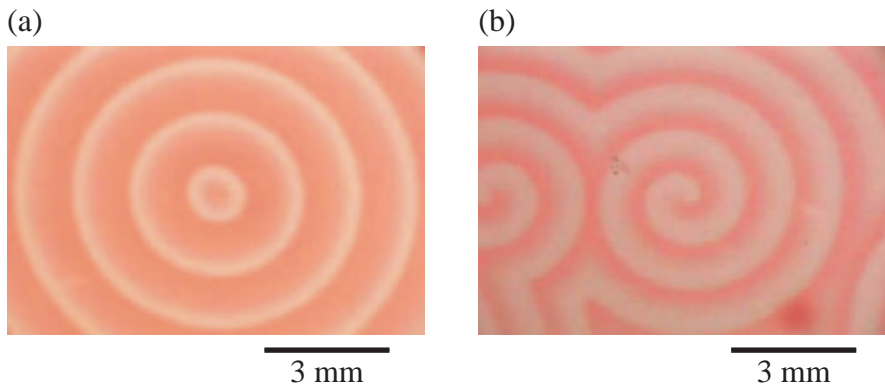
(a)   (b)

3 mm   3 mm

Figure 2.2: Spontaneous pattern formation in BZ reaction using ferroin as a cat-
alyst. (a) Target pattern. (b) Spiral pattern. Red and blue regions correspond
to the oxidized and reduced states, respectively.

Among the reduced models, the Oregonator has widely been used, which
was proposed by Field and Noyes. They assumed that the BZ solution takes
one of the two characteristic states: i.e., $HBrO_2$-rich state and $HBrO_2$-poor
state, where $HBrO_2$ is an unstable intermediate. In this model, the following
five chemical processes are important:

$$A + Y \xrightarrow{k_1} X + P, \tag{2.11}$$

$$X + Y \xrightarrow{k_2} 2P, \tag{2.12}$$

$$A + X \xrightarrow{k_3} 2X + 2Z, \tag{2.13}$$

$$2X \xrightarrow{k_4} A + P, \tag{2.14}$$

$$Z + B \xrightarrow{k_5} hY, \tag{2.15}$$

where A, B, P, X, Y, and Z correspond to BrO_3^-, $CH_2(COOH)_2+BrCH(COOH)_2$,
HOBr $HBrO_2$, Br^- and the oxidized catalyst, respectively. h is the parameter
which corresponds to the number of Br^- ions produced by one catalyst molecule
in the oxidized state.

Assuming that the temporal change in the concentrations of A and B is
negligible, the concentrations of A and B, i.e., A and B, can be set as constants.
Then, the kinetic differential equations for X, Y, and Z can be derived:

$$\epsilon \frac{dX}{dt} = k_1 AY - k_2 XY + k_3 AX - 2k_4 X^2, \tag{2.16}$$

$$\epsilon' \frac{dY}{dt} = -k_1 AY - k_2 XY + hk_5 BZ, \tag{2.17}$$

$$\frac{dZ}{dt} = 2k_3 AX - k_5 BZ, \tag{2.18}$$

where X Y and Z correspond to the concentrations of X Y   and Z, respectively. $k_i(i = 1 \cdot 5)$ are the reaction constants on each reaction (2.11) to (2.15) and ϵ and ϵ' are the positive small constants that correspond to the difference in the reaction rate. The above-mentioned differential equations are called the 3-variable Oregonator [47]

Since the temporal change in Y is much faster than the changes in X and Z, Y can also be reduced adiabatically, and the following model is obtained. This model is called the 2-variable Oregonator (Tyson version) [48]. Here, it is noted that X and Y is replaced by U and V, respectively.

$$\epsilon\frac{\mathrm{d}U}{\mathrm{d}t} = U(1 - U) - fV\frac{U - q}{U + q} \equiv F(U, V), \qquad (2.19)$$

$$\frac{\mathrm{d}V}{\mathrm{d}t} = U - V \equiv G(U, V), \qquad (2.20)$$

where U and V correspond to the concentrations of HBrO$_2$ and the oxidized catalyst, respectively. In other words, the region with larger V corresponds to the oxidized state (blue if using ferroin) and that with smaller V corresponds to the reduced state (red if using ferroin). f q and ϵ are the parameters that correspond to the threshold for excitation, excitability, and nondimensionalized reaction constant, respectively. The two-dimensional dynamical system with the equations (2.19) and (2.20) has one stable fixed point (excited state) or one unstable fixed point and one stable limit cycle (oscillatory state) depending on these parameters. For example, as the paremeter f is changed, a stable fixed point destabilizes and a limit cycle orbit comes out, i.e., the system exhibits Hopf bifurcation. The nullclines of the dynamical systems are shown in Fig. 2.3.

On the contrary, Rovinsky and Zhabotinsky also proposed another way of reduction [49]. This model is called the Rovinsky-Zhabotinsky model, which can be written as follows:

$$\epsilon\frac{\mathrm{d}U}{\mathrm{d}t} = U(1 - U) - 2q\alpha\frac{V}{1 - V}\frac{U - \mu}{U + \mu}, \qquad (2.21)$$

$$\frac{\mathrm{d}V}{\mathrm{d}t} = U - \alpha\frac{U}{1 - U}V, \qquad (2.22)$$

where U and V correspond to the concentrations of HBrO$_2$ and [Fe(phen)$_3$]$^{3+}$, respectively.

The difference between Rovinsky-Zhabotinsky model and Tyson version 2-variable Oregonator is the term of $\frac{U}{1-U}$. It is said that the BZ reaction with ferroin catalyst is reproduced better by the Rovinsky Zhabotinsky model, but in the present article, Tyson version 2-variable Oregonator is adopted. Figure 2.4 shows the results of numerical calculation on the pattern formation using Tyson version Oregonator.

So far, there have been a large number of studies on BZ reaction, since it is easily achieved by mixing a few chemical compounds, and easily controlled.
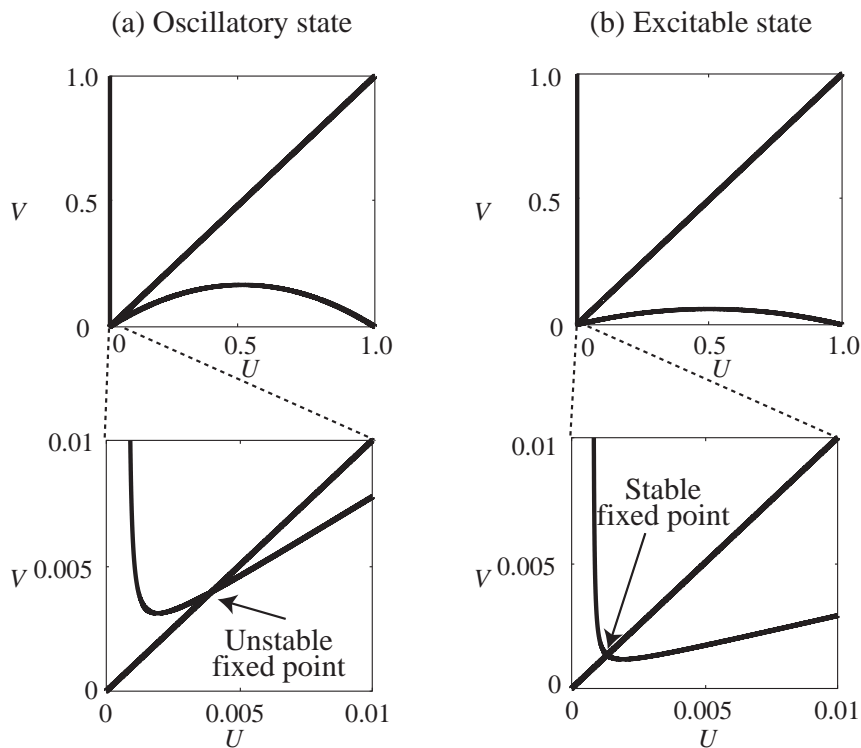
Figure 2.3: Nullclines of the 2-variable Oregonator (Tyson version). (a) Oscillatory state. (b) Excitable state. The parameters are $q = 0.0008$ and (a) $f = 1.5$, (b) $f = 4$. The lower figures are the magnifications near the intersections.
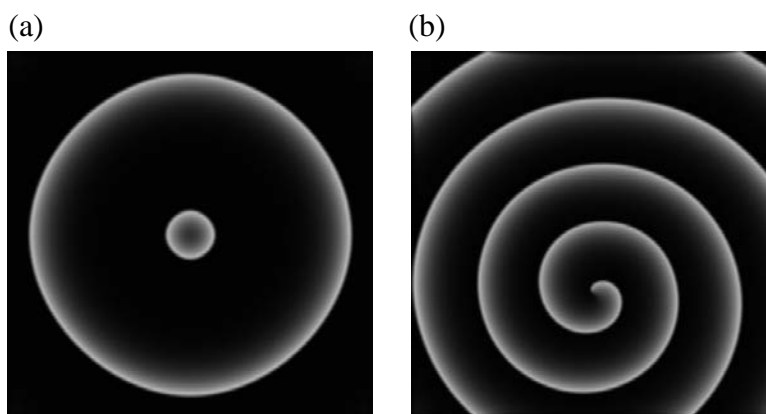

Figure 2.4: Numerical results on pattern formation using the Oregonator (Tyson version). (a) A target pattern and (b) a spiral pattern are exhibited. The parameters are $f = 3$, $q = 0.0008$, and $\epsilon = 0.04$.
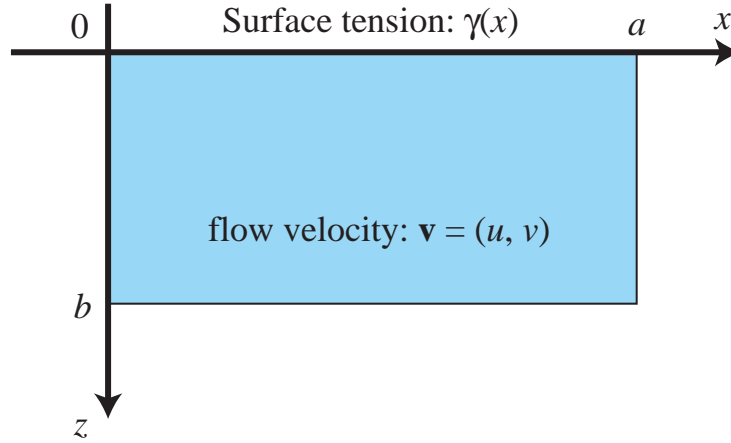
Figure 2.5: Schematic illustration on the system considered here. At the upper boundary, the surface tension is defined as $\gamma(x)$. At the other boundaries, a fixed boundary condition is adopted.

The mechanism of BZ reaction has been almost solved, but it is widely used as a model experimental systems for a reaction-diffusion system, or a nonequilibrium open system.

2.3   Marangoni effect and interfacial tension

It is known that spatial gradient of surface tension can cause convection. In this section, some characteristics of surface-tension-driven convection, or Marangoni effect, are introduced.

There are two types of the Marangoni effect: one is the thermal Marangoni effect and the other is the solutal Marangoni effect. The former is the convection driven by the surface tension gradient due to the temperature gradient, and the latter is that due to the concentration gradient [50, 51]. As for the thermal Marangoni effect, there have been a number of reports, but there have been only a few reports on the solutal Marangoni effect. In this thesis, the solutal Marangoni effect is mainly concerned.

The Marangoni effect can be understood in the framework of hydrodynamics. Using the Navier-Stokes equation, the surface tension gradient is introduced as a shear at the surface. Here, we consider the system as shown in Fig. 2.5. The x axis is set along the surface, and the z axis is perpendicular to the x axis. Supposing the component of the field velocity in x and z axis are u and v, the surface tension gradient along x axis is proportional to the tangential gradient of u:

$$\nu\frac{\partial u}{\partial z} = -\frac{\partial \gamma}{\partial x},\qquad(2.23)$$

where ν is the kinetic viscosity of the medium. Here, it is to be noted that the

surface has no curvature. As the surface have a certain curvature, the pressure difference between two phases should be considered, i.e., Laplace pressure [52].

In Chapters 3 and 5, we use another formulation, i.e., we introduce the surface tension as a volume force. We adopt the modified Navier-Stokes equations for incompressible fluid;

$$\rho \left(\frac{\partial \mathbf{v}}{\partial t} + (\mathbf{v} \cdot \nabla)\mathbf{v} \right) = \eta \nabla^2 \mathbf{v} - \nabla p + \mathbf{F}_{\mathrm{i}}, \qquad (2.24)$$

and

$$\nabla \cdot \mathbf{v} = 0. \qquad (2.25)$$

The interfacial tension term $\mathbf{F}_{\mathrm{i}}$ has the following shape:

$$\mathbf{F}_{\mathrm{i}} = \frac{\partial \gamma}{\partial x} \delta(z) \mathbf{e}_x. \qquad (2.26)$$

In this formulation, the surface tension is introduced as a volume force. The compatibility between eqs. (2.23) and (2.26) are confirmed as follows: A steady state is assumed and the pressure term is also assumed to be neglected. Then, eq. (2.24) becomes

$$\rho \mathbf{v} \cdot \nabla \mathbf{v} = \eta \nabla^2 \mathbf{v} + \mathbf{F}_{\mathrm{i}}. \qquad (2.27)$$

When ρ/η is small, i.e., $Re = \rho v l / \eta << 1$, the nonlinear term can be neglected:

$$\eta \nabla^2 \mathbf{v} + \mathbf{F}_{\mathrm{i}} = 0. \qquad (2.28)$$

Here, the system as shown in Fig. 2.5 is considered. In this discussion, we want to know the features near the interface, where v is nearly 0. For the x component of $\mathbf{v}$, u, follows the equation:

$$\frac{\eta}{\rho} \nabla^2 u = \frac{\partial \gamma}{\partial x} \delta(z). \qquad (2.29)$$

By integrating eq. (2.29) with z from 0 to b,

$$\frac{\eta}{\rho} \left(\int_0^b \frac{\partial^2 u}{\partial x^2} \mathrm{d}z + \left. \frac{\partial u}{\partial z} \right|_{z=b} - \left. \frac{\partial u}{\partial z} \right|_{z=0} \right) = \frac{\partial \gamma}{\partial x}. \qquad (2.30)$$

When the effect of the bottom interface is small enough, or the system is deep enough, we can assume that

$$\left. \frac{\partial u}{\partial z} \right|_{z=b} = 0, \qquad (2.31)$$

at the bottom interface. The first term of the left side is

$$
\begin{aligned}
\int_0^b \frac{\partial^2 u}{\partial x^2} \mathrm{d}z &= \int_0^b \frac{\partial}{\partial x} \left(-\frac{\partial v}{\partial z} \right) \mathrm{d}z \\
&= \int_0^b \frac{\partial}{\partial z} \left(-\frac{\partial v}{\partial x} \right) \mathrm{d}z \\
&= \left. \frac{\partial v}{\partial x} \right|_{z=b} - \left. \frac{\partial v}{\partial x} \right|_{z=0} \\
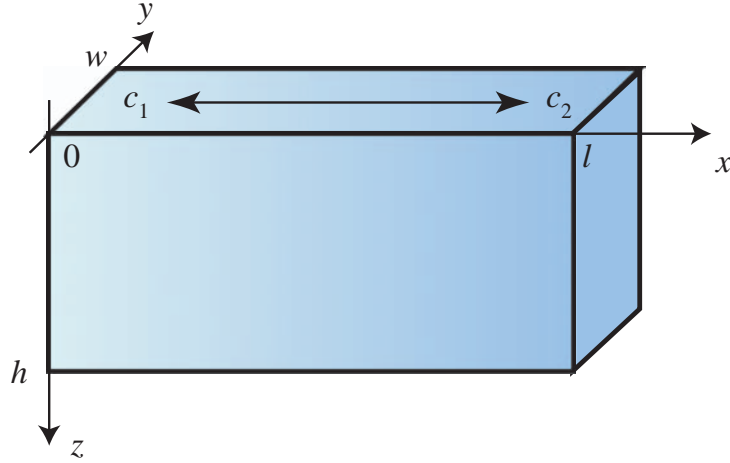&= 0, \qquad (2.32)
\end{aligned}
$$

Figure 2.6: Schematic illustration on the theoretical system in three dimension. The competition between the transportation by diffusion and by flow is important.

where the incompressive condition (eq. (2.25)) is used. Equation (2.30) can be written as follows:

$$\nu \left.\frac{\partial u}{\partial z}\right|_{z=0} = -\frac{\partial \gamma}{\partial x}, \tag{2.33}$$

where $\nu = \eta/\rho$.

Thus, the relationship between the surface tension and the tangential gradient of velocity (eq. (2.23)) is achieved.

By the way, the characteristics of the surface-tension driven convection can be identified by the nondimensional number named Marangoni number. Here, the meanings of this nondimensional number are easily exemplified.

We assume the system where two regions with the concentrations of c_1 and c_2 are at the distance of l. The width of the system is w and the depth is h. The coordinate is set so that the x coordinate meets the horizontal surface as shown in Fig. 2.6. The origin is set at the position where the concentration is c_1.

Without convection, the profile of the concentration should be linear:

$$c(x) = c_1 + (c_2 - c_1)x \equiv c_1 + \Delta c x. \tag{2.34}$$

This concentration gradient causes the gradient in surface tension, which drives the convective flow. The driving force per unit area is

$$(\gamma_2 - \gamma_1)\, w/l, \tag{2.35}$$

where γ_1 and γ_2 correspond to the surface tension for the regions with the concentration of c_1 and c_2, respectively. The driving force is assumed to be

averaged, and the driving force per unit volume can be written as

$$(\gamma_2 - \gamma_1)\, w/lh = \Delta\gamma w/lh. \tag{2.36}$$

On the other hand, if the Marangoni flow with a velocity of v was induced, the friction force per unit volume would be

$$|\eta\nabla v|\, d \approx \frac{\eta v}{h}d. \tag{2.37}$$

By assuming that the driving force is balanced to the friction force, i.e.,

$$\frac{\Delta\gamma w}{lh} = \frac{\eta v}{h}w \tag{2.38}$$

we can derive the following equation,

$$v = \frac{\Delta\gamma}{\eta}. \tag{2.39}$$

When the concentration difference is small enough, the surface tension gradient is described as a linear relationship:

$$\Delta\gamma = \frac{\mathrm{d}\gamma}{\mathrm{d}c}\Delta c. \tag{2.40}$$

Therefore, eq. (2.39) leads

$$v = \frac{\Delta c}{\eta}\frac{\mathrm{d}\gamma}{\mathrm{d}c}. \tag{2.41}$$

Considering the above discussion, the rate of transport by the flow is

$$M_{\mathrm{flow}} = v\Delta c = \frac{(\Delta c)^2}{\eta}\frac{\mathrm{d}\gamma}{\mathrm{d}c}. \tag{2.42}$$

On the other hand, the rate of transportation by diffusion is

$$M_{\mathrm{diffusion}} = D\frac{\Delta c}{l} \tag{2.43}$$

The critical value for whether convection is induced or not is the point where the above two transport rates become on the same scale. By considering the ratio between M_{flow} and $M_{\mathrm{diffusion}}$, we can discuss on whether convection is induced by the interfacial tension gradient. The ratio is written as follows:

$$\frac{M_{\mathrm{flow}}}{M_{\mathrm{diffusion}}} = \frac{(\Delta c)^2}{\eta D\Delta c}\frac{\mathrm{d}\gamma}{\mathrm{d}c} = \frac{\Delta c}{\eta D}\frac{\mathrm{d}\gamma}{\mathrm{d}c} \equiv Ma. \tag{2.44}$$

Thus, we can discuss on whether convection induced by surface tension happens or not using Marangoni number, Ma.

Part II

Spontaneous Motion in Reaction Diffusion System Coupled with Convection

Chapter 3

Convective flow coupled with BZ reaction

In this chapter, the convective flow induced by interfacial tension change in BZ reaction is exhibited. This system is a typical example of the reaction-diffusion-advection system. The convection is observed in the experiments [1], and the properties of the convective flow can be reproduced in numerical calculations [7].

3.1   Introduction

It was reported that the interfacial tension of BZ medium changes synchronized with the chemical oscillation, that is, BZ medium in the oxidized state has higher interfacial tension than that in the reduced state [53]. The catalyst used in the BZ reaction is ferroin, which is the complex of the ferrous ion and 1,10-phenanthroline. Since the phenanthroline is hydrophobic, the catalyst tends to be distributed near the surface and reduces the interfacial tension. A catalyst with a higher valence (oxidized form) is even more hydrophilic than that with a lower valence (reduced form). Therefore, in BZ solution, the surface distribution of the catalyst is less in the oxidized state than in the reduced state, which causes the difference in surface tension.

Driven by the repetitive change in interfacial tension, Miike et al. reported that Marangoni convection is induced at the free surface of BZ medium [54–56]. Though there have been some other reports on the convective flow in BZ reaction both experimentally and theoretically [57–64], the convection is induced on the perpendicular plane. Therefore the gravitational effects are unavoidable.

In the present study, we adopted a system made of two bulk phases of BZ reaction medium and oleic acid (oil), and observed the flow near the interface of the two phases by adding small particles for visualization. Since the interface is perpendicular to the horizontal plane, the gravity does not affect the convection. Due to the change in interfacial tension, Marangoni convection was induced synchronizing with the chemical wave propagation. Near the interface between
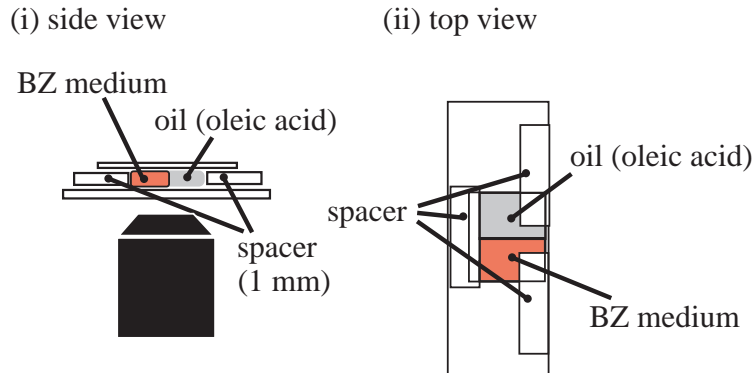
Figure 3.1: Schematic illustration on the experimental setup. Images are taken from below [1].

the both phases, the strong convective flow was observed toward the oxidized area, and two rolls were formed in the bulk phases. Numerical calculations based on the reaction-diffusion-advection equations were also performed, and can well reproduce the experimental results.

3.2　Experiments

All chemicals were analytical grade reagents and used without further purification. An aqueous solution of ferroin, tris (1,10-phenanthroline) iron (II) sulfate, was prepared by mixing stoichiometric amounts of 1,10-phenanthroline ($C_{12}H_8N_2$) and ferrous sulfate ($FeSO_4$) in pure water. The water was purified with a Millipore-Q system. BZ medium, in the excitable state, contains 0.15 M sodium bromate ($NaBrO_3$), 0.30 M sulfuric acid (H_2SO_4), 0.10 M malonic acid ($CH_2(COOH)_2$), 0.03 M potassium bromide (KBr), and 5.0 mM ferroin ($[Fe(phen)_3]^{2+}$). To visualize the convective flow, polystyrene beads (General Science Corporation, 10 μm in diameter) were dispersed throughout the medium. BZ medium and oleic acid were situated between two glass plates (clearance : 1.0 mm). A chemical wave was initiated using silver wire. The region near the interface between BZ medium and oleic acid was observed from below by an inverted microscope (Nikon DIA-PHOT-TMD), as schematically shown in Fig. 3.1.

3.3　Results

Figure 3.2 shows the convective flow that accompanied the propagation of a chemical wave in BZ medium, where the flow of the tracer beads was visualized as the accumulation of video frames over 1.0 s, together with image-processing to compensate for the nonuniformity of the illumination [65]. On the front of
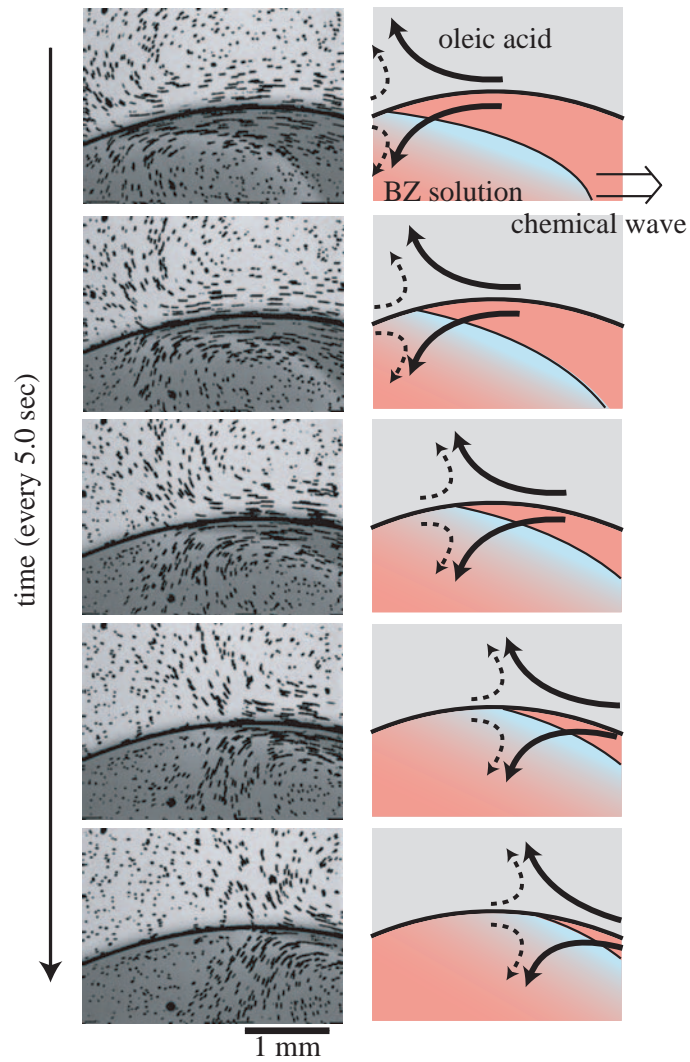
Figure 3.2: Results of convective flow on the horizontal plane. The profiles of streamlines in 1.0 s are shown at the intervals of 5.0 s. The upper phase is oleic acid and the lower phase is the BZ medium; the chemical wave propagated from left to right. Convective flow was generated towards the wave front on both sides (Left column) Schematic illustrations are also given to show the direction of convective flow (Right column) [1].
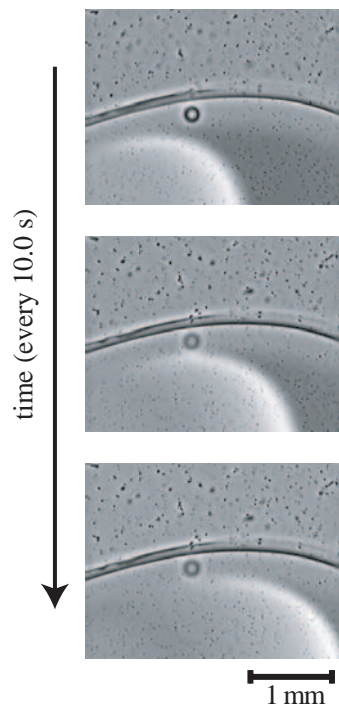
Figure 3.3: Disappearance of convective flow due to an inhibitor, iodine, of the chemical reaction. Pure oleic acid was replaced by oleic acid with iodine. The chemical wave propagated from left to right in the bulk solution, but did not reach the interface, and no convective flow was induced [1].

the chemical wave, large convective flow, parallel to the interface and opposite the direction of movement of the chemical wave, was induced in both the water and oil phases. Parallel flow in the same direction as the chemical wave was observed on the back of the chemical wave at the interface. In both the water and oil phases near the intersection of the chemical wave with the interface, the flow sank into the bulk phases. Figure 3.3 shows the results of an experiment in which iodine was added to the oil phase. In this experiment, no convective flow was generated, despite the appearance of a chemical wave. Iodine is a potent inhibitor of the BZ reaction [66, 67]. The iodine in the oil phase is expected to inhibit wave generation near the interface, due to its diffusion from the oil to the aqueous phase through the interface. Thus, the absence of convective flow can be attributed to the failure of the chemical wave to propagate near the interface. This convective flow is clearly caused by the difference in interfacial tension between the oxidized and the reduced states [53].
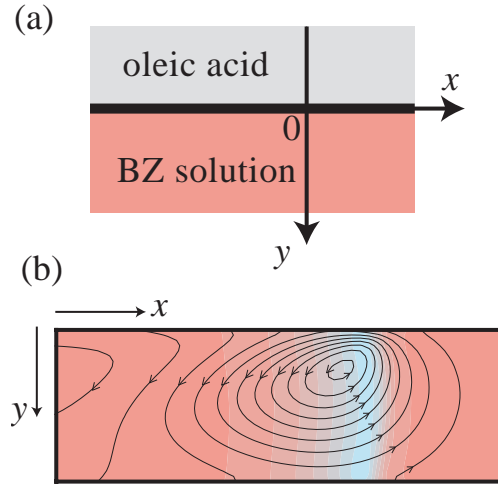
Figure 3.4: Results of numerical calculation. (a)The coordinate in the numerical calculation. The results are for the lower half plane ($y > 0$). (b)Profiles of a traveling chemical wave and the streamline in the bulk phase are shown. The region with large V, i.e., the oxidized state, is drawn with blue. The experimental trends have been thus represented in a qualitative manner. The parameters used in this simulation are $\rho = 1$, $\eta = 3$, $D_U = D_V = 0.5$, $\epsilon = 0.04$, $f = 3$, $q = 0.0008$, $k = 0.01$, and $\delta = 0.5$ [7].

3.4   Numerical calculation

For a numerical simulation, we adopted the 2-variable Oregonator, which has often been used for reproducing BZ reaction. In many past studies, the pattern in the settled BZ reaction medium is described as the reaction-diffusion equation using Oregonator as a reaction term. However, in this system, the medium can move. Therefore, we have to consider the dynamics of the medium, or field, itself. Consequently, we adopted Navier-Stokes equation for the movement of the medium. The medium is affected by the interfacial tension due to the change in the chemical components coupled with BZ reaction. Here, Cartesian coordinates are set so that the interface meets the x axis as shown in Fig. 3.4(a). Thus, we can write as follows:

$$\rho \left(\frac{\partial}{\partial t} + \mathbf{v} \cdot \nabla \right) \mathbf{v} = \eta \nabla^2 \mathbf{v} - \nabla p + \mathbf{F}_i, \tag{3.1}$$

$$\nabla \cdot \mathbf{v} = 0, \tag{3.2}$$

$$\left(\frac{\partial}{\partial t} + \mathbf{v} \cdot \nabla \right) U = F(U, V) + D_U \nabla^2 U, \tag{3.3}$$

$$\left(\frac{\partial}{\partial t} + \mathbf{v} \cdot \nabla\right) V = G\left(U, V\right) + D_V \nabla^2 V, \tag{3.4}$$

$$F\left(U, V\right) = \frac{1}{\epsilon}\left\{U(1 - U) - fV\frac{U - q}{U + q}\right\}, \tag{3.5}$$

$$G\left(U, V\right) = U - V, \tag{3.6}$$

where ρ is the density, $\mathbf{v}$ is the velocity of the fluid, p is the pressure, η is the viscosity, U and V are the concentrations of the represented chemical reagents, and f, ϵ, and q is the parameters corresponding to the nature of BZ medium. Here, interfacial tension is assumed to be as a volume force, which has non-zero value in the area within the distance, δ, from the interface as is commented in Chapter 2. The interfacial tension is proportional to the gradient of the concentration of oxidized catalyst, V:

$$\mathbf{F}_{\mathrm{i}} = \begin{cases} k\frac{\partial V}{\partial x}\mathbf{e}_x & (0 < y < \delta), \\ 0 & (y > \delta), \end{cases} \tag{3.7}$$

where k is a positive constant and $\mathbf{e}_x$ is the unit vector in the x direction.

In Fig. 3.4(b), the profiles in the bulk phase calculated using the above equations are shown. In the numerical calculation, SMAC method (Simplified marker and cell method) was used [68]. Near the interface, convective flow is induced toward the point where chemical wave touches the interface. The chemical wave near the interface propagates slower than that in the bulk phase. These characteristics are qualitatively similar to those of the experimental results.

3.5　Discussion

Using the above-mentioned framework, the profile of interfacial tension can be estimated. The x and y components of fluid velocity $\mathbf{v}$ are supposed to be u and v, respectively. Here, the pressure term does not play an important role, it is neglected for simplicity. The x component of eq. (3.1) is

$$\rho\left(\frac{\partial u}{\partial t} + u\frac{\partial u}{\partial x} + v\frac{\partial u}{\partial y}\right) = \eta\left(\frac{\partial^2 u}{\partial x^2} + \frac{\partial^2 u}{\partial y^2}\right) + F_{\mathrm{i}}. \tag{3.8}$$

As we approach the region near the interface, the velocity parallel to the interfacial plane, u, is much greater than that perpendicular to the plane, v. Thus we can neglect the term $\rho v \partial u/\partial y$. The term $\eta \partial^2 u/\partial y^2$ represents the diffusion-like behavior in the y direction. The characteristic time for passing of the chemical wave, Δt, is about 10 s based on the experimental results. Therefore, the characteristic depth of the region, Δy, in which fluid moves attached to the interface is calculated as

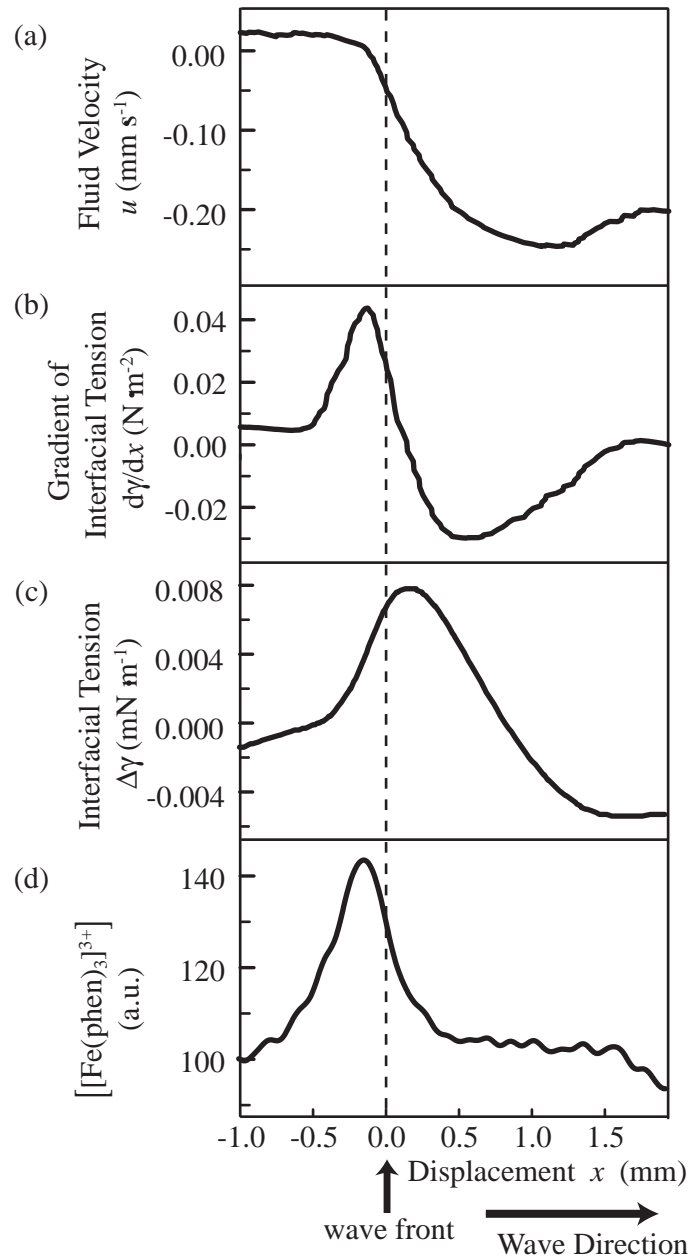$$\Delta y \sim \sqrt{\frac{\eta}{\rho}\Delta t} \simeq 0.3\,\mathrm{cm}. \tag{3.9}$$

Figure 3.5: Spatial profile of various physics-chemical variables deduced from the experimental results on convection generated by the BZ reaction, as in Fig. 3.2. (a) Fluid velocity, u, parallel to the interface in the region near the interface. The chemical wave propagates from left to right, and the origin is set at the position of the wave front. (b) The gradient of interfacial tension, $d\gamma/dx$, calculated from the fluid velocity profile. (c) Interfacial tension, $\Delta\gamma$, calculated by integration of (b). (d) The chemical wave as represented by a change in the color of the solution that corresponds to the concentration of ferriin ($[Fe(phen)_3]^{3+}$) [1].

From the experiments, the viscosity of the BZ medium was around 1.1×10^{-2} g cm^{-1} s^{-1}. In this calculation, the viscosity and density of BZ medium are adopted. From now on, only the x component is considered, and the interfacial tension is taken as the force working in the region within Δy from the interface. In this framework, the interfacial tension can be considered s a volume force, and can be combined with an interfacial tension constant γ as follows:

$$\frac{\partial \gamma}{\partial x} = F_\mathrm{i} \Delta y. \tag{3.10}$$

Since the chemical wave propagates at a constant velocity, c, the fluid velocity profile, u, satisfies the differential equation:

$$\frac{\partial u}{\partial t} = c \frac{\partial u}{\partial x}. \tag{3.11}$$

From the experiment, the velocity of the chemical wave parallel to the interface is $c = 0.01 \, \mathrm{cms^{-1}}$. Thus, eq. (3.8) can be simplified to a one-dimensional ordinary differential equation:

$$\rho \left(c \frac{\mathrm{d}u}{\mathrm{d}x} + u \frac{\mathrm{d}u}{\mathrm{d}x} \right) = \eta \frac{\mathrm{d}^2 u}{\mathrm{d}x^2} + F_\mathrm{i}. \tag{3.12}$$

The fluid velocity profile near the interface was measured, and the results are shown in Fig. 3.5(a). Using these results, the first-order derivative, the second-order derivative, and the interfacial tension profile are calculated. The profile of the gradient of the interfacial tension, $\mathrm{d}\gamma/\mathrm{d}x$, is shown in Fig. 3.5(b). Using this profile, the profile of the interfacial tension, $\Delta\gamma$, is calculated by integration, as shown in Fig. 3.5(c). The profile of the chemical wave is shown in Fig. 3.5(d), which was obtained from a quantitative analysis of the color in the reacting solution. The profile of the chemical wave corresponds to the profile of the interfacial tension, except for the slight differences in their peak positions and widths. These differences are attributed to the effect of the convective motion of the reacting solution. As in Fig. 3.2, the portion of the fluid in the reduced state (low $[\mathrm{Fe(phen)_3}]^{3+}$) is pulled toward the front of the chemical wave. This convective effect causes retardation of the phase of the oscillatory reaction of the wave front, together with narrowing of the chemical wave. The change in interfacial tension between the oxidized state and the reduced state is on the order of $0.01 \, \mathrm{mNm^{-1}}$, as in Fig. 3.5(c). This is about 1% of the value in a previous report [53], where the interfacial tension was measured under the condition that the BZ medium was stirred and the medium was uniform. In the present experiment, we estimated the change in interfacial tension under the condition of propagation of a chemical wave without stirring the reaction medium. Since the interfacial tension on the front of the wave is opposite that on the back, the net velocity may be damped. In the analysis adopted above, we assumed that the system was two-dimensional, however, the actual system was

the space between two glass plates. The fluid must be affected by the friction from the glass plates, which should disturb the motion of the fluid. In addition, there would be a rather large damping effect, i.e., flow in the aqueous phase inevitably induces flow in the oil phase. The discrepancy in the amplitude of the change in interfacial tension can be attributed to these effects. This estimation of the interfacial tension profile from the fluid velocity profile might be useful in an analysis of fluid dynamics.

Chapter 4

Spontaneous motion of a BZ droplet

In this chapter, spontaneous motion of a small droplet of BZ reaction medium on an oil phase is exhibited [1]. This can be regarded as an experimental system where chemical energy is transduced into mechanical energy. This spontaneous motion is related to the convection inside the droplet [2].

4.1   Introduction

In the previous chapter, Marangoni convection at the interface between BZ medium and oil driven by a repetitive change in interfacial tension is presented. Near the interface between these two phases, strong convective flow is observed toward the wave front, and two rolls are formed in both phases. Moreover, the experimental results can be reproduced by a numerical calculation using the Navier-Stokes equation coupled with a reaction-diffusion-advection equation based on the Oregonator.

The convection coupled with the BZ reaction can be regarded as chemo-mechanical energy transduction, but only the motion of the small particles for visualization can be observed due to the convective flow. Therefore, we designed the system where the macroscopic motion is induced by the chemo-mechanical energy transduction in BZ reaction. In the past studies, Yoshida et al. have exemplified the spontaneous deformation of the gel synchronized with BZ reaction [69, 70], but the deformation is due to the characteristics of the gel. In the present study, only by making the system size small, a droplet of BZ medium can be driven by the convection due to the interfacial tension. In this chapter, the experimental results and discussion on the mechanism are presented.
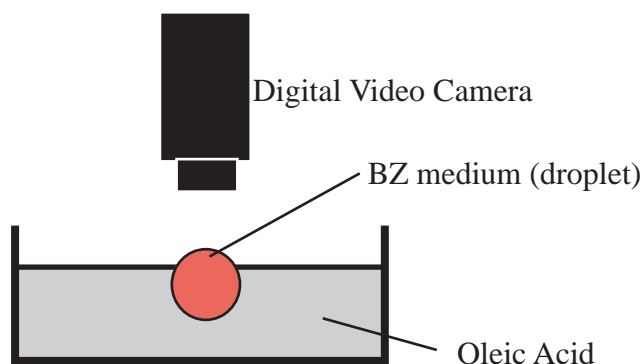
Figure 4.1: Schematic illustration of the experimental setup. Images were recorded from above [1].

4.2 Spontaneous motion of a BZ droplet on oil phase

All chemicals were analytical grade reagents and used without further purification. An aqueous solution of ferroin, tris (1,10-phenanthroline) iron (II) sulfate, was prepared by mixing stoichiometric amounts of 1,10-phenanthroline ($C_{12}H_8N_2$) and ferrous sulfate ($FeSO_4$) in pure water. The water was purified with a Millipore Milli-Q system. BZ medium, in the oscillatory state, contains 0.15 M sodium bromate ($NaBrO_3$), 0.60 M sulfuric acid (H_2SO_4), 0.10 M malonic acid ($CH_2(COOH)_2$), 0.03 M sodium bromide (NaBr), and 5.0 mM ferroin ($[Fe(phen)_3]^{2+}$). To visualize convective flow, polystyrene beads (General Science Corporation, 10 μm in diameter) were dispersed throughout the medium. Using the experimental system shown schematically in Fig. 4.1, we observed the motion of a 1.0-μl droplet of BZ medium floating on a layer of oleic acid.

Figure 4.2 shows the experimental results on the motion of a BZ droplet floating on the surface of oleic acid. The spatio-temporal plot indicates a translational motion of the droplet accompanied by the propagation of a chemical wave.

4.3 Convective flow inside the spontaneously-moving droplet

For clarification of the nature of this motion, the x axis is set in the direction of the spontaneous motion of the droplet, as shown in Fig. 4.3(a). The positive direction is defined as that in which the droplet moves first. The chemical wave propagated keeping the shape of a circle, and when the chemical wave propagating in the negative x direction touched the interface, the droplet began to move in the positive direction. After the entire droplet turned to the oxidized
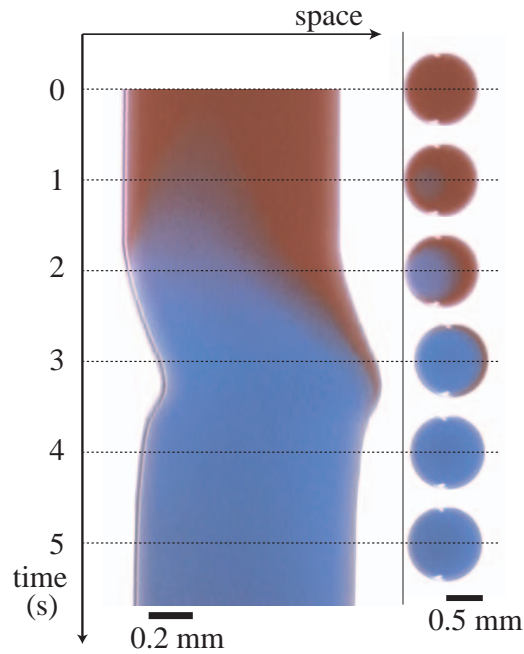
Figure 4.2: Spatio-temporal plot on the motion of a droplet of BZ medium with the snapshots each 1.0 s. Each image on the dotted line is aligned with time to show the translational motion of the droplet. The change in the shape of the droplet was not observed [1].
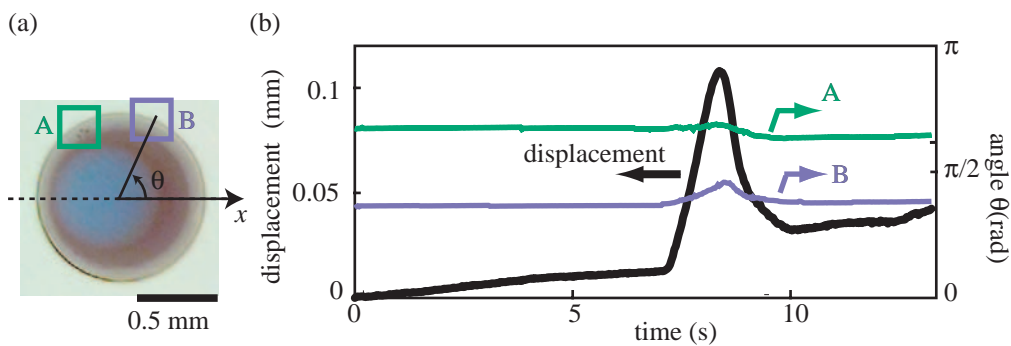

Figure 4.3: Experimental results regarding the convection inside a droplet of BZ medium. (a) Two measured particles inside the droplet are shown as A and B. (b) Time traces of the angles of the particles from the x axis (the direction of the motion). The time trace of translational motion of the droplet is also shown [2].
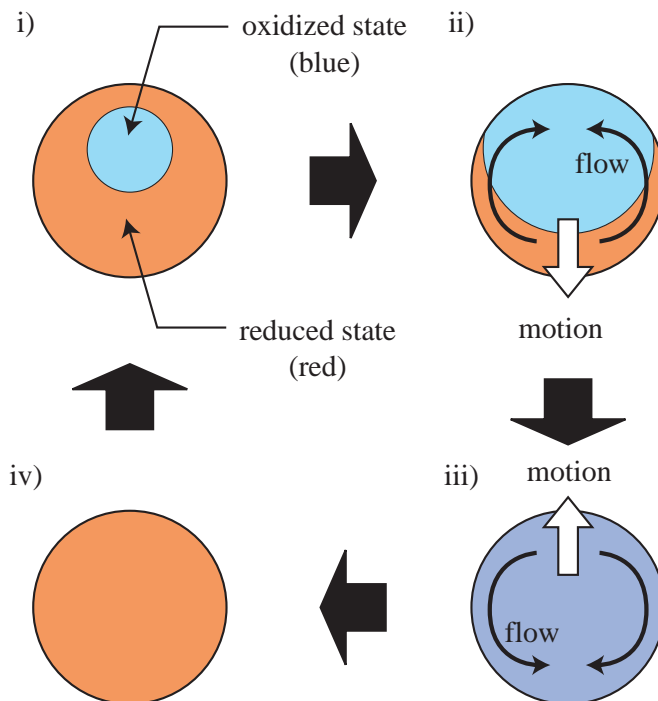
Figure 4.4: Schematic illustration on the mechanism of the spontaneous motion of a BZ droplet [2].

state, it moved back in the negative direction as shown in Figs. 4.2 and 4.3(b).

To observe the characteristics of the convection inside the droplet, we measured the positions of the particles located near the interface of the droplet. Figure 4.3(b) shows the time traces of the position of the center of the droplet and the angles between the positions of the particles and x direction. The origin was set at the center of the droplet. As the droplet moved in the positive direction, convective flow was observed in the counterclockwise direction on the upper semicircle. In contrast, after the entire droplet reached the oxidized state, convective flow was induced in the opposite direction, as schematically shown in Fig. 4.4.

4.4   Discussion

We consider only the concentration of the catalyst near the surface. The BZ reaction medium in the oxidized state has a higher interfacial tension than that in the reduced state, since the distribution of the catalyst near the surface is different [53].

First, as the chemical wave touches the interface of the droplet, convective flow is induced by the difference in interfacial tension between the oxidized and reduced states. This convective flow causes motion in the positive direction, since

there is interaction between the aqueous and organic phases at the interface. They exchange momentum, which results in the total translational motion [71]. Due to the convective flow, the oxidized catalyst at the interface accumulates in the region where the chemical wave propagates last. As the chemical wave finishes propagation and the entire droplet turns to the oxidized state, the concentration gradient of the oxidized catalyst near the interface causes backward convection. The interfacial tension at regions with less catalyst is higher than that in regions with more catalyst. Thus, the direction of the convective flow is reversed, which results in the back-and-forth spontaneous motion of the BZ droplet. It is noted that we can neglect the return to the reduced state, since the time scale of the spontaneous motion is much shorter than the period of chemical oscillation.

By the way, the motive force of the droplet is the gradient of interfacial tension, which is proportional to the length of where the chemical wave touches the interface between the BZ medium and oleic acid. Hence, the interfacial tension is proportional to r, the system size:

$$|\mathbf{F}_i| \propto \gamma r. \tag{4.1}$$

On the other hand, the mass, M, is proportional to the cube of the system size:

$$M = \rho r^3. \tag{4.2}$$

The acceleration α is, thus, proportional to r^{-2},

$$|\mathbf{F}_i| = M\alpha, \tag{4.3}$$

$$\alpha \propto \frac{\gamma}{\rho} \frac{1}{r^2}. \tag{4.4}$$

From the above discussion, the BZ droplet should move more as the size of the system gets smaller. However, the chemical reaction is hard to activate, when the system is smaller. Moreover, the time lag from when chemical wave touches one side to when it touches the other side becomes shorter, so the droplet moves less. Considering these factors, a system size of ~ 1 mm is suitable for observing the spontaneous motion of a BZ droplet.

4.5 Deformation of a droplet coupled with BZ reaction

When the BZ droplet sinks down and touches the bottom of the petri dish, it cannot move translationally, but rather becomes deformed. The experimental results together with the schematic representation are shown in Fig. 4.5. In this system, the droplet is stuck to the bottom and chemical energy is transduced into deformation of the droplet rather than translational motion. In this phenomena, the detailed mechanism has not yet been solved. Both experimental and theoretical studies are needed to understand this phenomenon.
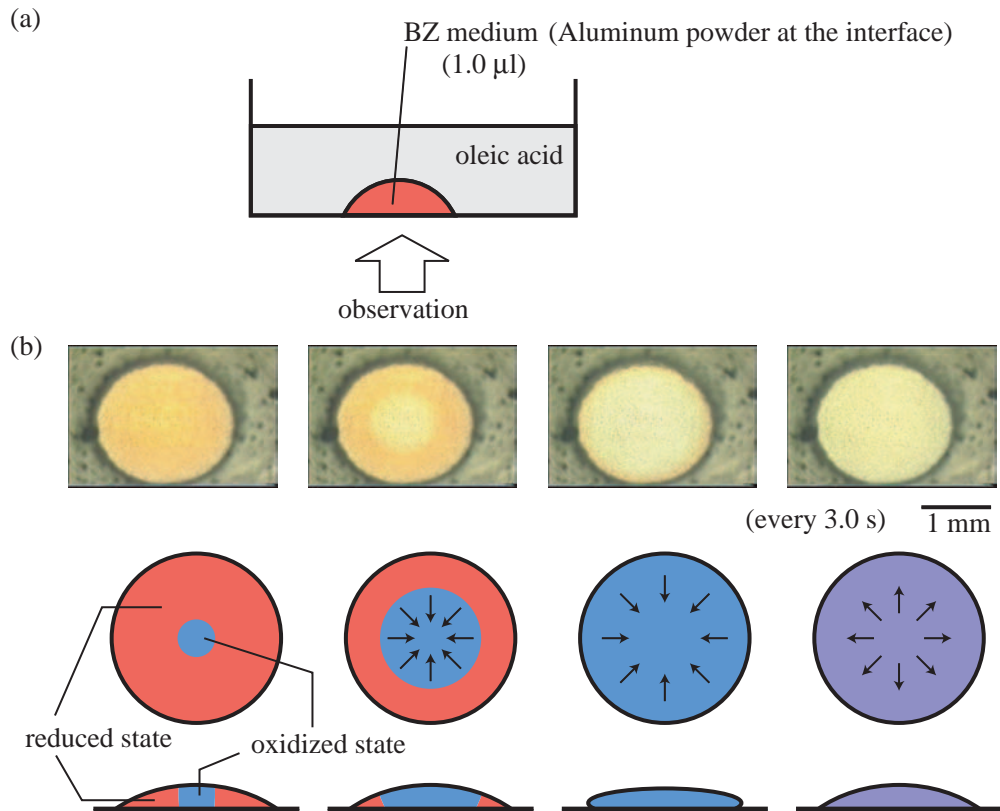
Figure 4.5: Spontaneous deformation of a droplet of BZ medium. (a) Experimental setup. The composition of the BZ medium was the same as that in the above-mentioned experiment on a floating BZ droplet. We placed a small amount of BZ medium (1.0 ml) at the bottom of the oleic acid phase, and observed with an inverted microscope (Nikon DIAPHOT-TMD). Since the BZ medium was in an oscillatory state, a chemical wave was initiated spontaneously. (b) Schematic representation on the experimental results from the side and below. The arrows in the figures correspond to the motion of the interface observed by placing aluminum powder at the interface of the BZ droplet. The chemical wave propagated from the center, and motion of the interface could be seen toward the wave front. After the entire droplet reached the reduced state, deformation of the droplet was observed. Periodic change in shape was, thus, generated [4].

Chapter 5

Convective motion in water-camphor system

In this chapter, the spontaneous motion of a camphor disk is firstly introduced. Then, convective flow induced by the surface tension gradient due to the camphor layer is investigated both experimentally and theoretically. Some systems are also exemplified where the spontaneous motion of a camphor disk is affected by the convective flow.

5.1   Introduction

In the 19th century, Rayleigh reported that camphor grains floating on water exhibit irregular motion called a "camphor dance" [72]. When a disk of camphor is placed on water, it moves in one direction almost at a constant velocity. Such motion is induced by the gradient in the surface tension [73]. Since the camphor disk is almost circular and is placed on the water gently, the system can be considered isotropic. The camphor molecule layer formed around the camphor grain, which is axially symmetric. Due to the dissolution from the camphor grain and sublimation from the camphor layer, the concentration of camphor on the surface has a gradient. This gradient makes the resting state unstable, and the disk begins to move at a constant velocity in a certain direction, thus breaking axial symmetry [74].

When anisotropy is introduced to the shape of a camphor grain, its motion can be easily controlled. For example, a camphor grain with the shape of a "hat (^)", as shown in Fig. 5.1 (b)-ii, exhibits unidirectional motion, while one with the shape of a "comma (,)" as shown in Fig. 5.1 (b)-iii or iv, exhibits a rotational motion [73].

This translational and rotational motion is described for the position of the center of gravity, $\mathbf{r}$, and the rotational angle θ of the camphor grain:

$$m\frac{\mathrm{d}^2\mathbf{r}}{\mathrm{d}t^2} = -k_\mathrm{t}\frac{\mathrm{d}\mathbf{r}}{\mathrm{d}t} + \mathbf{F}, \tag{5.1}$$
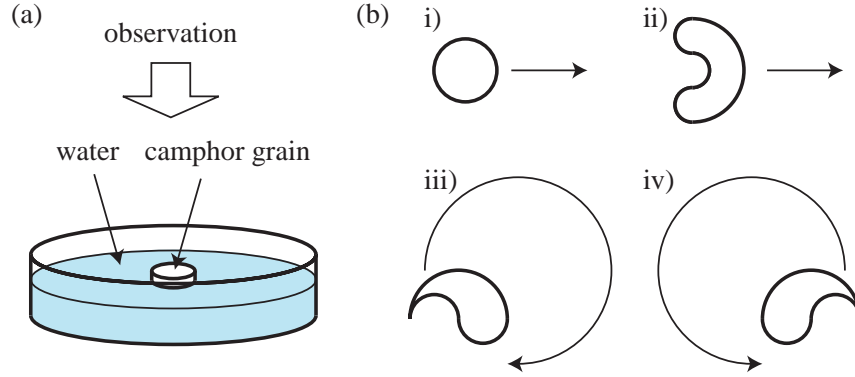
Figure 5.1: Spontaneous motion of a camphor grain on water. (a) Rough sketch of the experimental setup. (b) i) A circular camphor disk on the aqueous phase does not stand still, but rather spontaneously moves in one direction. ii) A camphor grain shaped like a "hat (̂)" exhibits translational motion at a constant velocity. iii and iv) A camphor grain shaped like a "comma (,)" exhibits rotational motion [4].

$$I\frac{\mathrm{d}^2\theta}{\mathrm{d}t^2} = -k_\mathrm{r}\frac{\mathrm{d}\theta}{\mathrm{d}t} + N, \tag{5.2}$$

where m is the mass, I is the moment of inertia of the camphor grain, and k_t and k_r are the viscosity resistance for translational and rotational motion, respectively. $\mathbf{F}$ and N are the total force and torque working on the camphor grain due to the surface tension gradient:

$$\mathbf{F} = \oint \gamma\mathbf{n}\mathrm{d}l, \tag{5.3}$$

$$N = \oint \gamma\,(\mathbf{l} - \mathbf{r}) \times \mathbf{n}\mathrm{d}l, \tag{5.4}$$

where the contour integral is executed along the boundary of the camphor grain, γ is the surface tension, $\mathbf{n}$ is the normal vector, and $(\mathbf{l} - \mathbf{r})$ is the vector from the center of mass. The surface tension is dependent on the density of the camphor layer, which can be approximately calculated as follows:

$$\gamma(c) = \frac{\gamma_0}{c + \tilde{c}}. \tag{5.5}$$

The dynamics of the surface concentration of camphor, c, is described as a reaction-diffusion equation:

$$\frac{\partial c}{\partial t} = -kc + D\nabla^2 c + G\,(\mathbf{r}, \omega), \tag{5.6}$$

where the terms, $-kc$ and $D\nabla^2 c$, correspond to the sublimation and surface diffusion of the camphor layer, respectively. $G\,(\mathbf{r}, \omega)$ is the term of development
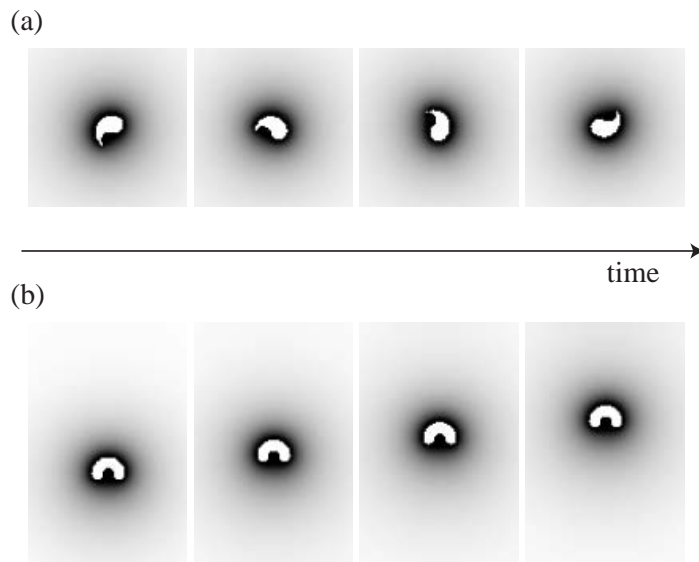
(a)

time

(b)

Figure 5.2: Typical numerical results on the spontaneous motion of a camphor grain shaped like (a) a "hat (ˆ)" and (b) a "comma (,)" based on eqs. (5.1) - (5.7). The parameters, m and I, are calculated from the shape of the grain by letting the density as 0.1. The other parameters are $k_t = 10^3$, $k_r = 0.1$, $D = 10$, $k = 0.01$, $\alpha = 10$, $c_0 = 1$, $\gamma_0 = 1$, and $\tilde{\gamma} = 1$ [4].

of the camphor layer from the grain:

$$G\left(\mathbf{r}, \omega\right) = \begin{cases} \alpha(c_0 - c) & \text{if the point is inside the grain.} \\ 0 & \text{otherwise} \end{cases} \quad (5.7)$$

Numerical results based on the above equations are shown in Fig. 5.2.

When the shape of the grain is isotropic, N is cancelled and the grain exhibits only translational motion. In contrast, when it is not isotropic, N has a finite value, and it exhibits rotational motion as well as translational motion.

In the above discussion, convective flow is not concerned; however, we can observe strong convective flow in the bulk phase. Therefore, in this chapter, we will discuss the convective flow due to the surface tension difference induced by the development of camphor molecular layer from the disk. We also report on the influence of the convection on the spontaneous motion of a camphor disk in the last section of this chapter.

5.2 Experiments

Camphor was obtained from Wako Chemicals (Kyoto, Japan). Water was first distilled and then purified with a Millipore-Q system. A camphor disk (diameter: 3 mm, thickness: 1 mm) was prepared using a pellet die set for FTIR. 3 ml
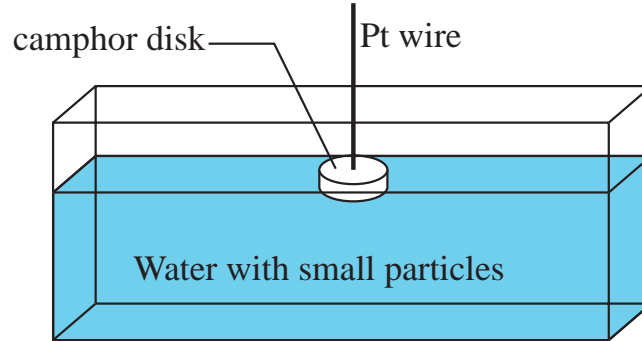
Figure 5.3: Schematic illustration on the experiments on the convective flow induced by the camphor disk [3].

of water was poured into a quasi-one-dimensional polystyrene chamber (inner length: 90 mm, width: 5 mm, depth: 9 mm, water level: 7 mm). The temperature of the water chamber was adjusted to 293 ± 1 K with a thermoplate (TP-80, AS ONE Co. Ltd., Japan). Plastic beads (DIAION, HP20S, relative density: 1.01, Mitsubishi Chemical Co. Ltd., Japan) were mixed in the aqueous phase to visualize the convective flow around the camphor disk. As shown in Fig. 5.3, the camphor disk was fixed with a platinum wire and the motion of the plastic beads were observed from side with a digital video camera and then analyzed with an image-processing system.

5.3   Results

Figure 5.4 shows a streamline of the convective flow observed by the dispersion of plastic beads in the aqueous phases with different viscosities. In this experiment, the camphor disk was fixed with a platinum wire at the air/aqueous interface. The streamlines for 1/3 s are shown in the both figures. With an increase in viscosity, the velocity of convective flow clearly decreased.

5.4   Numerical calculation

In order to discuss on the convective flow in the water-camphor system, we made numerical calculations using the following equations:

$$\rho \left(\frac{\partial}{\partial t} + \mathbf{v} \cdot \nabla \right) \mathbf{v} = \eta \nabla^2 \mathbf{v} - \nabla p + \mathbf{F}_i, \tag{5.8}$$
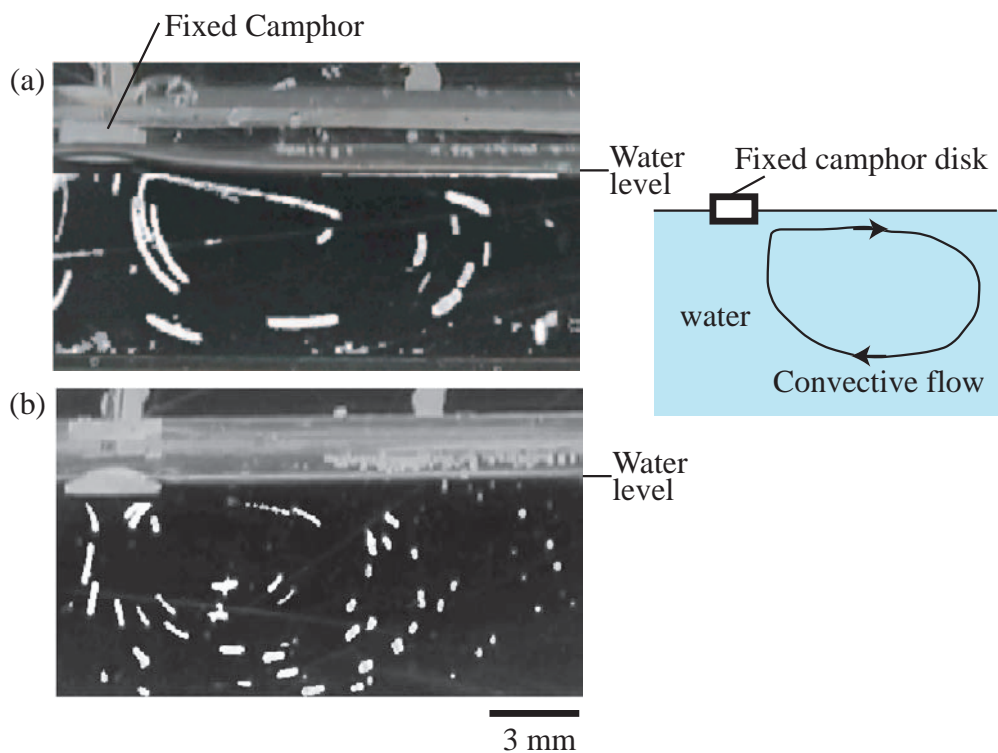
$$\nabla \cdot \mathbf{v} = 0, \tag{5.9}$$

Figure 5.4: Trajectories of the convective flow (analyzed time: 1/3 s), as visualized with plastic beads (diameter: 100-200 μm) in a side view when a camphor disk was placed on (a) the surface of an aqueous phase with (a) 5 mol l^{-1} and (b) 10 mol l^{-1} glycerin. The viscosity is larger in the solution of (b) than that of (a). The nature of convective flow on the left side of the camphor disk (data not shown) was similar to that on the right side [3].
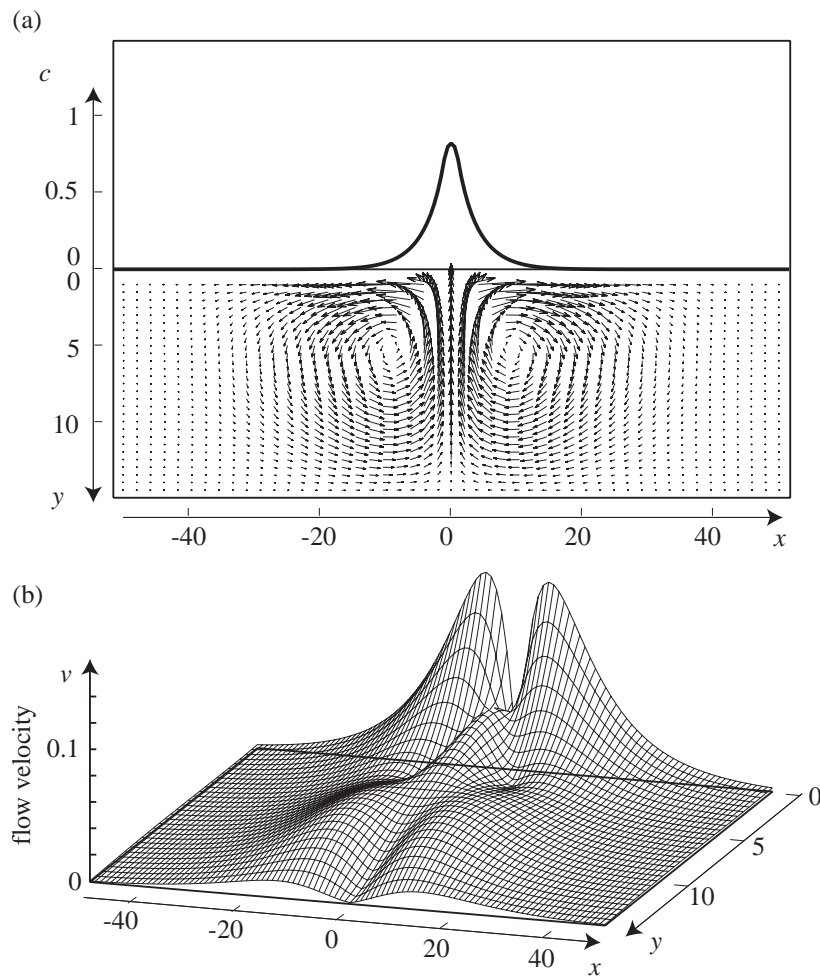
(a)

(b)

Figure 5.5: Results of the numerical calculation. It is assumed that a camphor disk is fixed at the origin, i.e., $x_c = 0$. (a) The surface concentration of the camphor layer and the flow velocity at representative points are shown. (b) To clarify the magnitude of the flow velocity, the absolute value of the flow velocity is shown. The parameters are $\rho = 1$, $\eta = 1$, $D = 0.5$, $\alpha = 0.1$, $\tilde{c} = 1$, $c_0 = 1$, $\gamma_0 = 1$, $\delta = 0.5$, $r = 1$, and $b = 1$ [3].

$$\left(\frac{\partial}{\partial t} + \mathbf{v} \cdot \nabla\right) c = -\alpha c + H(x, c) + D\nabla^2 c, \tag{5.10}$$

where c is the surface concentration of the camphor, α is the rate constant of sublimation, D is the surface diffusion constant of camphor, and $H(x, c)$ is the term of the supply of camphor from a grain. Letting that the position of the camphor grain is $x = x_c$ and that the size is r, we can write

$$H(x, c) = \begin{cases} b(c_0 - c) & (|x - x_c| < r), \\ 0 & (|x - x_c| \geq r), \end{cases} \tag{5.11}$$

where b is the rate constant of the supply of the camphor, and c_0 is the saturated surface concentration. The interfacial tension is

$$\mathbf{F}_\mathrm{i} = \begin{cases} \frac{\partial \gamma}{\partial x}\mathbf{e}_x & (0 < y < \delta), \\ 0 & (y > \delta), \end{cases} \tag{5.12}$$

$$\gamma = \frac{\gamma_0}{c + \tilde{c}}, \tag{5.13}$$

where $\gamma_0/\tilde{c}$ denotes the interfacial tension of the pure water surface without any camphor.

In Fig. 5.5, the numerical results are shown, when a camphor grain is fixed. The numerical result qualitatively reproduces the experimental one, and we suggest the convective flow may affect the spontaneous motion of a camphor grain on water. When changing the viscosity in the numerical calculation, the velocity of the convective flow is decreased, which also reproduced the experimental results (data not shown).

5.5   Effects of convective flow on the spontaneous motion

Figure 5.6 shows the camphor motion on water in a chamber with a saw-tooth-shaped base. A chamber with a saw-tooth-shaped base made of polycarbonate material was prepared by a fused deposition modeling process using TITAN (Stratasys Corporation) at U-tec Corporation. The camphor moved over three teeth under the present conditions. The maximum velocity in the leftward motion (~ 60 mm s^{-1}) was greater than that in rightward motion (50 mm s^{-1}). The velocity decreased when the camphor disk passed over the front edge of the saw tooth while moving to the right, as marked by leftward arrows. In contrast, the velocity increased when the camphor disk passed over the edge while moving to the left, as marked by rightward arrows.

Figure 5.7 shows the results of a numerical calculation under a saw-tooth-shaped boundary condition. Leftward flow is stronger than rightward flow near the camphor disk ($x = 0$). Due to this stronger leftward flow, leftward motion
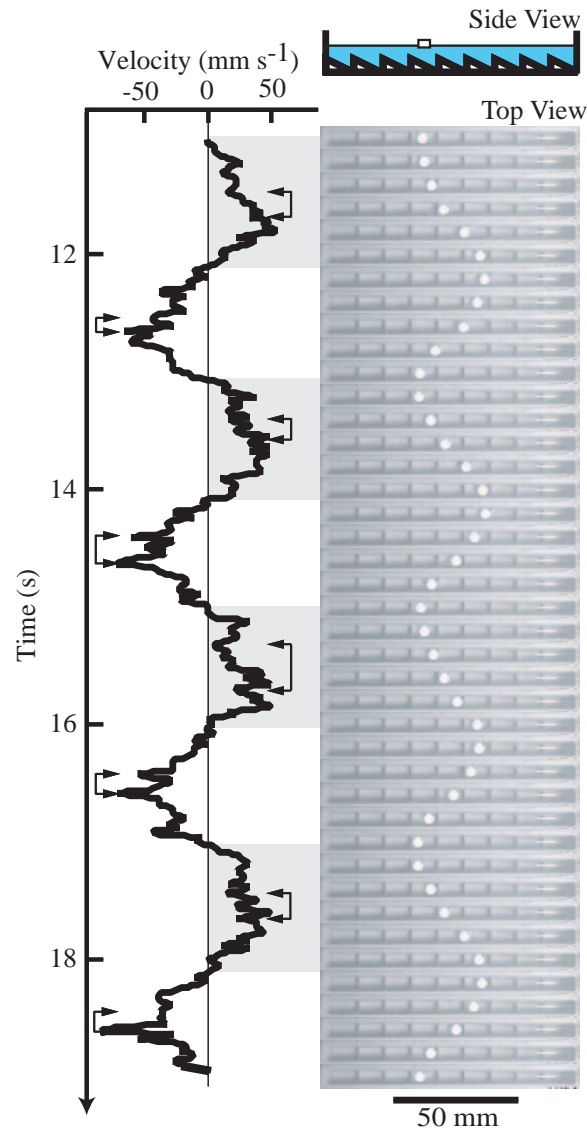
Figure 5.6: Results of the experiments using the chamber with a saw-tooth-shaped base. Right: Snapshots of camphor motion with a time interval of 0.2 s (top view) in the chamber shown schematically (side view). Left: Time variation of the velocity of a camphor disk. The analyzed data correspond to those in the snapshots on the right. The positive (gray areas) and negative velocities correspond to the motion to the right and left in the chamber. The rightward and leftward arrows denote when the camphor disk passed over the front edge of a saw-tooth blade from the right to the left and vice versa, respectively [3].

(a)

(b)
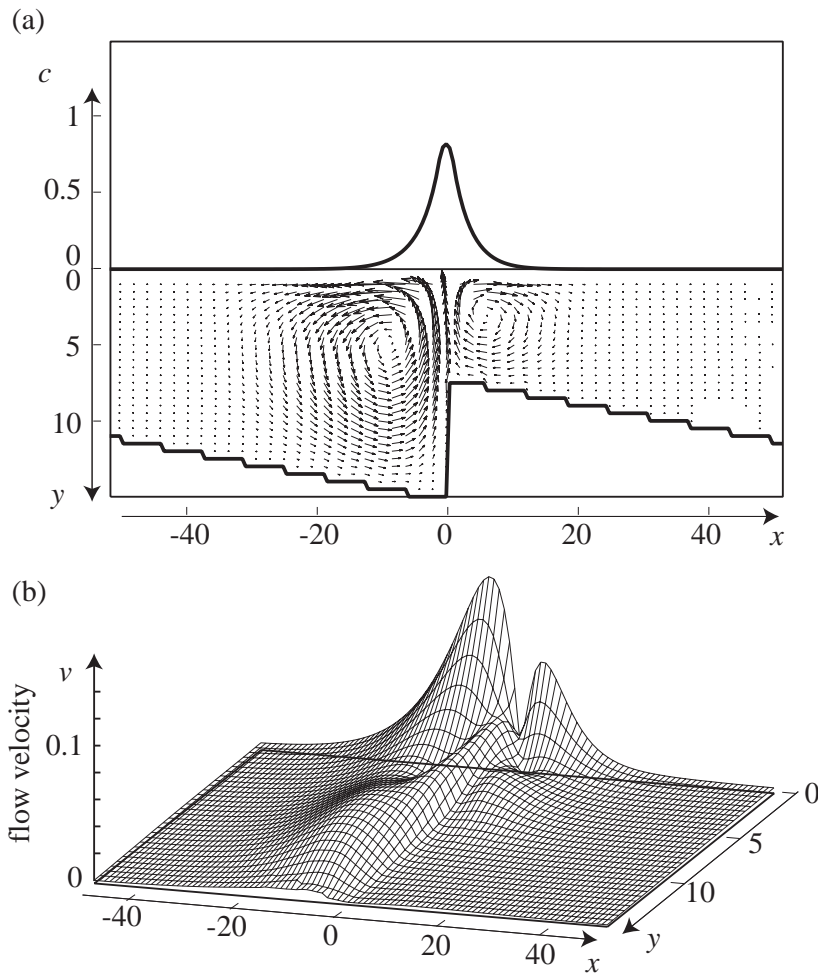
Figure 5.7: The numerical results under a saw-tooth-shaped boundary condition. (a) The surface concentration of the camphor layer and the flow velocity at the representative points are shown. (b) To clarify the magnitude of the flow velocity, the absolute value of the flow velocity is shown. Leftward flow is stronger than rightward flow near the camphor disk. Due to this stronger leftward flow, leftward motion of the camphor disk is accelerated and rightward motion is decelerated near the edges of the saw-tooth blades. The experimental trends shown in Fig. 5.6 can be explained by this effect of the asymmetry in the boundary condition. The parameters are the same as those used in Fig. 5.5 [3].

(a)

30 mm

(b)

100 mm
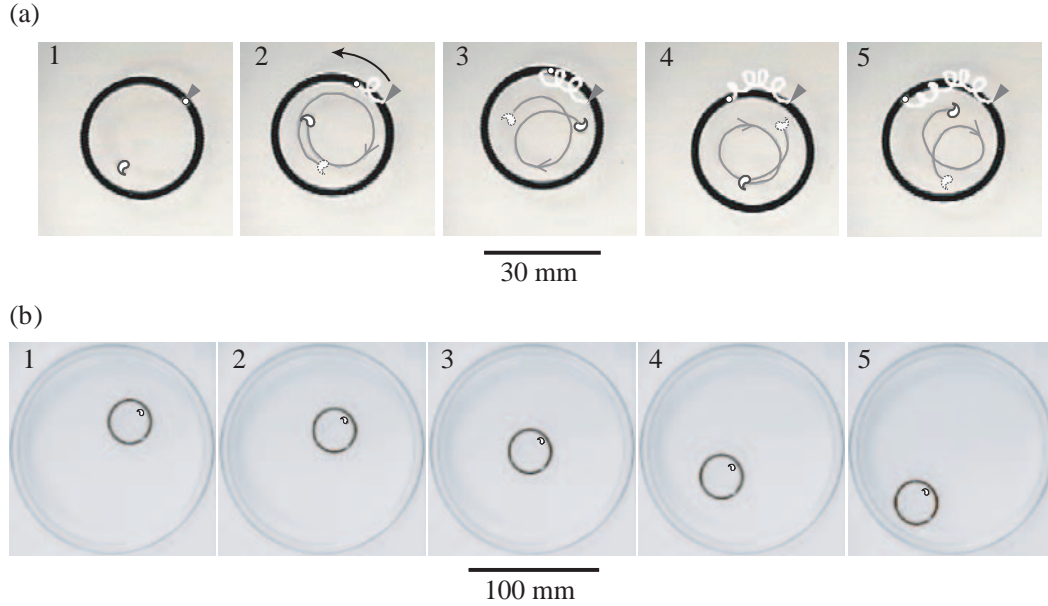
Figure 5.8: Snapshots of the spontaneous motion of a circular ring and an encircled camphor fragment under two different initial conditions. (a) Counterclockwise rotation of the circular ring (ring α) and clockwise rotation of the camphor fragment when the camphor fragment was placed onto the water surface before the ring (ring α). The white line denotes the trajectory of a point marked on the circular ring. The location of the point in 1 is indicated by an arrow in each snapshot. The trajectory of the camphor motion from the previous snapshot is shown by a gray line. (b) Intermittent motion of the circular ring with a camphor fragment when the circular ring was placed onto the water surface before the camphor fragment. The time intervals between snapshots were (a) 3/2 s, and (b) 3 s in 1-2 and 1/3 s in 2-5 [8].

of the camphor disk is accelerated and the rightward motion is decelerated near the edges of the saw-tooth blades. The experimental results shown in Fig. 5.6 can be explained by this influence of the asymmetric boundary condition.

Next, the motion affected by the convection in two-dimensional system is considered [8].

Three mobile rings (circular ring: ring α, ratchet-shaped ring: ring β, mirror image of ring β: ring γ) were prepared with a plastic plate (thickness: 0.1 mm). A camphor grain with the shape of comma (,) and a mobile ring were put onto the water surface and the motion of the camphor grain was observed.

Figure 5.8 shows the snapshots of the synchronized spontaneous motion of a circular mobile ring (ring α) and a camphor fragment depending on the initial conditions. In Fig. 5.8(a), the camphor fragment moved clockwise at $2\pi/3$ rad s^{-1} on the water surface as an initial condition, and then the circular ring α was placed on the water surface to surround the camphor fragment. Under
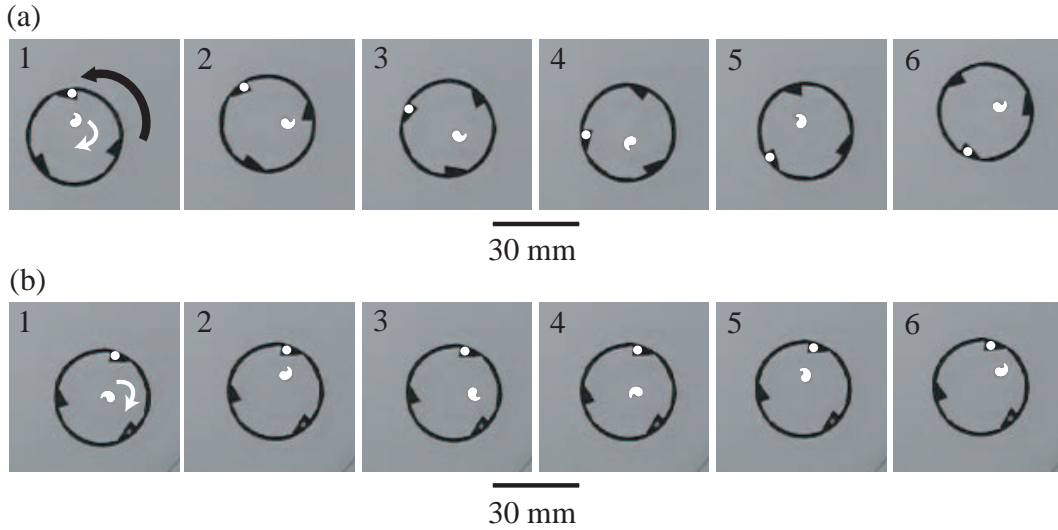
(a)

30 mm

(b)

30 mm

Figure 5.9: Snapshots of the spontaneous motion of an asymmetric ring and an encircled camphor fragment (time interval: 2.0 s). The shapes of the ring in (a) (ring β) and (b) (ring γ) are mirror images of each other when they are placed on the water surface. To visualize the motion of the circular ring, a point was marked on the ring [8].

this condition, the camphor fragment continued to move clockwise at $2\pi/5$ rad s^{-1} and the circular ring moved counterclockwise at $-\pi/30$ rad s^{-1}. In Fig. 5.8(b), the circular ring α was placed on the water surface as another initial condition, and the camphor fragment was placed on inside the ring settling on the water surface. Under this condition, the camphor fragment settled after slow movement for 10 min without rotation. The circular ring then maintained intermittent motion together with the camphor fragment for 30 min, i.e., settling of both the ring and the camphor fragment and rapid motion of them were repeated at an interval of ~ 30 s.

Figure 5.9 shows the snapshots of the synchronized motion between an asymmetric ring and a camphor fragment. In these experiments, a camphor fragment was placed and then the ring was introduced to surround the fragment. In Fig. 5.9(a), the ring rotated in the direction opposite the rotation of the camphor fragment. In contrast, the camphor fragment continued to rotate while the ring almost did not move under the experimental condition in Fig. 5.9(b).

Figure 5.10(a) shows the trajectories of a camphor fragment, a circular ring, and two talc powders for visualization on a water surface. In this experiment, the initial conditions are the same as those in Fig. 5.8(a). Convective flow was observed along the inner side of the ring in the same rotational direction as that of the ring. Figure 5.10(b) shows the trajectories of the talc powders during the resting state of the circular ring and the camphor fragment when the initial conditions are the same as those in Fig. 5.8(b). Although the camphor fragment
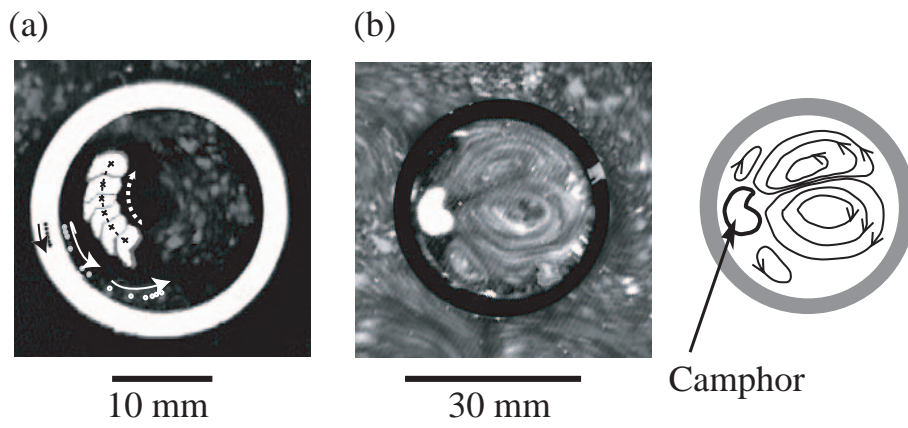
(a)   (b)

10 mm   30 mm

Camphor

Figure 5.10: (a)Trajectories of the camphor fragment, ring, and two talc powders on the water surface. In this experiment, the initial conditions are the same as those in Fig. 5.8(a), and talc powders (diameter: 3-7 μm) were homogeneously added to the water surface to visualize the convective flow driven by the concentration difference of the camphor layer that developed from the solid fragment. Convective flow was observed along the inner side of the ring in the same rotational direction as that of the circular ring (time interval: 1/15 s). (b)Trajectories of the movements of talc powders to visualize the convective flow generated around a camphor fragment in the resting state of the circular ring and the camphor fragment on the water surface for a duration of 25 s. The camphor grain exhibits intermittent motion as in Fig. 5.8(b) [8].

was settled in the circular ring, convective flow circulated from the location of the camphor fragment.

Figures 5.8(a) and 5.10(a) suggest that convective flow, where the direction is opposite that of camphor rotation, is maintained around the camphor fragment even after the circular ring is placed, and therefore the convective flow drives the circular ring. By adding the ratchet to the circular ring, the effects of the flow can increase or decrease depending on the direction of the ratchet as shown in Fig. 5.9. In contrast, Figs. 5.8(b) and 5.10(b) suggest that the surface tension around the camphor fragment reaches a balanced state because of the narrow surface area within the circular ring and therefore the camphor fragment is at rest immediately after the camphor fragment is placed inside the floating ring. Next, convective flow increases since the local settling of the camphor fragment increases the concentration gradient of the camphor layer around the camphor fragment, while circulating flow around the camphor fragment may maintain this settling, as seen in Fig. 5.10(b). When the concentration of the camphor layer reaches a critical concentration, the excess camphor layer develops locally out of the circular ring and the balanced state is destroyed. Therefore, the circular ring may move rapidly in a certain direction.

These spontaneous motions of a camphor grain and an encircled ring are clearly affected by the convection induced by the camphor grain. So far, we cannot reproduce these phenomena by numerical calculation, because the system is quite complicated, however, by reducing the effects of the convection, I hope that we can clearly describe the effects of the convective flow.

Chapter 6

Spontaneous motion of a droplet in the other systems

In this chapter, three examples where chemical energy is transduced into mechanical energy, or motion [4]. The first example is the spontaneous motion of an alcohol droplet on the aqueous phase [10], the second one is the spontaneous motion of an oil droplet on a glass substrate in the surfactant solution [11], and the last one is the spontaneous motion of a phenanthroline disk on the aqueous phase [9]. These motions can be explained as the energy transduction from chemical energy into mechanical energy through interfacial tension in reaction-diffusion systems. Although the convective flow is not explicitly considered in this chapter, the spontaneous motion can be regarded as convective flow in a wide sense. Therefore, they are introduced in this chapter.

6.1 Spontaneous motion in an alcohol-water system

It is well known that alcohol has much lower surface tension than water, and that mixtures of alcohol and water show many interesting phenomena, such as "tears of wine" [75, 76]. When alcohol with a rather long hydrocarbon chain is used, the oscillation of the surface tension is reported both experimentally and theoretically [77–79].

A droplet of alcohol with a long hydrocarbon chain can be formed on water for a rather long time. We adopted the pentanol as alcohol, and noticed the formation of the droplet on aqueous phase. In this section, the spontaneous motion of such a droplet is presented.

We added pentanol to water in a petri dish and observed the phenomena inside it as shown in Fig. 6.1(a). Initially, the pentanol immediately mixes with water. After a near-saturating amount of pentanol is added, the pentanol does

(a)

observation

water   pentanol droplet

(b)   i)   small droplet
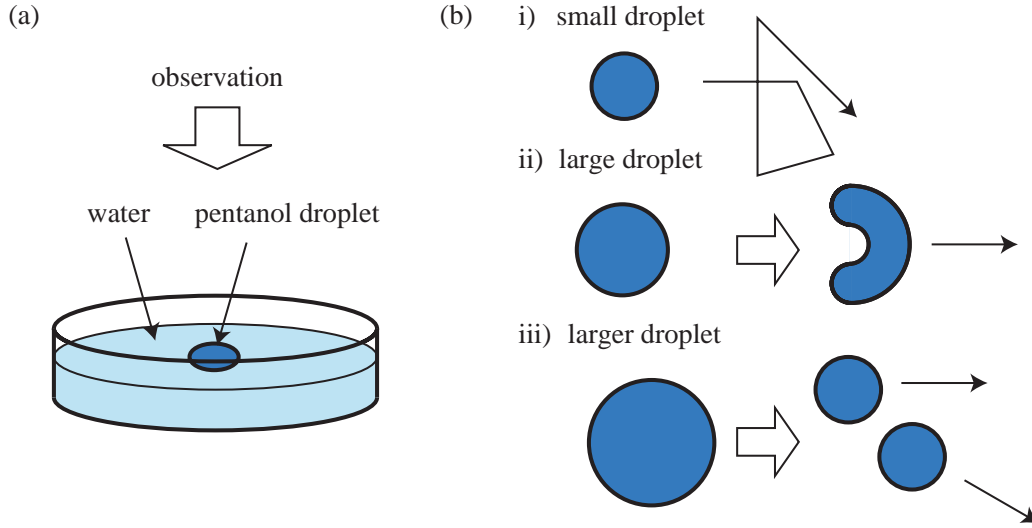
ii) large droplet

iii) larger droplet

Figure 6.1: Spontaneous motion of a pentanol droplet on water. (a) Rough sketch of the experimental setup. Images are taken from above. (b) i) A small droplet maintains a circular shape and moves irregularly. ii) A larger droplet deforms into a "hat (^)" and moves in one direction. iii) A much larger droplet divides into smaller droplets and they move around [4, 10].

not mix any further with the solution, and a droplet is formed. The droplet does not stand still but rather moves around, as shown schematically in Fig. 6.1 (b).

The feature of this spontaneous motion of a droplet is depending on the size of the droplet. A small droplet maintains a circular shape and moves irregularly. A larger droplet deforms like a "hat (^)" shape and moves in one direction. A much larger droplet divides into smaller droplets and moves around as shown schematically in Fig. 6.1 (b). The experimental results are exhibited in Fig. 6.2.

This mode change in spontaneous motion depending on the size of the droplet can be understood by considering the instability for the perturbation. Here, the straight interface with a small perturbation is assumed and the following two factors are considered. In order to simplify the treatment, we adopt the approximation that the shape of the wave consists of parts of a circle as shown schematically in Fig. 6.3.

The first factor is the process of the minimizing the alcohol-water interface. Here, the strength of the force per unit length is let as γ_1. In this case, the radius of the circle, R, and the length of the interface per wave length, L, shown in Fig. 6.3, are derived as

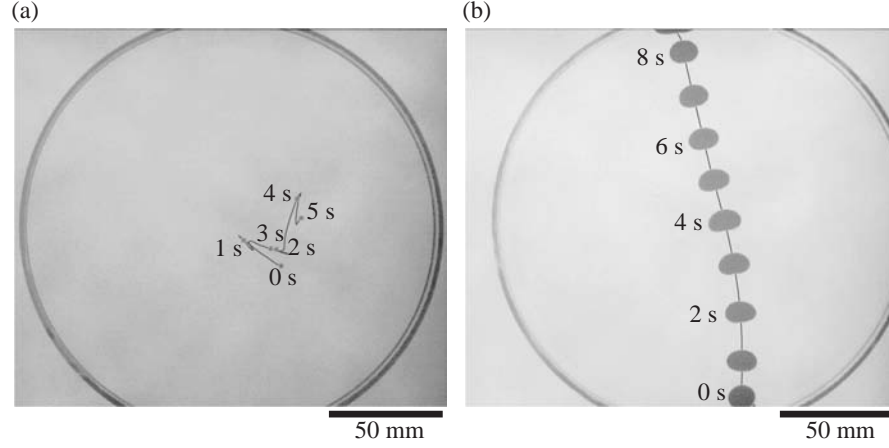$$R = \frac{A^2 + (\pi/2k)^2}{2A} \approx \frac{\pi^2}{8Ak^2},$$

(6.1)

Figure 6.2: Spontaneous motion of an alcohol droplet on water-alcohol mixture. (a) When a droplet is smaller, it moves irregularly. (b) When a droplet is larger, it deforms and moves in one direction. The pentanol was mixed with ink in order to visualize the droplet [10].

$$L = 4R \arcsin\left(\frac{\pi/2k}{R}\right) \approx \frac{2\pi}{k}\left(1 + \frac{8A^2 k^2}{3\pi^2}\right). \tag{6.2}$$

Supposing that γ_1 is proportional to $\partial\left[L/\left(2\pi/k\right)\right]/\partial A$,

$$\gamma_1 = a\frac{\partial}{\partial A}\left(\frac{L}{2\pi/k}\right) = aAk^2, \tag{6.3}$$

where a is a constant.

The second factor is the concentration gradient of the pentanol at the surface depending on the curvature of the water-alcohol interface. The pentanol dissolves from the droplet to the surface of the aqueous phase, and then it is sublimated to the air or dissolved to the aqueous phase. These processes can be written as follows:

$$\frac{\partial c}{\partial t} = D\nabla^2 c - \alpha\left(c - c_{\mathrm{a}}\right) - \beta\left(c - c_{\mathrm{w}}\right), \tag{6.4}$$

where c is the surface concentration of the pentanol, D is the diffusion coefficient of pentanol on the surface, α is the evaporation rate of pentanol, β is the dissolution rate of pentanol, c_{a} is the concentration at the gas-liquid equilibrium and c_{w} is the concentration at the surface-bulk equilibrium in the aqueous phase. By assuming the steady state with the Dirichlet boundary condition at the pentanol-water interface, i.e., $c = c_0$ at the interface, the concentration gradient can be calculated using modified Bessel functions for a certain curvature. It is noted that the dissolution process of the pentanol from the droplet corresponds to the adopted boundary condition in the steady state. In the convex region, the concentration gradient is larger than that in the concave region,
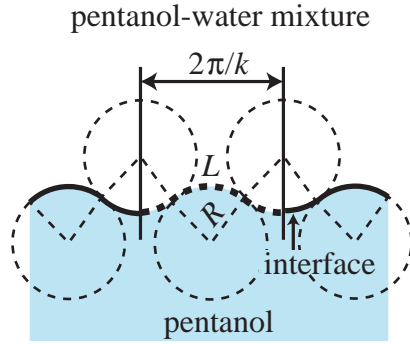
Figure 6.3: Schematic illustration of the tractable model. The perturbation from the straight interface is considered. The sine wave with the wave number k is approximated as the combination of the parts of circles [10].
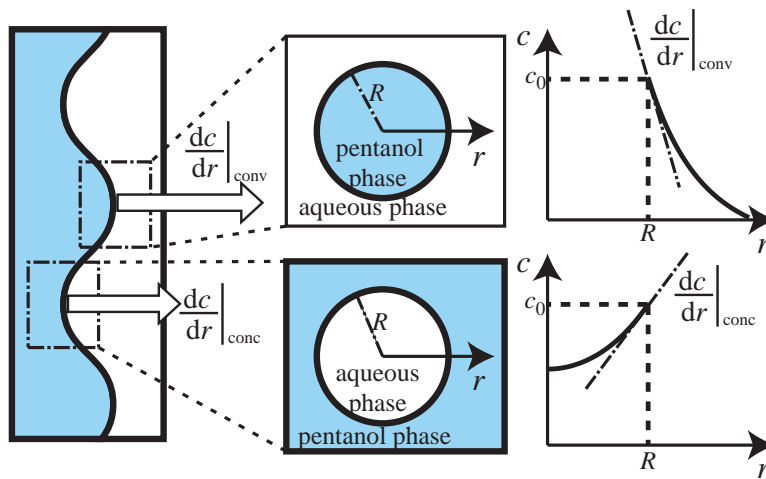

Figure 6.4: Schematic representation on the interfacial tension difference. As the interface is assumed to be circular with the radius of R, the concentration profile is $(c_0 - \Gamma) K_0(\sqrt{(\alpha + \beta)/D}r)/K_0(\tilde{R})$ at the convex region (upper), and $(c_0 - \Gamma) I_0(\sqrt{(\alpha + \beta)/D}r)/I_0(\tilde{R})$ at the concave region (lower), where K and I are modified Bessel functions. The interfacial tension is nearly proportional to the gradient of the concentration at the interface [10].

which means the perturbation of the interface tends to grow as schematically shown in Fig. 6.4. As the force strength per unit length is γ_2, it is described as

$$\gamma_2 = b \left[\left| \left(\left. \frac{dc}{dr} \right|_{\text{conv}} \right) \right| - \left| \left(\left. \frac{dc}{dr} \right|_{\text{conc}} \right) \right| \right], \tag{6.5}$$

where $dc/dr|_{\text{conv}}$ is the concentration gradient perpendicular to the interface in the convex region, $dc/dr|_{\text{conc}}$ is that in the concave region, and b is a positive constant. By the analytic calculation, the following representation is obtained:

$$\gamma_2 = b \left(c_0 - \Gamma \right) \sqrt{\frac{\alpha + \beta}{D}} \left(\frac{K_1 \left(\tilde{R} \right)}{K_0 \left(\tilde{R} \right)} - \frac{I_1 \left(\tilde{R} \right)}{I_0 \left(\tilde{R} \right)} \right), \tag{6.6}$$

where $\Gamma = \left(\alpha c_{\text{a}} + \beta c_{\text{w}} \right) / \left(\alpha + \beta \right)$, $\tilde{R} = \sqrt{\left(\alpha + \beta \right) / D} R$ and I_0, I_1, K_0, K_1 are modified Bessel functions.

Here, it is assumed that $0 < kA = \delta \ll 1$. When $k \ll 1$,

$$\gamma_2 - \gamma_1 \approx -aAk^2 + \frac{8b\Gamma A k^2}{\pi^2}, \tag{6.7}$$

and when $k \gg 1$,

$$\gamma_2 - \gamma_1 \approx -aAk^2 + \frac{8b\Gamma A k^2}{\pi^2 \ln \left[8Ak^2 / \left(\pi^2 \sqrt{\left(\alpha + \beta \right) / D} \right) \right]}. \tag{6.8}$$

This means $\gamma_2 - \gamma_1 < 0$ when $k \gg 1$, and $\gamma_2 - \gamma_1 > 0$ when $k \ll 1$. By setting $\gamma_2 - \gamma_1 = 0$ at $k = k_{\text{c}}$, k_{c} is obtained as follows:

$$k_{\text{c}} = \frac{\pi^2}{8\delta} \sqrt{\frac{\alpha + \beta}{D}} \exp \left[\frac{3b \left(c_0 - \Gamma \right)}{2a} \right]. \tag{6.9}$$

When the droplet size is smaller than $2\pi/k_{\text{c}}$, the droplet is stable and does not deform. On the other hand, when it is larger than $2\pi/k_{\text{c}}$, the fluctuation of a certain mode grows and the droplet can separate into several smaller droplets. Just when the droplet size is around $2\pi/k_{\text{c}}$, only one mode is destabilized. In such a case, a droplet is deformed into the shape of a "hat(ˆ)" and moves in one direction.

The mode change in spontaneous motion depending on the size of the droplet can be understood based on the reaction-diffusion equations. The results can predict the experimental trends when the temperature or concentration of the aqueous phase is changed. In fact, such experiments have been performed, and the theoretical prediction has been confirmed, though the experimental data are not shown in this thesis.

Thus, in this framework, the convective flow is not considered, but the strong convective flow is confirmed in the experiments. By considering the convective flow, various modes of spontaneous motion may be achieved.
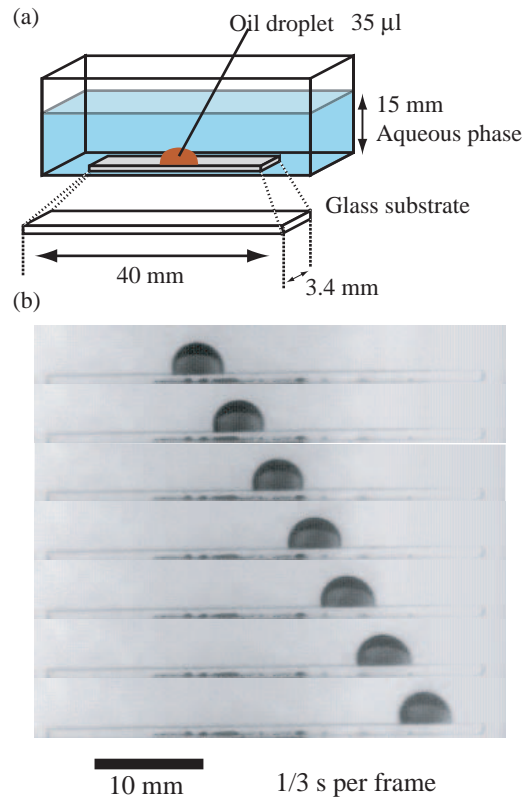
Figure 6.5: Spontaneous motion of an oil droplet on a glass substrate. (a) Schematic illustration on the experimental setup. (b) Snapshots of an oil droplet from side every 1/3 s. The droplet moves spontaneously almost at a constant velocity in one direction [4, 84].

6.2   Spontaneous motion in an oil-water system

There have been some reports on reactive droplets on a glass plate [80, 81]. However, such reactive droplets cannot cross their own trails; i.e., they show a self-avoiding trajectory. On the other hand, as a droplet of nitrobenzene including iodine (I_2) and saturated potassium iodide (KI) is put onto a glass substrate in an aqueous solution of surfactant such as stearyltrimethylammonium chloride (STAC) solution, the oil droplet exhibits ameba-like motion [82, 83]. When the oil droplet is put onto the long rectangular glass substrate, the droplet goes back and forth as shown in Fig. 6.5 [84].

We have also experimentally observed that the chemo-sensitive motion of an oil droplet on a glass substrate treated by acid. It was found that an oil droplet can show turning back motion, stopping motion, and slowing motion when the substrate was partially treated with acid as shown in Fig. 6.6. With detailed observations, however, it turned out that the motion of an oil droplet severely depends on the condition of the substrate, which was hard to control

experimentally.

Here, the mechanism of the droplet motion is considered. The oil droplet moves dissolving adhered STA^+ ions on the glass substrate. Since STA^+ and I_3^- in the organic phase make an ion-pair, a difference in interfacial energy arises from the difference in the concentration of STA^+ ions on the glass surface between the front and back of an oil droplet. Thus, the condition of the glass surface on which STA^+ ions aggregate plays an important role in the motion of an oil droplet. The stopping and slowing of an oil droplet can be attributed to the effect of inertia, which moves the oil droplet to the area where there are not enough STA^+ ions on the glass surface to produce a driving force. Furthermore, the dependence of the droplet motion on the condition of the acid-treated region can be attributed to the difference in the number of adsorption sites on the glass surface.

Based on the above discussion, we make a simple one-dimensional model. The x axis is set along the surface of the glass substrate. The droplet proceeds on a line with stretching and shrinking. The positions at the both ends of the droplet are set as $x_1(t)$ and $x_2(t)$, where $x_1 < x_2$. The concentration of STA^+ ions on the glass surface is set as $u(x, t)$. The dynamics of x_1 and x_2 are written as follows:

$$\rho \frac{d^2 x_1}{dt^2} = -\mu_0 \frac{dx_1}{dt} - \left. \frac{\partial E}{\partial x} \right|_{x=x_1} - \beta(r_0)(x_1(t) - x_2(t) - r_0), \tag{6.10}$$

$$\rho \frac{d^2 x_2}{dt^2} = -\mu_0 \frac{dx_2}{dt} - \left. \frac{\partial E}{\partial x} \right|_{x=x_2} - \beta(r_0)(x_2(t) - x_1(t) + r_0), \tag{6.11}$$

where ρ, μ_0, and r correspond to the surface density, viscosity, and the diameter of the oil droplet, respectively. $\beta(r)$ is the elastic constant of the oil droplet with the diameter r_0 in the equilibrium state [11]:

$$\beta(r) = \frac{2\gamma w}{r}. \tag{6.12}$$

$E(u)$ is the surface energy of the glass surface modulated by the STA^+ ions adsorbed on it:

$$E(u) = \frac{e_0}{1 + au^m}, \tag{6.13}$$

where e_0, a and m are the positive constants. On the other hand, the dynamics of u is written as follows:

$$\frac{\partial u}{\partial t} = d\frac{\partial^2 u}{\partial x^2} + F(u, x, x_1(t), x_2(t); \ell_0), \tag{6.14}$$

where d is the diffusion constant of the STA^+ ions molecules on the glass surface. $F(u, x, x_1(t), x_2(t); \ell_0)$ corresponds to the desorption of the STA^+ ions
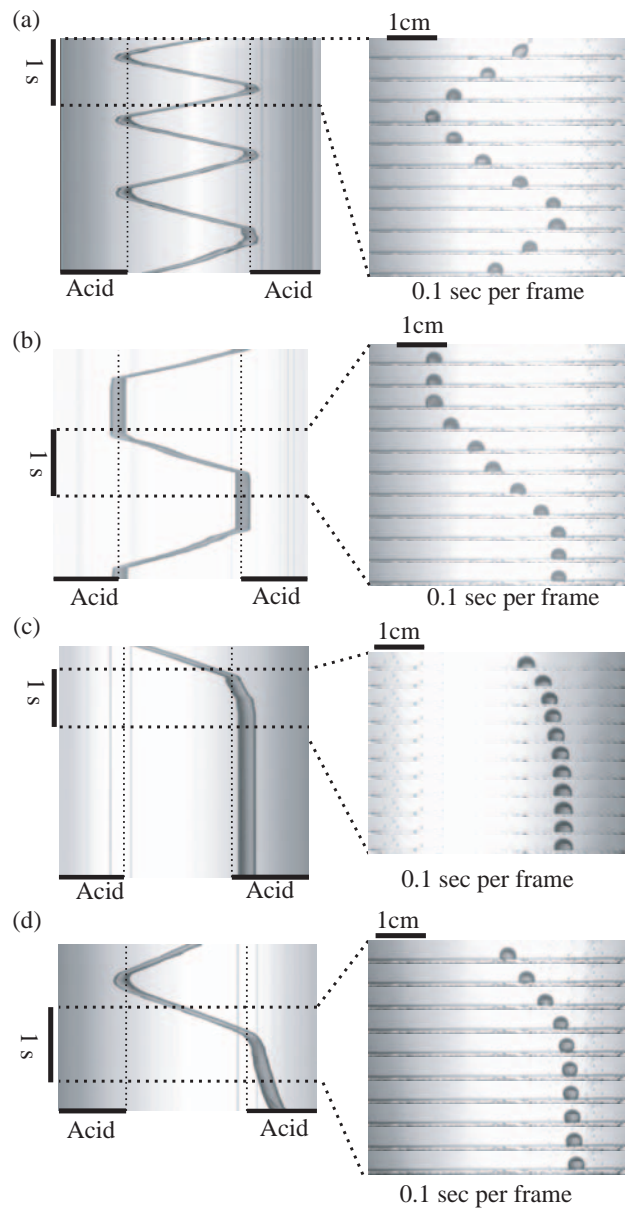
Figure 6.6: Experiments on spontaneous droplet motions. A 15-μl oil droplet was put onto a narrow acid-treated glass substrate. Images from the experiment and a spatio-temporal image of oil-droplet motion are shown. An oil droplet showed (a) shuttling motion, (b) intermittent shuttling motion, (c) stopping, and (d) slowing [11].
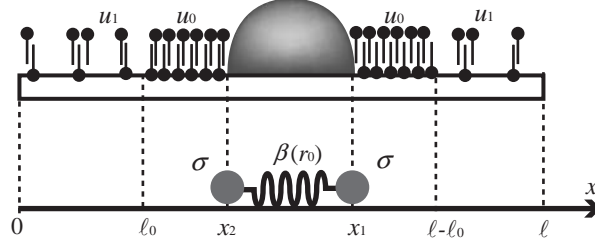
Figure 6.7: Schematic diagram of the model of oil-droplet motion on a glass surface. The lower arrow represents the spatial coordinate, where 0 to ℓ_0 and $\ell - \ell_0$ to ℓ are treated with acid. u_0 and u_1 are the saturated concentration of the STA$^+$ ions on the glass substrate on bare and acid-treated glass substrate, respectively. The oil droplet is modeled as two lines (perpendicular to x-axis, whose mass density is σ, connected to a spring with an elastic constant of $\beta(r_0)$) [11].

from the glass surface to the oil droplet. For this term, we assume the following description:

$$F(u, x, x_1(t), x_2(t); \ell_0) = \begin{cases} -k_1 u, & (x_2(t) \le x \le x_1(t)) \\ k_2(u_0 - u), & (\ell_0 < x < x_2(t),\ x_1(t) < x < \ell - \ell_0) \\ k_3(u_1 - u), & (0 < x \le \ell_0,\ \ell - \ell_0 \le x < \ell) \end{cases}$$
(6.15)

where k_1, k_2, u_0, u_1, ℓ and ℓ_0 are the positive constants that correspond to the desorption rate, adsorption rate, saturated concentration of the STA$^+$ ions on the bare glass surface, that on the acid-treated glass surface, the length of the glass substrate, and the length of the glass substrate treated with acid, respectively (see Fig. 6.7). The initial and boundary conditions are set as

$$\frac{\partial u}{\partial x}(t, 0) = \frac{\partial u}{\partial x}(t, \ell) = 0,$$
(6.16)

$$u(0, x) = \begin{cases} u_0, & (\ell_0 < x < \ell - \ell_0) \\ u_1, & (0 < x \le \ell_0,\ \ell - \ell_0 \le x < \ell) \end{cases}$$
(6.17)

$$x_1(0) = x_{10},\ \ x_2(0) = x_{20}(< x_{10}),$$

$$\frac{\mathrm{d}x_1}{\mathrm{d}t}(0) = \frac{\mathrm{d}x_2}{\mathrm{d}t}(0) = 0.$$
(6.18)

To normalize eqs. (6.10) - (6.18), we introduce the following dimensionless variables:

$$U = \frac{u}{u_0},\ X_1 = \frac{x_1}{\ell},\ X_2 = \frac{x_2}{\ell},\ X = \frac{x}{\ell},\ T = k_1 t.$$
(6.19)

We then derive the following dimensionless equations from eqs. (6.10) - (6.18):

$$\frac{\mathrm{d}^2 X_1}{\mathrm{d}T^2} = -\mu \frac{\mathrm{d}X_1}{\mathrm{d}T} - \frac{\partial E}{\partial X}\bigg|_{X=X_1} - B(R_0)(X_1(T) - X_2(T) - R_0),$$
(6.20)

$$\frac{\mathrm{d}^2 X_2}{\mathrm{d}T^2} = -\mu\frac{\mathrm{d}X_2}{\mathrm{d}T} - \frac{\partial E}{\partial X}\bigg|_{X=X_2} - B(R_0)(X_2(T) - X_1(T) + R_0), \qquad (6.21)$$

$$E(U) = \frac{E_0}{1 + AU^n}, \qquad (6.22)$$

$$\frac{\partial U}{\partial T} = D\frac{\partial^2 U}{\partial X^2} + F(U, X, X_1(T), X_2(T); L_0), \qquad (6.23)$$

$$F(U, X, X_1(T), X_2(T); L_0) = \begin{cases} -U, & (X_2(T) \le X \le X_1(T)) \\ K_2(U_0 - U), & (L_0 < X < X_2(T), \\ & \qquad X_1(T) < X < 1 - L_0) \\ K_3(U_1 - U), & (0 < X \le L_0, 1 - L_0 \le X < 1) \end{cases} \qquad (6.24)$$

with the following initial and boundary conditions:

$$\frac{\partial U}{\partial X}(T, 0) = \frac{\partial U}{\partial X}(T, 1) = 0, \qquad (6.25)$$

$$u(0, x) = \begin{cases} 1, & (L_0 < X < 1 - L_0) \\ U_1, & (0 < X \le L_0, 1 - L_0 \le X < 1) \end{cases} \qquad (6.26)$$

$$X_1(0) = X_{10}, \quad X_2(0) = X_{20}(< X_{10}),$$

$$\frac{\mathrm{d}X_1}{\mathrm{d}T}(0) = \frac{\mathrm{d}X_2}{\mathrm{d}T}(0) = 0, \qquad (6.27)$$

where

$$\mu = \frac{\mu_0}{\sigma k_1}, \quad E_0 = \frac{e_0}{\ell\sigma k_1^2}, \quad R_0 = \frac{r_0}{\ell},$$

$$B(R_0) = \frac{\ell^2\beta(r_0)}{\sigma k_1^2} = \frac{W}{R_0}, \quad W = \frac{2\gamma w\ell}{\sigma k_1^2}, \quad A = au_0^n,$$

$$D = \frac{d}{k_1\ell^2}, \quad K_2 = \frac{k_2}{k_1}, \quad K_3 = \frac{k_3}{k_1}, \quad U_1 = \frac{u_1}{u_0},$$

$$L_0 = \frac{\ell_0}{\ell}(< 1), \quad X_{10} = \frac{x_{10}}{\ell}, \quad X_{20} = \frac{x_{20}}{\ell}.$$

We performed a numerical simulation using eqs. (6.20) - (6.24) under the initial and boundary conditions shown in eqs. (6.25) - (6.27).

We only changed the parameter U_1, while all of the other parameters were fixed. It is noted that U_1 corresponds to the saturated concentration at the region treated by acid. Spatio-temporal plots of the droplet given by the numerical calculations are shown in Fig. 6.8.

When U_1 is small enough, i.e., it is difficult for STA$^+$ ions to adsorb to the acid-treated region, the oil droplet moves back and forth inside the untreated region, as shown in Fig. 6.8(a). As U_1 increases slightly, the oil droplet does not turn back quickly but rather rests at the border between the acid-treated region and the untreated region. After a brief stop, it begins to move backward, and this intermittent shuttling motion is repeated as shown in Fig. 6.8(b). For
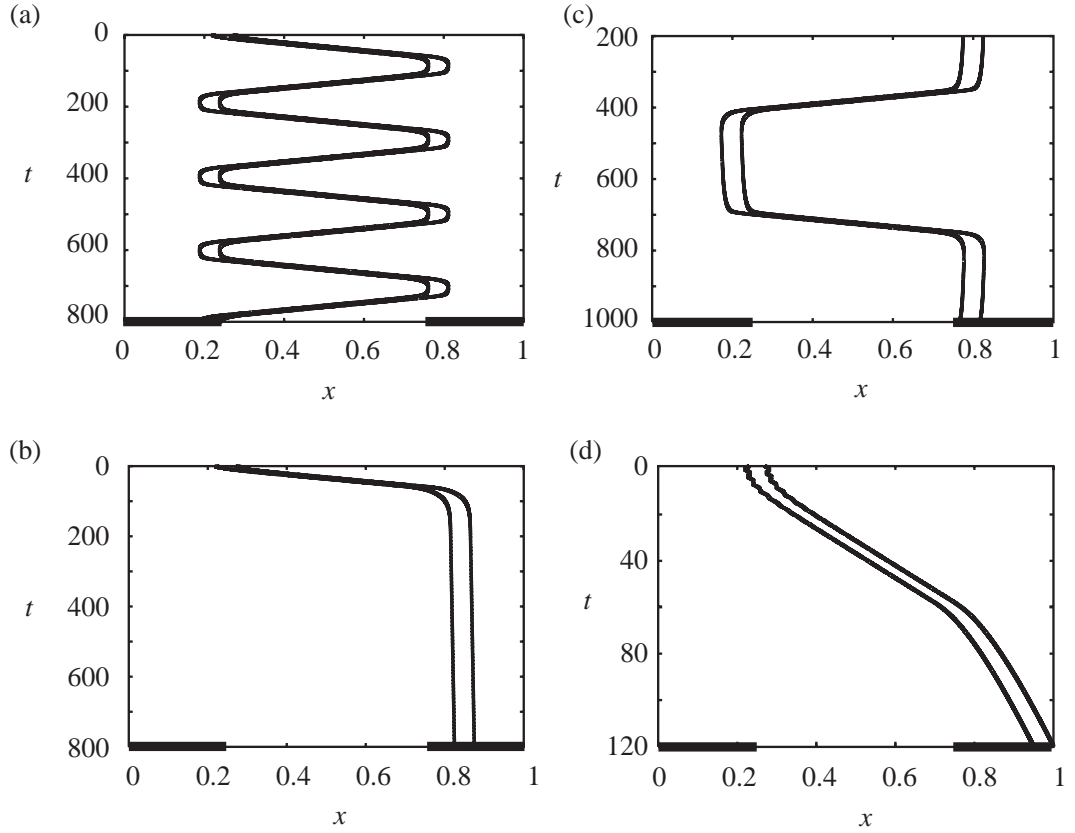
Figure 6.8: Spatio-temporal plots of the results by the numerical calculations using eqs. (6.20) - (6.27). Only the parameter U_1 was changed as (a) $U_1 = 0.65$, (b) $U_1 = 0.658$, (c) $U_1 = 0.68$ and (d) $U_1 = 0.75$. The other parameters are $\mu = 0.2$, $R = 0.05$, $E_0 = 5 \times 10^{-5}$, $A = 1$, $m = 4$, $B(R) = 2$, $D = 2.5 \times 10^{-7}$, $L_0 = 0.25$, $U_0 = 1$, $K_2 = 1$, $K_3 = 1$, $X_{10} = 0.23$, and $X_{20} = 0.27$. The thick lines along the x axis correspond to the regions treated with acid [11].

much larger U_1, the oil droplet does not go back any more, as shown in Figs. 6.8(c) and (d). The oil droplet goes into the acid-treated region and it moves on very slowly or stops according to the value of U_1.

In this system, the difference in the chemical energy of the dissolution of the surfactants between the water phase and oil phase is transduced into motion. We hope that we can discuss the efficiency of the chemo-mechanical energy transduction using the developed model.

6.3   Spontaneous motion coupled with a chemical reaction

1,10-phenanthroline ($C_{12}H_8N_2$) is used for making the ferroin, which is often used as a catalyst of BZ reaction. Putting phenanthroline and ferrous sulfate ($FeSO_4$) into pure water, they make a complex at a ratio of 3:1. A phenanthroline molecule has hydrophobic parts and hydrophilic parts, and it has the surface activity like camphor. Thus, as a disk of phenanthroline is put onto the water, it moves spontaneously. In this section, we report the spontaneous motion of a phenanthroline disk on pure water or ferrous sulfate solution, and the mode change of the spontaneous motion according to the change in the concentration of $FeSO_4$.

When the concentration of $FeSO_4$ is low enough, the uniform motion of the grain was observed. With the increase in the concentration of $FeSO_4$, the uniform motion changed to intermittent motion (periodic change between motion and rest) and its period and resting time increased. However, this intermittent motion reverted to uniform motion and the velocity increased with a further increase in [$FeSO_4$]. The mechanism of this characteristic motion depending on [$FeSO_4$] is discussed in relation to the surface tension, which depends on the concentration of a surface-active layer composed of 1,10-phenanthroline and a tris-(1,10-phenanthroline) iron complex ([$Fe(phen)_3$]$^{2+}$, ferroin) as the driving force and the solubility of ferroin in the aqueous phase.

Figure 6.9 shows the snapshots for (a) uniform motion ([$FeSO_4$]= 0 mol l^{-1}), (b) intermittent motion ([$FeSO_4$= 5 mmol l^{-1}), and (c) uniform motion ([$FeSO_4$= 100 mmol l^{-1}) of the spontaneous motion of the phenanthroline disk together with the time variation of its velocity. As for the uniform motion, a red colored layer, which was composed of ferroin, was remained on the trajectory of the motion. On the intermittent motion, the density of the red colored layer around the disk increased at the resting state, but the resting state was changed to the rapid motion when the density of the red colored layer reached to a critical value, as seen in Fig. 6.9(b).

Figure 6.10 shows the mode diagram of the spontaneous motion of the phenanthroline disk depending on [$FeSO_4$]. The velocity of uniform motion decreased with the increase in [$FeSO_4$], and changed to intermittent motion (periodic change between motion and rest) at [$FeSO_4$] =3 mmol l^{-1}. Here, we
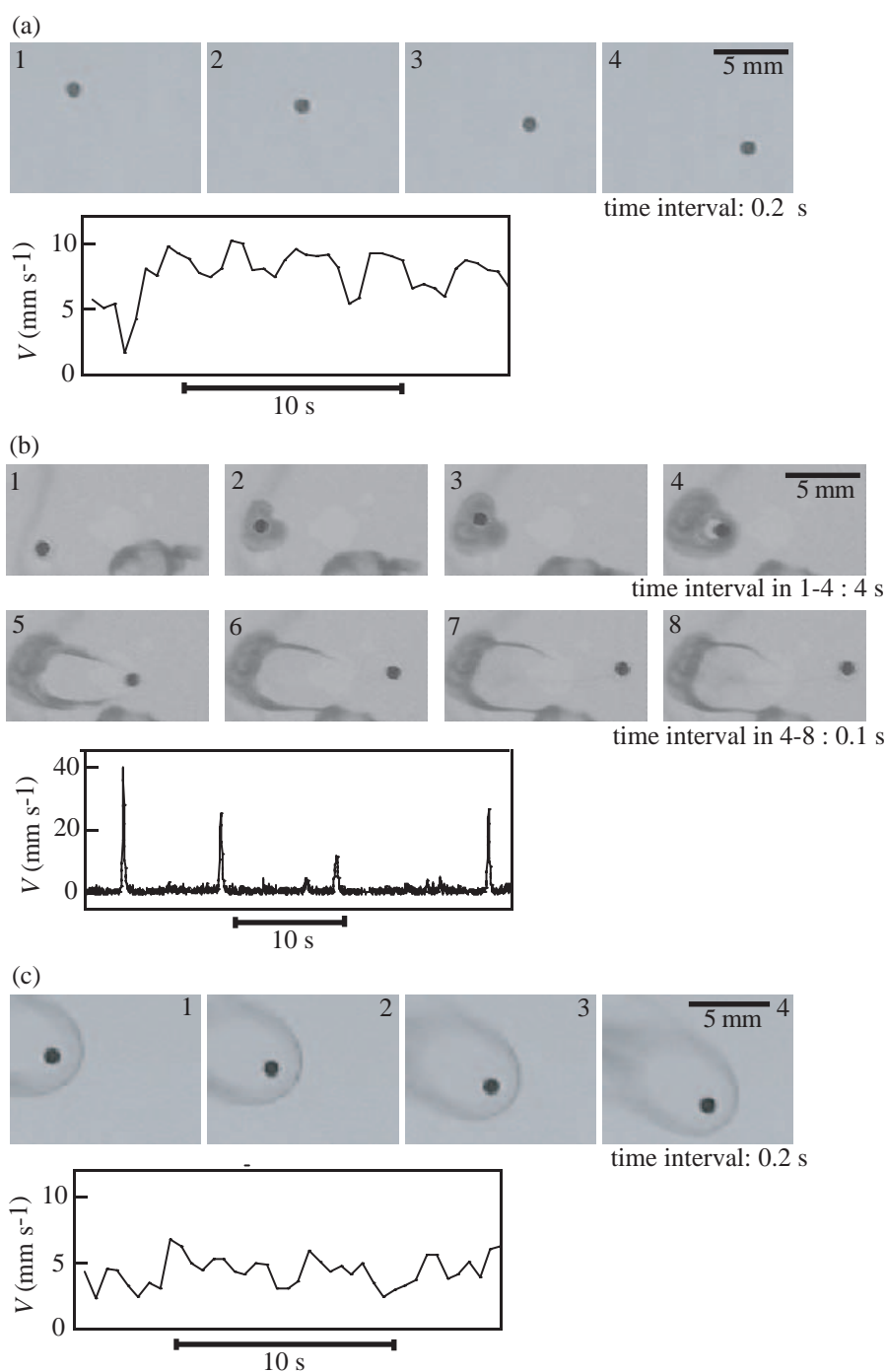
Figure 6.9: Snapshots of the spontaneous motion of a phenanthroline disk on the $FeSO_4$ aqueous solution at different concentrations ((a) 0, (b) 5, and (c) 100 mmol l^{-1}) (top view) together with the time variation of the velocity of the phenanthroline disk [9].
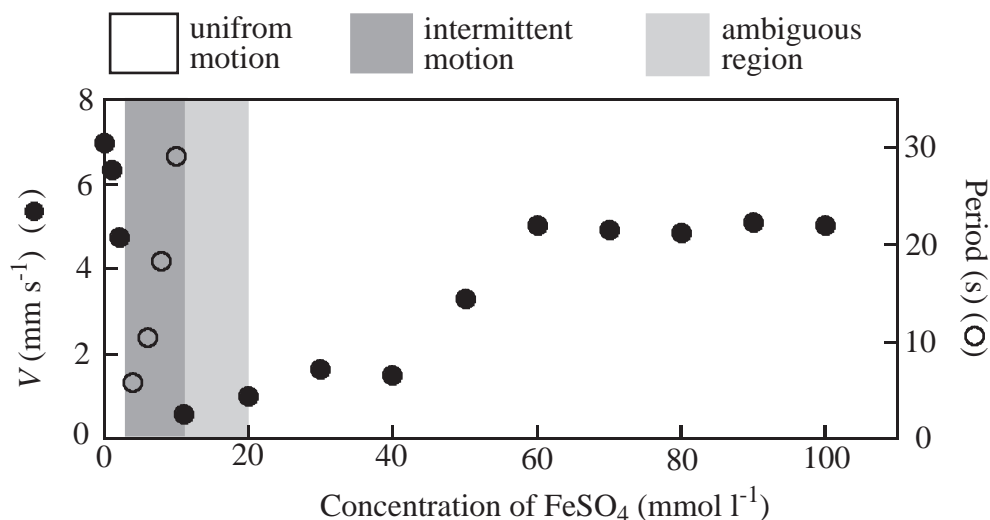
Figure 6.10: The mode of the spontaneous motion of a phenanthroline disk depending on [FeSO$_4$]. The velocity of uniform motion ($0 \leq$ [FeSO$_4$] ≤ 2, $30 \leq$ [FeSO$_4$] ≤ 100 mmol l^{-1}) including the ambiguous region ($11 \leq$ [FeSO$_4$] ≤ 20 mmol l^{-1}), and the frequency of intermittent motion ($3 \leq$ [FeSO$_4$] ≤ 10 mmol l^{-1}) are plotted [9].

determined as the ambiguous motion if the velocity of the motion was lower than 1 mm s^{-1} and the resting time of the intermittent motion was higher than 1 min. The frequency of intermittent motion decreased and the resting time increased with the further increase in [FeSO$_4$], and the phenanthroline disk almost settled at [FeSO$_4$] $= 10$ mmol l^{-1}. However, the uniform motion reverted again over [FeSO$_4$] $= 30$ mmol l^{-1}, and the velocity increased with the further increase in [FeSO$_4$].

The mechanism of this spontaneous motion can be described as a reaction-diffusion system with convection. The phenomenon of the spontaneous motion of a phenanthroline disk is interesting because the formation of the reaction product and the convective flow can be easily observed. We hope that the system will be designed where the spontaneous motion of a phenanthroline disk and oscillation or spatio-temporal pattern formation in BZ reaction can interact with each other, and create a novel spatio-temporal pattern.

Part III

Boundary Effects on Reaction-Diffusion Systems

Chapter 7

Slowing and stopping of a chemical wave in a narrowing canal

In Part III, the geometrical effects of boundary in reaction-diffusion systems are exemplified. In this chapter, the slowing and stopping of the chemical wave in the narrowing glass capillary is presented in BZ reaction. The mechanism is theoretically analyzed related to the surface-volume ratio.

7.1 Introduction

It has been claimed that the essence of the neuronal system can be understood in terms of a simple differential equation as a kind of reaction-diffusion systems [31–33]. Thus, a neuronal pulse is a manifestation of a dissipative structure generated in nonequilibrium open systems. Several experimental and theoretical studies have been undertaken on the reaction-diffusion systems as a model of the neuronal system. It is known that the FitzHugh-Nagumo equation can well reproduce the features.

In such studies, the Belousov-Zhabotinsky (BZ) reaction is often used as an experimental model of the reaction-diffusion systems. In this system, chemical waves propagate at a constant velocity and amplitude, and thus exhibit the characteristics similar to those of pulses in nerve cells. The characteristics of the BZ reaction can be well described using a numerical model, the Oregonator. The Oregonator model has a mathematical structure similar to the FitzHugh-Nagumo equation. Therefore, to better understand information processing in the neuronal system, it may be useful to compare it with the chemical waves in the BZ reaction, although there exists a fundamental difference between them: a neuronal pulse propagates on the two-dimensional tubular membrane and a chemical wave propagates in the three-dimensional bulk phase.
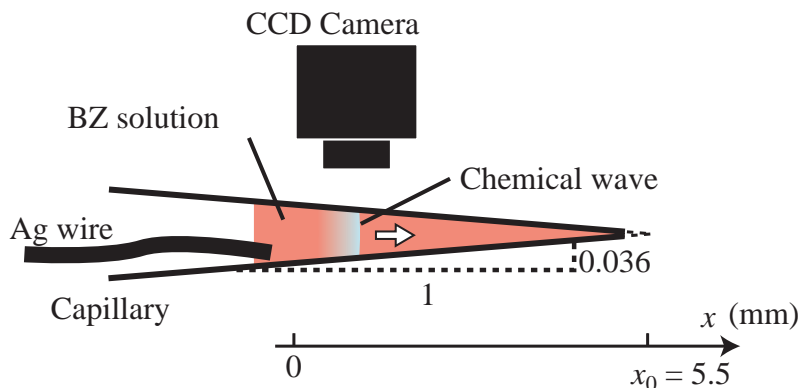
Figure 7.1: Schematic representation of the experimental system. The capillary was arranged horizontally and observed from above by a CCD camera [5].

Over the past decade, the behavior of the chemical waves in a narrow space has been studied using a gel system [34,35], a droplet system [36], and a bead system [37,38]. Tóth and co-workers reported that a chemical wave does not propagate when it expands from a thin capillary to the bulk solution. They claimed that a chemical wave can perform information processing [85,86]. Masere et al. performed experiments on the propagation of a chemical wave in a vertical capillary. They discussed their experimental results with special emphasis on the gravitational effect [87]. In these previous studies, the features of the chemical-wave propagation in a narrow straight capillary with a constant diameter were examined.

In this chapter, we show that a chemical wave slows, stops, and then disappears in a narrowing glass capillary. We discuss this phenomenon in term of the surface-volume ratio for the reaction field, i.e., the surface can seriously affect chemical wave propagation.

7.2 Experiments

All chemicals were analytical-grade reagents and used without further purification. An aqueous solution of ferroin, or tris (1,10-phenanthroline) iron (II) sulfate, was prepared by mixing stoichiometric amounts of 1,10-phenanthroline ($C_{12}H_8N_2$) and ferrous sulfate ($FeSO_4$) in pure water. The water was purified with a Millipore-Q system. BZ medium contained 0.35 M sodium bromate ($NaBrO_3$), 0.39 M sulfuric acid (H_2SO_4), 0.12 M malonic acid ($CH_2(COOH)_2$), 0.05 M sodium bromide (NaBr), and 4.0 mM ferroin ($Fe(phen)_3^{2+}$) (excitable condition). We left the BZ solution for about 10 min and then stirred it to diminish the formation of bubbles in the solution.

We prepared a glass capillary (borosilicated glass, length: 100 mm, inner radius: 0.75 mm, Sutter Instrument Co.) with a decreasing width by pulling

a straight capillary with a Micropipette Puller (Model P-97/IVF, Sutter Instrument Co.). The both ends of the capillary were open and the gradient of the inner radius was 0.036. In order to make easier to show the experimental results, the x axis is set as shown in Fig. 7.1. The capillary was immersed in the BZ medium, fulfilled with the BZ medium inside it, and then situated on a horizontal plate for observation with a CCD camera (Digital Microscope Unit, Keyence). As soon as bubbles formed inside the capillary, we stopped the observation: the data reported in the present study are only from the experimental series without bubble formation. All the experiments were performed at the room temperature (20 ± 3 $^\circ$C). Images were recorded on a videotape and analyzed by an image processing system.

7.3   Results

A chemical wave was initiated at the wider end by a silver wire without disturbance. A chemical wave propagating toward the narrower end slowed, stopped, and eventually disappeared. The oxidized solution in the capillary then reverted to the reduced state. The spatio-temporal plot of images of the capillary along the long axis is shown in Fig. 7.2(a), and the snapshots in every 5.0 s are shown in Fig. 7.2(b). They clearly show that the velocity of the chemical wave gradually decreases before it stops. This feature was seen in every chemical wave initiated. With each subsequent wave, the position at which the chemical wave stopped tended to shift slightly toward the narrower end. Figure 7.3 shows the temporal change in the position (a) and velocity (b) of the chemical wave, and the velocity depending on the position (c). From the observation, the point where the chemical wave stops propagation, x_s, was 2.7 ± 0.2 mm. We have confirmed the reproducibility of the experimental trends through a number of repeated experiments.

7.4   Discussion

We discuss here the characteristic change in the manner of wave propagation in a glass capillary. According to an analysis with the Oregonator, the velocity of the chemical wave in the BZ reaction can be written as [88]:

$$v \approx \frac{1}{2} \left(k_5 HAD \right)^{1/2}, \tag{7.1}$$

where H is the concentration of hydrogen ion, A is the concentration of bromate ion, D is the diffusion constant of the activator, and k_5 is the rate constant of the component reaction, which is introduced as an autocatalytic process by summation of the two elemental processes in the Oregonator model [88]. Equation (7.1) is valid for a plane and steady traveling wave but does not apply to a wave that shows a change in velocity. By assuming that the concentration dependence
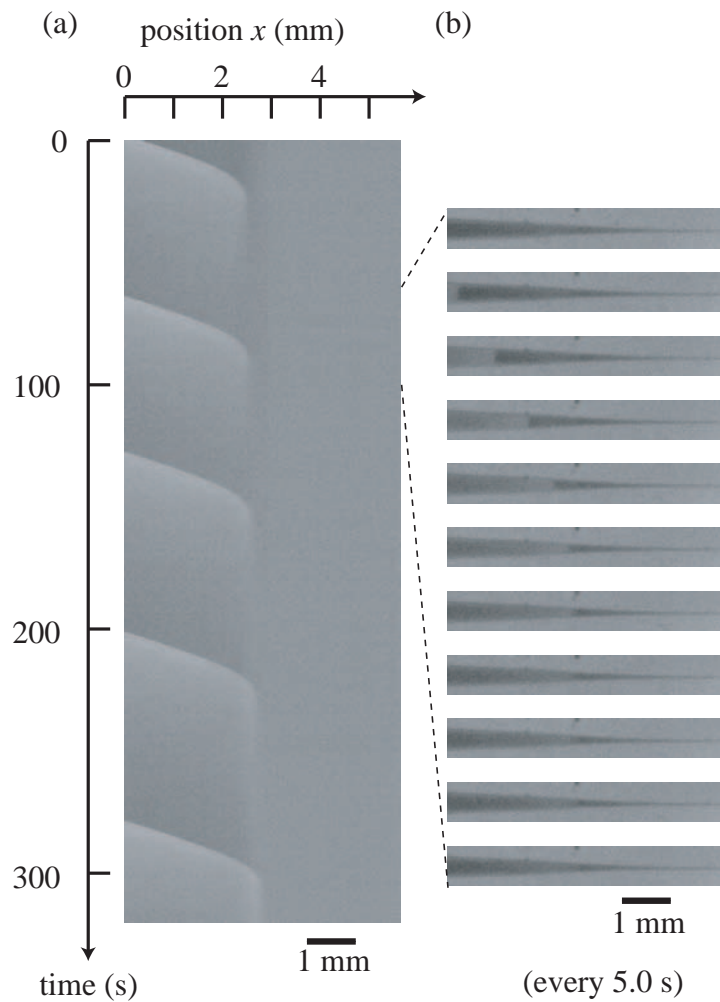
Figure 7.2: Experimental results on the propagation failure in a narrowing glass capillary. The chemical wave propagated from the left (wider end) to the right (narrower end). (a) Spatio-temporal plot of the chemical wave propagation. (b) Snapshots with an interval of 5.0 s. When the wave propagated to the narrower region, it slowed, stopped, and then disappeared. The darker and brighter areas correspond to the reduced and oxidized states, respectively [5].
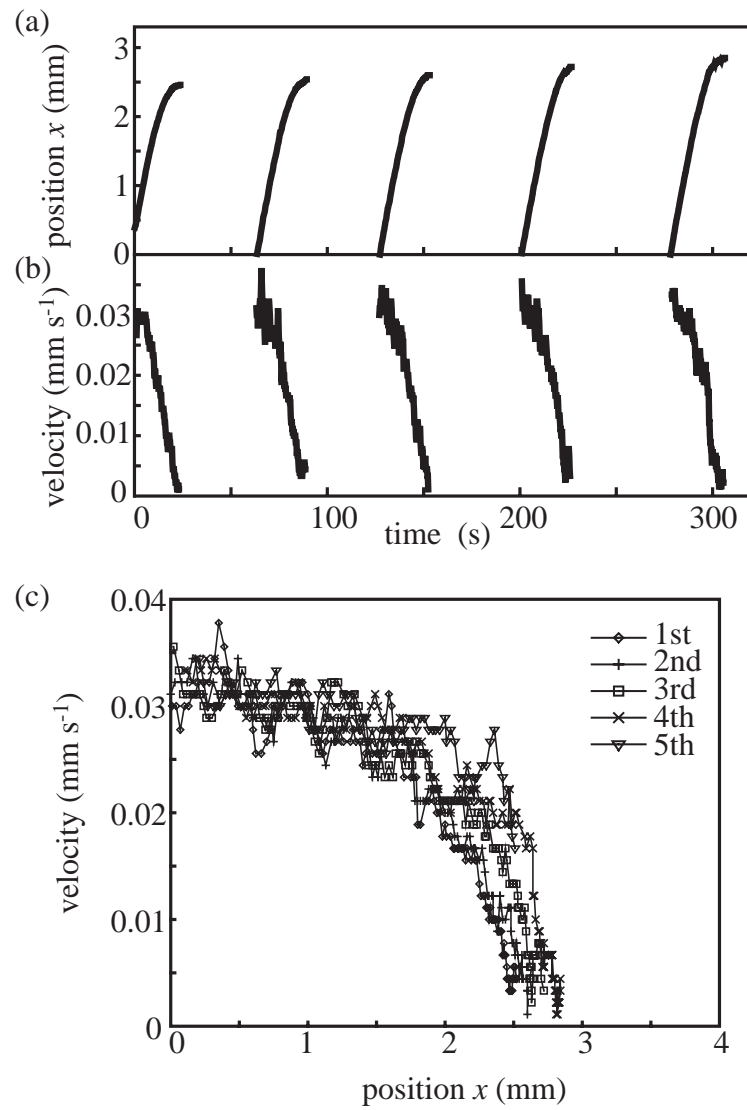
Figure 7.3: Features of the propagation failure of chemical waves in the experiments as shown in Fig. 7.2. (a) Temporal changes in the position and (b) velocity of chemical waves. (c) The relationship between position and velocity [5].
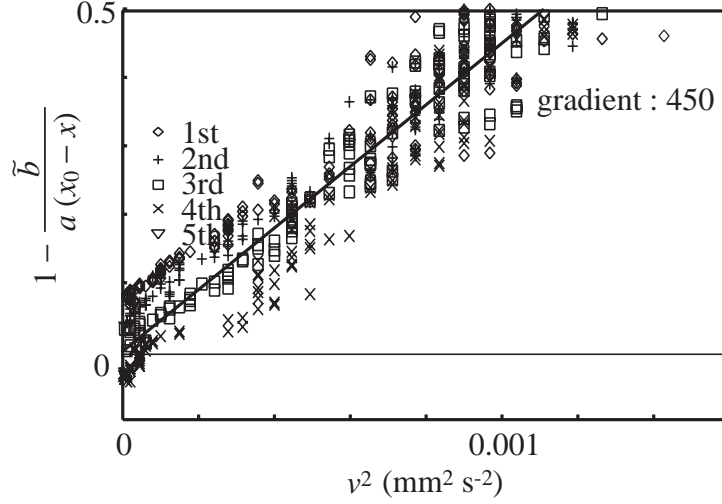
Figure 7.4: Plot of v^2 vs $1 - \tilde{b}/\{a(x_0 - x)\}$. Five chemical waves were measured and the different marks correspond to the different waves. By linear fitting, the gradient was calculated to be 450 mm^{-2} s^2 [5].

of the local velocity along the capillary is also given in a similar way, we simply adapt eq.(7.1) to interpret the experimental trends in a semi-quantitative manner.

The x axis is set in the direction of wave propagation. We describe the inner radius of the glass capillary, r, by assuming it as a part of a cone:

$$r = a(x_0 - x), \tag{7.2}$$

where a corresponds to the gradient of the inner radius of the glass capillary, and x_0 is the position that would be the top of the cone.

The concentration of hydrogen ion, H, can be decreased by the effect of the glass surface of the capillary. It is noted that H is the average concentration over the cross section, and that the effect on the hydrogen concentration by the glass surface is effective only near the surface. Amemiya et al. reported that the effective hydrogen ion concentration is not homogeneous in the porous glass system [89]. The sodium ions connected to the SiO_2^- groups could be, thus, replaced by hydrogen ions, which causes a decrease in the concentration of hydrogen ions near the glass surface. We assume that this effect is proportional to the surface-volume ratio:

$$H_{\text{eff}} = H\left(1 - b\frac{2\pi r}{\pi r^2}\right) \equiv H\left(1 - \frac{\tilde{b}}{r}\right), \tag{7.3}$$

where b is a positive constant that reflects the effect of the glass surface. Although, at present, it seems difficult to evaluate b from an experiment, as a
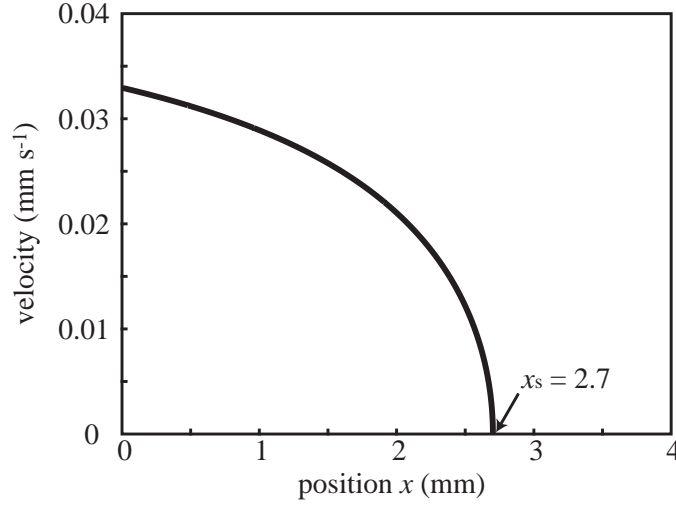
Figure 7.5: Relationship between position and velocity of a chemical wave based on the theoretical discussion by eq.(7.4). The parameters used here are determined from the experiments [5].

future subject, it may be of value to try to measure the change in the chemical environment near the surface. $\tilde{b}$ $(= 2b)$ is a positive constant introduced to simplify the equation.

From the above equations, we can derive the relationship between the position and velocity:

$$v = v_0 \left(1 - \frac{\tilde{b}}{a(x_0 - x)} \right)^{1/2}, \tag{7.4}$$

where v_0 is the velocity of the chemical wave without any effects from the glass surface. By letting $v = 0$ in eq.(7.4), we can determine the position, x_s, where the chemical wave stops:

$$x_s = x_0 - \frac{\tilde{b}}{a}. \tag{7.5}$$

Equation (7.4) can also be written as:

$$\left(\frac{v}{v_0} \right)^2 = 1 - \frac{\tilde{b}}{a(x_0 - x)}. \tag{7.6}$$

From the experimental results, the parameters were determined to be $x_s = 2.7 \pm 0.2$ mm, $x_0 = 5.5$ mm, and $a = 0.036$. Using these values, we plotted the relationship between v^2 and $1 - \tilde{b}/\{a(x_0 - x)\}$ in Fig. 7.4, where $\tilde{b}$ is calculated as $\tilde{b} = 0.20 \pm 0.01$ using eq. (7.5). The results show a linear relationship between these two values. By linear fitting, the gradient was calculated to be 450 ± 50 mm^{-2} s^2. This value corresponds to $1/v_0^2$, indicating that $v_0 = 0.047 \pm 0.003$ mm s^{-1}, which roughly corresponds to the wave velocity obtained through the

experiment using a wide capillary (0.06 ± 0.01 mm s^{-1}). Using this value, the plot between v and x is shown in Fig. 7.5. The relationship between v and x in the experiments, as shown in Fig. 7.3(c), was well reproduced in a quantitative manner. The velocity profile near the point where a chemical wave stops can be thus explained.

In the above discussion, the decrease in the effective concentration of the hydrogen ion, H_{eff}, near the glass surface seems to be induced by the adsorption by the SiO_2^- groups on the glass surface. With time, this substitution continues, and the effect of the glass surface on the concentration of the hydrogen ion decreases. This may be the cause of the slight shift in the position at which the chemical wave stops.

As we performed the experiments under the oxygen atmosphere, it is possible that the oxygen disturbs chemical-wave propagation. On this problem, we carried out the observation using a straight capillary with open ends, and confirmed that absorption of the oxygen from an open end has negligible effect on the manner of wave propagation. Therefore, it is most probable to expect that the significant factor is the absorption of the hydrogen ion to the inner wall of the glass capillary.

Chapter 8

Alternative stopping of a chemical wave in a photosensitive BZ reaction field

In Chapter 7, the chemical waves of BZ reaction in a narrowing glass capillary was investigated, and it is suggested that the effects of the glass surface is important. In this chapter, therefore, the narrowing reaction field is achieved using light illumination in photosensitive BZ reaction in order to avoid the effects of the glass. Then, it is observed that the chemical wave disappears alternatively at a certain light intensity.

8.1 Introduction

In the previous chapter, the natures of the chemical wave in the narrowing glass capillary were investigated. When a chemical wave goes to the narrower area, it propagates more and more slowly, and finally it stops and disappears. The mechanism of the slowing and stopping of the chemical wave can be explained as the effects of the glass surface, however, the physical chemistry near the glass surface is so difficult that the characteristics of the reaction diffusion system are hidden.

In this chapter, we made the narrowing reaction field using photosensitive BZ reaction. As written in Chapter 2, using Ru-catalyst, the BZ reaction has photosensitivity [42–44]. The mechanism of photosensitivity is considered as follows: Ruthenium catalyst absorbs light and is excited. When the excited catalyst is relaxed, it produces the bromide ion, which is the inhibitor of the BZ reaction. Therefore, in the region where light is illuminated, the inhibitor of BZ reaction increases.

Using a slide projector and a filter with a certain shape, we can achieve the reaction field with an arbitrary shape. In this chapter, chemical wave propaga-
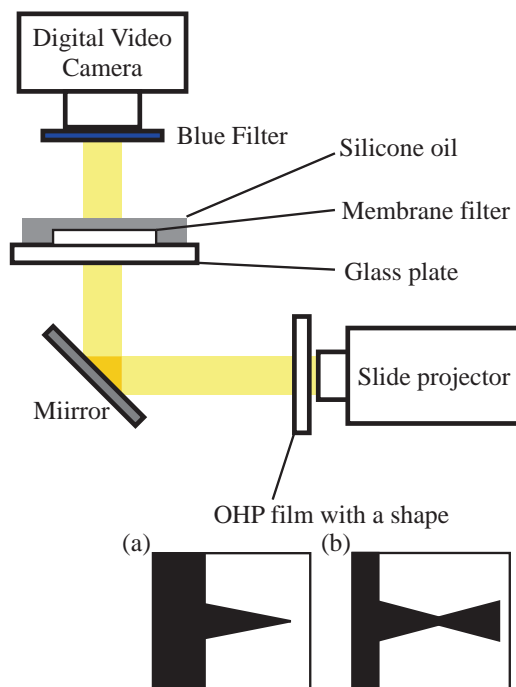
Figure 8.1: Schematic representation of experimental setup.

tion on the V- and X-shaped reaction fields as shown in Fig. 8.1 are investigated. On such reaction fields, the interesting phenomena on chemical wave propagation can be observed by changing the brightness of light irradiation. At a certain brightness, the positions at which chemical waves stop propagation change every two waves. In this chapter, the results of experiments and simple discussion are presented.

8.2   Experiments

All chemicals were analytical-grade reagents and used without further purification. The water was purified with a Millipore-Q system. The BZ medium contained 0.45 M sodium bromate ($NaBrO_3$), 0.30 M sulfuric acid (H_2SO_4), 0.20 M malonic acid ($CH_2(COOH)_2$), 0.05 M sodium bromide ($NaBr$), and 1.7 mM ruthenium bipyridyl chloride ($Ru(bpy)_3Cl_2$) (excitable condition). We mixed the chemical compounds except the ruthenium catalyst, and then the ruthenium catalyst solution was added to the solution waiting for around 4 minutes. The solution was heated till the first chemical wave was observed. Cellulose-nitrate membrane filters (Advantec, A100A025A with a pore size of 1 μm) were soaked in the BZ solution. The soaked membrane was gently wiped with a piece of filter paper to remove excess solution and placed on a piece of slide glass. The surface of the membrane filter was completely covered with around 1 ml of silicone oil to prevent it from drying and to protect it from the influence of
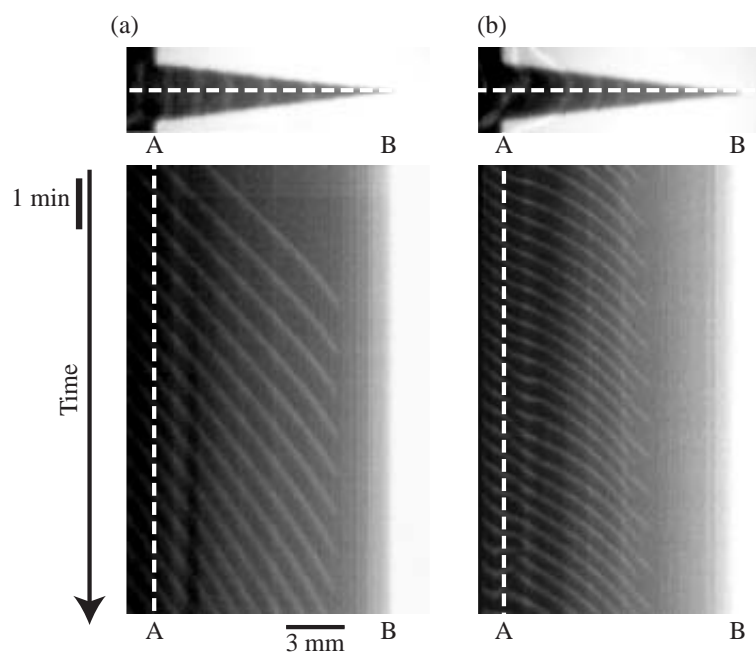
Figure 8.2: Experimental results on the reaction field with the triangular shape as in Fig. 8.1(a). Spatio-temporal plots achieved by aligning the images on the white broken line on the upper picture with time are shown.

oxygen. The experiments were carried out at room temperature. Using a slide projector and the OHP films with a certain shape printed, we could obtain the clear image on the membrane filter. Chemical waves were prevented from propagating in the brighter area, and they can propagate only in the darker area. We made the series of the experiments by changing the light intensity in the brighter region. The features of chemical wave propagation were recorded from above through a blue filter (Asahi Techno Glass, V-42) using a digital video camera. The schematic representation of the experimental setup is shown in Fig. 8.1.

8.3   Results

When the shape of the reaction field was triangular as shown in Fig. 8.1(a), the results of the chemical wave propagation are shown in Fig. 8.2. The chemical wave propagating from the broader region disappeared as they came to the narrower region. When the light intensity in the brighter area was smaller, the chemical waves disappeared at the same point as shown in Fig. 8.2(a). When it was larger, on the other hand, the points at which chemical waves disappeared changed every two wave as in Fig. 8.2(b). It was noted that the disappearing points sometimes changed every one in three or in more complicated way; however these phenomena were ambiguous and could not be observed stably.
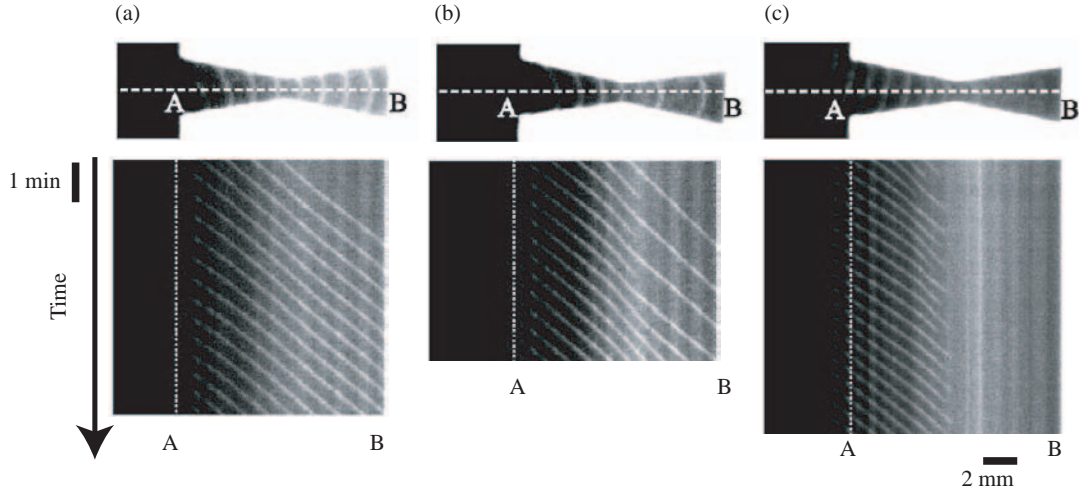
Figure 8.3: Experimental results on the reaction field with the combination of two triangles as in Fig. 8.1(b). Spatio-temporal plots achieved by aligning the images on the white broken line on the upper picture with time are shown.

When the shape of the reaction field was the combination of two triangles as shown in Fig. 8.1(b), the results of the chemical wave propagation are shown in Fig. 8.3. When the light intensity in the brighter area was smaller, all chemical waves propagated through the narrowest region as shown in Fig. 8.3(a). As the light intensity was slightly larger, every second wave could propagate through the narrowest region as in Fig. 8.3(b). When it was even larger, all chemical waves disappeared and failed propagation through the narrowest region as in Fig. 8.3(c).

8.4   Discussion

The Oregonator model is modified for photosensitive BZ reaction [90–92]:

$$\frac{\partial U}{\partial t} = \frac{1}{\epsilon}\left\{U(1-U) - (fV + A)\frac{U-q}{U+q}\right\} + D_U\nabla^2 U, \tag{8.1}$$

$$\frac{\partial V}{\partial t} = U - v + D_V\nabla^2 V, \tag{8.2}$$

where U and V are the dimensionless variable that correspond to the concentrations of the activator (HBrO$_2$) and the oxidized catalyst ([Ru(bpy)$_3$]$^{3+}$), respectively. f, ϵ and q are the positive parameters that determine the nature of the BZ reaction, D_U and D_V are the diffusion constants for the activator and the oxidized catalyst, and A is the variable that is proportional to the light intensity.

For simplicity, in this chapter, we adopt a one-dimensional model. In the experiments, the light intensity outside the reaction field was changed. It is
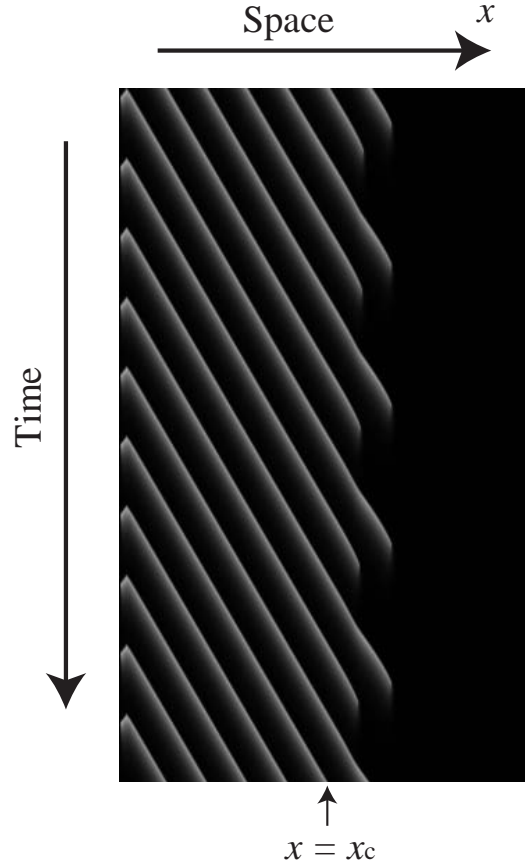
Figure 8.4: Numerical results based on eqs. (8.3) to (8.5). The spatio temporal plots are shown. The parameters are $f = 3$, $\epsilon = 0.04$, $q = 0.0008$, $A = 100$, $a = 8 \times 10^{-9}$, and $D_U = D_V = 1$.

assumed that when the reaction field becomes thin, the diffusion from/to the illuminated region becomes large. The activator diffuses from the reaction field to the illuminated region, and the inhibitor (bromide ion) diffuses from the illuminated area to the reaction field. This transfer can be described as follows:

$$\frac{\partial U}{\partial t} = \frac{1}{\epsilon}\left\{ U(1-U) - fV\frac{U-q}{U+q} + F(U,x)\right\} + D_U\nabla^2 U, \qquad (8.3)$$

$$\frac{\partial V}{\partial t} = U - v + D_V\nabla^2 V, \qquad (8.4)$$

$$F(U,x) = \begin{cases} a(x-x_c)^2\left(-A\frac{U-q}{U+q} - U\right), & (x \geq x_c) \\ 0, & (x < x_c) \end{cases} \qquad (8.5)$$

where the $a(x-x_c)^2$ is the factor that correspond to the amount of the transfer between the reaction field and illuminated region. A is the variable which is proportional to the light intensity in the illuminated region. This function is

adopted in order to change the parameter smoothly. $\left(A\frac{U-q}{U+q} - U\right)$ corresponds to the diffusion of the activator, U, from the reaction field to the illuminated area and the effects of the illumination on the activator, $-A\frac{U-q}{U+q}$.

Based on the eqs. (8.3) to (8.5), numerical calculation was performed. The results of the calculation are shown in Fig. 8.4. The positions at which chemical waves stop are changed alternatively. It is said that this simple model can represent some essences of the experimental results.

Chapter 9

Synchronization of photosensitive chemical waves coupled in two circular excitable fields

In this chapter, the geometry of chemical wave propagating on a circular ring is presented. The two chemical waves on the two contacted circular rings are also discussed from the viewpoint of synchronization [6].

9.1 Introduction

In Chapters 7 and 8, the anomalous chemical wave propagation on the reaction field with a small scale is reported. In this chapter, on the other hand, the chemical wave propagation on the excitable field with a shape of circular rings is investigated.

Experimental and theoretical studies on wave propagation on an excitable media may help us to not only understand signal processing in biological systems [93] such as nerve impulses [26] but also to create novel methods for artificial processing such as image processing [43, 44, 94, 95] and logic operations [85, 92, 96–99]. The Belousov-Zhabotinsky (BZ) reaction has been widely investigated as an excitable or oscillatory chemical system. The BZ reaction on a membrane, e.g., filter paper, [100, 101] nafion membrane, [102–104], gel [34, 69] or glass filter, [105] has been widely studied because the spatio-temporal pattern of wave propagation can be regulated by the geometry of the excitable field, which is easily prepared by cutting or printing. In such systems, however, it can be technically difficult to cut a membrane filter with a completely similar shape and to regulate the number of chemical waves and their intervals.

A photosensitive experimental set-up of the BZ reaction makes it easy to cre-

ate excitable fields of various geometries, which are drawn by computer software and then projected on a membrane filter soaked with BZ solution using a liquid-crystal projector. In this case, light illumination produces bromide ion which inhibits the oscillatory reaction, i.e., the degree of excitability can be adjusted by changing the intensity of illumination. Therefore, the number of chemical waves and their intervals can be spatio-temporally regulated by illumination.

In this chapter, the propagation of chemical waves in the photosensitive BZ reaction on an excitable field (a circular ring or a figure "8" composed of two equivalent circular rings) illuminated with a liquid-crystal projector was investigated. The nature of wave propagation depending on the ratio of the inner and outer radii of the circular rings was well fitted as the involute of a circle [106–109]. When the two equivalent circular rings slightly in contact with one another, two chemical waves collided at a location apart from the intersection. When two circular rings completely overlapped at the intersection, the location of wave collision alternated with time. The essential feature of wave propagation was qualitatively reproduced by a numerical calculation based on the reaction-diffusion equations using the modified Oregonator.

9.2   Experiments

Ru(bpy)$_3$Cl$_2$ was used as a catalyst for the photosensitive BZ reaction. The BZ solution consisted of [NaBrO$_3$] = 0.45 M, [H$_2$SO$_4$] = 0.3 M, [CH$_2$(COOH)$_2$] = 0.2 M, [KBr] = 0.05 M, and [Ru(bpy)$_3$Cl$_2$] = 1.7 mM. Cellulose-nitrate membrane filters (Advantec, A100A025A) with a pore size of 1 μm were soaked in BZ solution (5 ml) for about 1 min. The soaked membrane was gently wiped with filter paper to remove excess solution and placed on a petri dish (diameter: 100 mm). The surface of the membrane filter was completely covered with 1 ml silicone oil (Wako, WF-30) to prevent it from drying and to protect it from the influence of oxygen. The experiments were carried out in an air-conditioned room at 298 K, at which the reaction medium showed no spontaneous excitation and no change in behavior for approximately 30 min.

The medium was illuminated from below as schematically shown in Fig. 9.1. The high-pressure mercury bulb of a liquid-crystal projector (MITSUBISHI, LVP-XL8) was used as a light source and the spatial intensity distribution was controlled with a personal computer. A black and white picture on the liquid-crystal projector served as an illumination mask to create the appropriate boundary, and the light intensities were 4.0×10^2 lx and 1.7×10^4 lx for black and white regions, respectively. The experiments were monitored from above with a digital video camera (SONY, DCR-VX700) and recorded on videotape. A blue optical filter (Asahi Techno Glass, V-42) with a maximum transparency at 410 nm was used to enhance the image of the chemical waves. The light intensity at the illuminated part was measured with a light intensity meter (ASONE, LX-100).
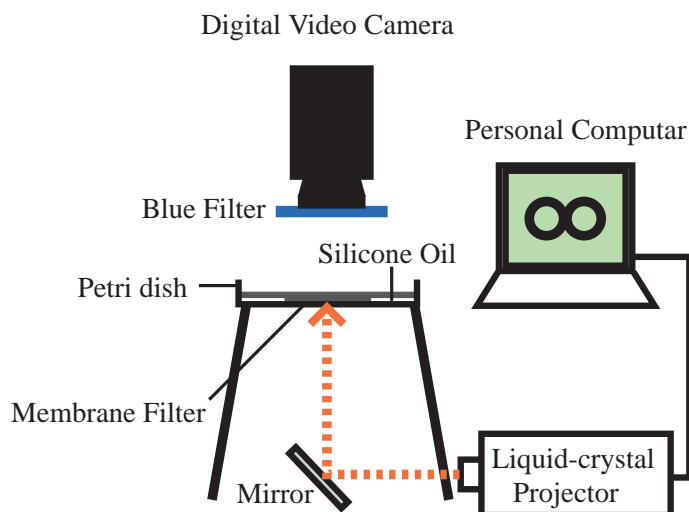
Figure 9.1: Schematic representation of experimental setup [6].

9.3   Results

9.3.1   Propagation of a single wave on a circular ring

First, we examined the radius-dependent propagation of a single wave on a reaction field in the shape of a circular ring. In this experiment, two chemical waves initially propagated in opposite directions. By the local illumination around one wave within 1 s, the illuminated wave was disappeared, but another one continued to propagate. Therefore the uni-directional chemical wave on the ring was achieved. Figure 9.2(a) shows the velocity of wave propagation on a circular ring depending on r_{out}/r_{in} (r_{in}: inner radius, r_{out}: outer radius of the circular route). In this experiment, r_{in} was varied under constant r_{out} ($= 6$ mm). The velocity of the chemical wave at the inner boundary of the circle (v_{in}) was almost independent of r_{in}. On the other hand, that at the outer boundary (v_{out}) was linearly increased with $1/r_{in}$, which indicates that the angular velocity of the chemical wave (ω) was determined by the wave propagation near the inner radius, i.e. $\omega = (v_{in}/2\pi)/r_{in}$ and $v_{out} = 2\pi r_{out}\omega$. The phase difference ($\Delta\theta$), which is schematically defined in Fig. 9.2, increased with r_{out}/r_{in}, as shown in Fig. 9.2(b), i.e., the deformation of the chemical wave increased with the width of the circular ring.

9.3.2   Collision of two chemical waves on two equivalent circular rings

Next, we examined the interaction between two chemical waves on a reaction field composed of two equivalent circular rings at $r_{in} = 2.1$ mm and $r_{out}/r_{in} = 2.0$. In this experiment, one chemical wave was initially generated in each ring in the
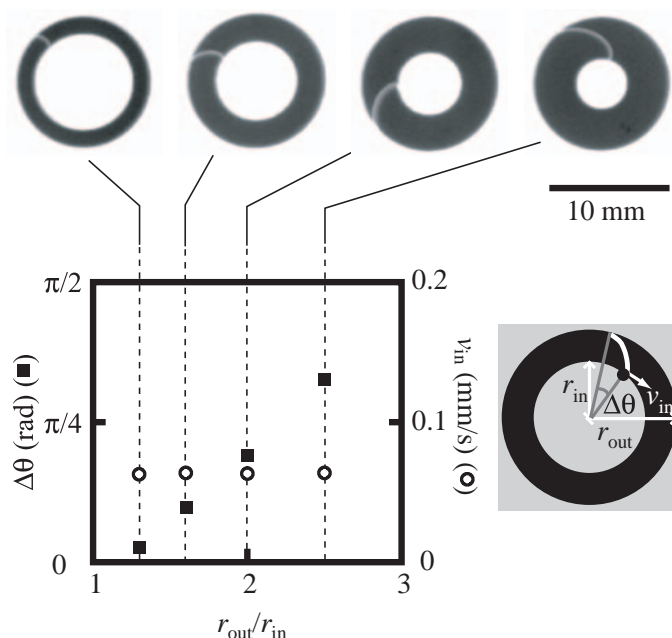
Figure 9.2: Wave propagation on a circular ring depending on r_{out}/r_{in} for v_{in} (empty circle) and $\Delta\theta$ (filled square). Corresponding snapshots are indicated in the upper part. $\Delta\theta$, r_{out}, r_{in}, and v_{in} are schematically defined at the right side of the figure [6].

same direction (clockwise), and the chemical wave in the right ring reached the intersection before that in the left ring.

When the distance between the centers of the two rings was nearly equal to $2r_{out}$, i.e., the two rings were just slightly in contact with one another, the location of the collision of the two waves was determined to be in the left ring near the intersection, as shown in Figs. 9.3 (a-1) and (b-1). Here, θ_L and θ_R are the angles corresponding to the positions of pulses on the left and right inner rings, and they are plotted at the moment two pulses collide in Fig. 9.3 (b). The location of the collision converged to 1.93π rad with time, and this convergent value did not change even when the difference in the initial phases was larger than 1.93π rad (data not shown) [110].

When the distance between the centers of the two rings was equal to $r_{in}+r_{out}$, i.e., the two rings completely overlapped one another, the location of the collision of the two waves changed alternatively, as shown in Figs. 9.3 (a-2) and (b-2), i.e., the chemical wave from the right ring reached the intersection ahead of that from the left ring, as seen in snapshots 1 and 3, or vice versa, as seen in snapshots 2 and 4.

(a-1)

(a-2)

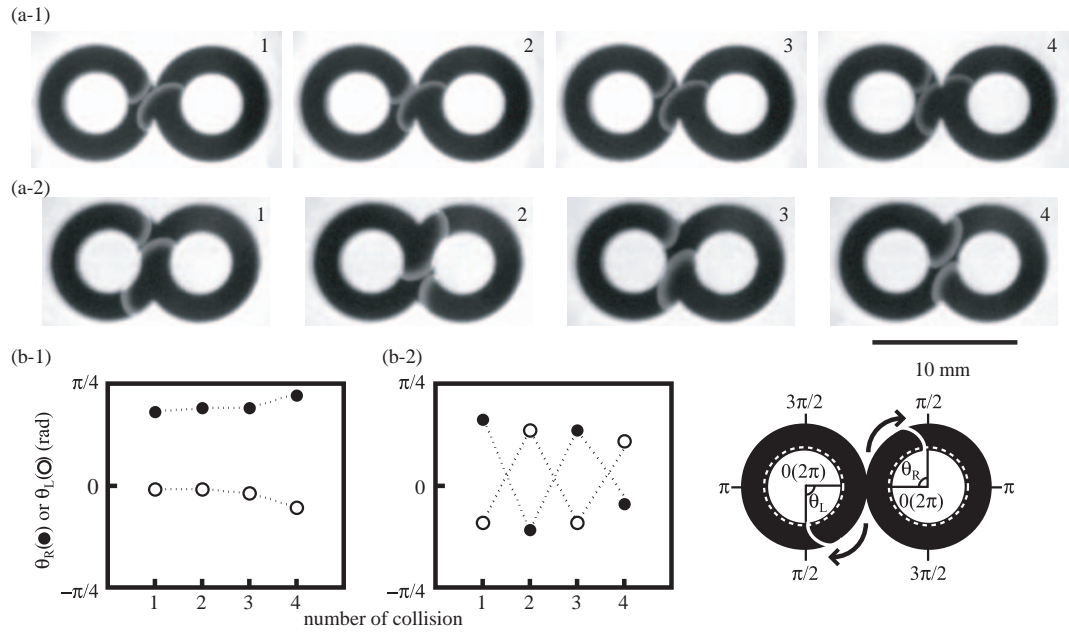(b-1)   (b-2)

Figure 9.3: Interactive wave propagation between two chemical waves in two equivalent circular rings that (1) were slightly in contact and (2) completely overlapped one another. (a) Top view of the snapshots of the wave propagation with the time intervals of (1) 300 sec and (2) 250 sec. (b) θ_R (filled circle) and θ_L (empty circle) when the two waves collided for (b-1) slightly connecting rings and (b-2) completely overlapping rings. θ_L and θ_R were schematically defined on the right side. The numbers of collision (1, 2, 3, 4) correspond to those in (a) [6].

9.4   Discussion

9.4.1   The nature of chemical wave propagation in a single circular ring.

Based on the experimental results and those in the related papers [106–109], we now discuss the characteristics of the BZ wave propagation in a reaction field designed by the light illumination. First, we analyze the shape of wave propagation depending on r_{out}/r_{in} of the circular ring. If we suppose that the wave propagates on the reaction field without any effects from the boundary, and that the wave cannot move into the brighter area, the distance from a point on the inner circle (point α) to another point (point β), which is one of the locations at which the chemical wave propagates along the inner circle, is the same as that to the intersection (point γ) between the chemical wave and the tangent line at the noted point (point α), as schematically indicated in Fig. 9.4 (a), since the chemical wave propagates in a direction perpendicular to the wave
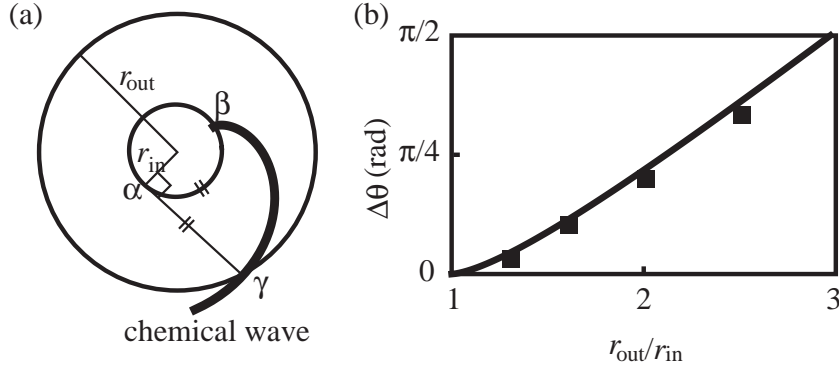
Figure 9.4: (a) Schematic representation on the chemical wave with the shape of the "involute" of a circle. (b)Comparison between the experimental results and the analytical prediction. The solid squares are the experimental results shown in Fig. 9.3, and the solid curve is the analytical prediction based on eq. (9.6) [6].

front with a uniform velocity. Therefore, the shape of the chemical wave may be regarded as the involute of a circle [106–109].

From the geometrical perspective, when the location of the chemical wave on the inner circle of the ring (point β) is expressed as $x = r_{\text{in}} \cos \theta_{\text{in}}$ and $y = r_{\text{in}} \sin \theta_{\text{in}}$, that on the chemical wave is expressed using parameter θ,

$$\begin{pmatrix} x \\ y \end{pmatrix} = r_{\text{in}} \begin{pmatrix} \cos \theta \\ \sin \theta \end{pmatrix} + r_{\text{in}} (\theta_{\text{in}} - \theta) \begin{pmatrix} -\sin \theta \\ \cos \theta \end{pmatrix}, \tag{9.1}$$

where θ is the phase of the point α. We calculate the location of the intersection between the chemical wave and the outer circle with a radius of r_{out}, (point γ). Here, the phase of the intersection is set as θ_{out}. From

$$r_{\text{out}}^2 = r_{\text{in}}^2 \left(1 + (\theta_{\text{in}} - \theta)^2 \right), \tag{9.2}$$

and

$$\tan \theta_{\text{out}} = \frac{r_{\text{in}} \sin \theta + r_{\text{in}} (\theta_{\text{in}} - \theta) \cos \theta}{r_{\text{in}} \cos \theta - r_{\text{in}} (\theta_{\text{in}} - \theta) \sin \theta} = \frac{\tan \theta + (\theta_{\text{in}} - \theta)}{1 - (\theta_{\text{in}} - \theta) \tan \theta}, \tag{9.3}$$

we can get

$$\tan \theta_{\text{out}} = \tan (\theta_{\text{in}} + \alpha), \tag{9.4}$$

where $\tan \alpha = \sqrt{r_{\text{out}}^2 - r_{\text{in}}^2}/r_{\text{in}} = \theta_{\text{in}} - \theta$. From eq. (9.4),

$$\theta_{\text{out}} = \theta_{\text{in}} + \alpha = \theta_{\text{in}} - \sqrt{r_{\text{out}}^2 - r_{\text{in}}^2}/r_{\text{in}} + \arctan \left(\sqrt{r_{\text{out}}^2 - r_{\text{in}}^2}/r_{\text{in}} \right). \tag{9.5}$$

Therefore, we can derive

$$\Delta \theta = \theta_{\text{in}} - \theta_{\text{out}} = \sqrt{(r_{\text{out}}/r_{\text{in}})^2 - 1} - \arctan \left(\sqrt{(r_{\text{out}}/r_{\text{in}})^2 - 1} \right). \tag{9.6}$$

Figure 9.4 (b) shows the theoretical results obtained based on eq.(9.6). These theoretical results suggest that the experimental results regarding the nature of the chemical wave propagation shown in Fig. 9.4 can be quantitatively fitted by a theoretical consideration based on the geometrical discussion. In the previous study, Müller et al. and Noszticzius et al. reported that the shape of the chemical wave is the involute of a circle and that it can be regarded as an Archimedes spiral far enough from the tip of the wave [106–109]. In this study, the chemical wave is well fit to the involute of a circle but not a spiral, since the core of the spiral is much larger than that of the spiral pattern formed spontaneously.

9.4.2   The nature of chemical wave propagation on two equivalent circular rings.

Following the above discussion, we calculated the nature of chemical wave propagation in a reaction field composed of two equivalent circular rings. We derived a characteristic phase differences $\Delta\theta_0$ that depended on the shape of the reaction field. First, it should be noted that there are two types of interaction between the chemical waves on the two rings: in one type, the chemical wave on one ring (ring A) propagates and touches the inner radius of the other ring (ring B), and in the other type, the chemical wave does not touch it. In the former case, the phase of the chemical wave on the ring A affects the phase of the chemical wave on ring B. Therefore, the phase difference between the chemical waves on the two rings is determined only by the shape of the reaction field. This difference in phase on the two circular rings is set as $\Delta\theta_0$. In the latter case, in contrast, the chemical wave on the ring A does not affect the chemical wave propagation on ring B. These two cases are selected by the initial phase difference between θ_L and θ_R when they reach a stationary propagation without collision. This characteristic phase difference $\Delta\theta_0$ is analytically derived as follows:

We consider chemical wave propagation on a field composed of two circular rings with overlap d, as shown in Fig. 9.5(a). Here, we derive the characteristic phase difference $\Delta\theta_0$ between the phase of the chemical wave in one ring (ring A) and that of the chemical wave on the other ring (ring B) after the chemical wave on the ring A affects chemical wave propagation on ring B. The time required for a chemical wave to reach a certain point can be calculated from the shortest path. Therefore, we have to consider the two cases as shown in Fig. 9.5.

In the case in Fig. 9.5 (b-1), i.e.,

$$\sqrt{r_{\text{out}}^2 - (r_{\text{out}} - d/2)^2} > r_{\text{in}}, \tag{9.7}$$

the shortest path from one ring to the other ring is a straight line, and the length, L, is

$$L = 2r_{\text{out}} - d. \tag{9.8}$$

If we suppose that the chemical wave on the ring A affects the chemical wave propagation on ring B, the phases of the chemical waves on rings A and B, θ_A
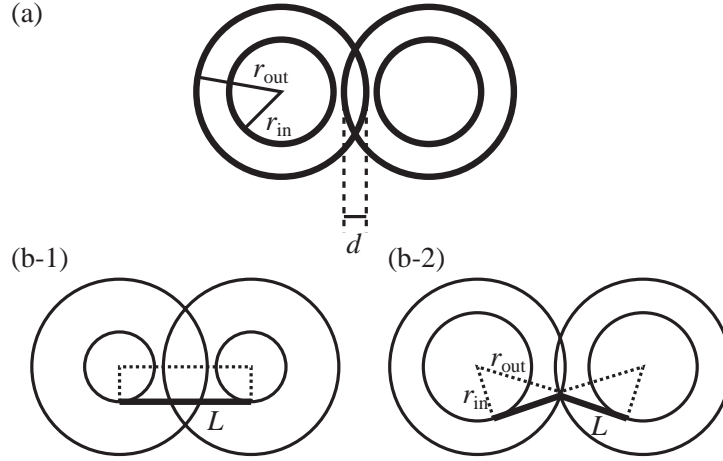
Figure 9.5: Schematic representation of (a) the shape of the reaction field and (b) the shortest path when the chemical wave in one ring propagates to the other ring. (b-1) When the shortest path is a straight line. (b-2) When the shortest path is a V-shaped line [6].

and θ_B, can be written as

$$\theta_A = -\frac{\pi}{2} + \frac{v}{r_{in}}t, \tag{9.9}$$

and

$$\theta_B = \frac{\pi}{2} + \frac{v}{r_{in}}\left(t - \frac{L}{v}\right), \tag{9.10}$$

where t is time. Therefore, the characteristic phase difference $\Delta\theta_0$ is derived as

$$\Delta\theta_0 = \theta_B - \theta_A = \pi - \frac{2r_{out} - d}{r_{in}}. \tag{9.11}$$

On the other hand, in the case of Fig. 9.5 (b-2), i.e.,

$$\sqrt{r_{out}^2 - (r_{out} - d/2)^2} < r_{in}, \tag{9.12}$$

the shortest path is a V-shaped line, and L is derived as

$$L = 2\sqrt{r_{out}^2 - r_{in}^2}. \tag{9.13}$$

If we suppose that the chemical wave on ring A affects the chemical wave propagation on ring B, θ_A and θ_B can be written as

$$\theta_A = -\Theta_0 + \frac{v}{r_{in}}t, \tag{9.14}$$

and

$$\theta_B = \Theta_0 + \frac{v}{r_{in}}\left(t - \frac{L}{v}\right), \tag{9.15}$$
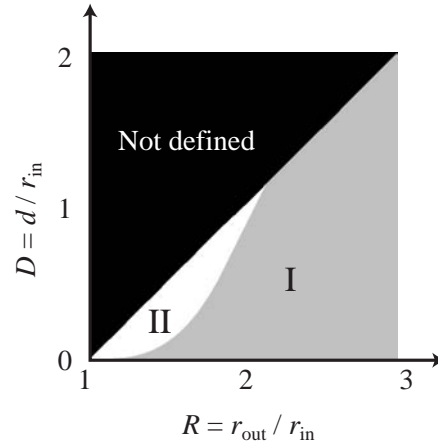
Figure 9.6: Phase map of the synchronization of chemical wave propagation in a reaction field composed of two equivalent circular rings depending on $R = r_{\text{out}}/r_{\text{in}}$ and $D = d/r_{\text{in}}$. Region I corresponds to collision at one point, and region II corresponds to alternative collisions [6].

where
$$\Theta_0 = \arccos\left(\frac{r_{\text{in}}}{r_{\text{out}}}\right) + \arccos\left(\frac{r_{\text{out}} - d/2}{r_{\text{out}}}\right). \tag{9.16}$$

Therefore, the characteristic phase difference $\Delta\theta_0$ is derived as

$$\Delta\theta_0 = \theta_{\text{B}} - \theta_{\text{A}} = 2\Theta_0 - \frac{2\sqrt{r_{\text{out}}^2 - r_{\text{in}}^2}}{r_{\text{in}}}. \tag{9.17}$$

In summary, the characteristic phase difference $\Delta\theta_0$ is written as

$$\Delta\theta_0 = \theta_{\text{B}} - \theta_{\text{A}} = \begin{cases} \pi - 2R + D & (R > D/4 + 1/D) \\ 2\Theta_0 - 2\sqrt{R^2 - 1} & (R < D/4 + 1/D) \end{cases}, \tag{9.18}$$

and

$$\Theta_0 = \arccos\left(\frac{1}{R}\right) + \arccos\left(1 - \frac{D}{2R}\right). \tag{9.19}$$

These equations are written in the nondimensional form using $R = r_{\text{out}}/r_{\text{in}}$ and $D = d/r_{\text{in}}$. The phase map shown in Fig. 9.6 is drawn according to the sign of $\Delta\theta_0$.

According to the above discussion, when the initial phase difference is smaller than $|\Delta\theta_0|$, the phase difference is maintained. Though we do not show the experimental data corresponding to this case, but this features are confirmed in the experiments [110]. On the other hand, when the initial phase difference is larger than $|\Delta\theta_0|$, the chemical waves on the two rings affect each other: If $\Delta\theta_0 < 0$ (Region I), the phase difference is fixed as $|\Delta\theta_0|$. If $\Delta\theta_0 > 0$ (Region II), the phase difference changes alternatively. Thus, the location of the collision of the
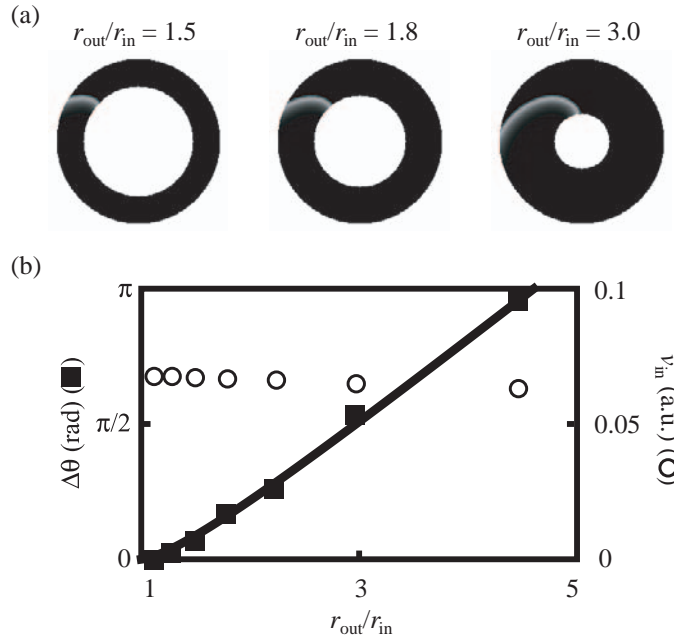
Figure 9.7: Results of the numerical calculation for a reaction field in the shape of a circular ring based on the modified Oregonator model shown in eqs. (9.20) and (9.21). (a) Snapshots for the various values of r_{out}/r_{in}. (b) Wave velocity along the inner boundary v_{in} (empty circle) and the phase difference between the locations of the chemical wave along the inner and outer boundaries $\Delta\theta$ (filled square) depending on r_{out}/r_{in}. The curve derived from the analytical discussion is also described as a solid curve. The parameters used in the calculations are $f = 1$, $\epsilon = 0.05$, $q = 0.00015$, and $D_U = D_V = 1$. The chemical wave is initiated by setting $U = 0.5$ at a certain point. Some time later, the two chemical waves propagate in opposite directions. By increasing the variable for light intensity, A, in a certain area for some length of time, we can make one wave disappear, and a unidirectional chemical wave is achieved [6].

two waves changes alternatively. Figure 9.6 shows a phase map that depends on R (the ratio between the inner and outer radii, r_{out}/r_{in}) and D (the ratio between the overlap and the inner radius, d/r_{in}). The characteristics of the chemical wave propagation shown in 1 and 2 in Fig. 9.3 in the experiments correspond to regions I and II, respectively. The properties of chemical wave propagation on two equivalent circular rings can be understood analytically within this framework.

9.4.3   Numerical calculation using the modified Oregonator model

We performed numerical calculations based on the modified Oregonator [90–92]:

$$\frac{\partial U}{\partial t} = \frac{1}{\epsilon}\left\{ U(1-U) - (fV+A)\frac{U-q}{U+q}\right\} + D_U \nabla^2 U, \qquad (9.20)$$

$$\frac{\partial V}{\partial t} = U - v + D_V \nabla^2 V, \qquad (9.21)$$

where U and V are the dimensionless variable that correspond to the concentrations of the activator ($HBrO_2$) and the oxidized catalyst ($[Ru(bpy)_3]^{3+}$), respectively. f, ϵ and q are the positive parameters that determine the nature of the BZ reaction, D_U and D_V are the diffusion constants for the activator and the oxidized catalyst, and A is the variable that is proportional to the light intensity. We set $A = 0.03$ in the brighter area and 0.005 in the darker area, respectively.

The results of the numerical calculation for a reaction field in the shape of a circular ring are shown in Fig. 9.7. The relationship between $\Delta\theta$ and $r_{\mathrm{out}}/r_{\mathrm{in}}$ is described together with the analytical prediction by eq. (9.6). This dependency is well described by the analytical discussion, and the experimental, theoretical and numerical results are all consistent with one another.

Figure 9.8 shows the numerical results for a reaction field in the shape of a figure "8", which is composed of two equivalent circular rings. When the two circular rings slightly in contact with one another, the phase difference is fixed at a constant value, as shown in Figs. 9.8 (a-1) and (b-1). On the other hand, when they completely overlap, the phase difference changes alternatively; i.e., the location of the collision changes alternatively, as shown in Figs. 9.8 (a-2) and (b-2). These experimental and analytical results are well reproduced by the numerical calculations.
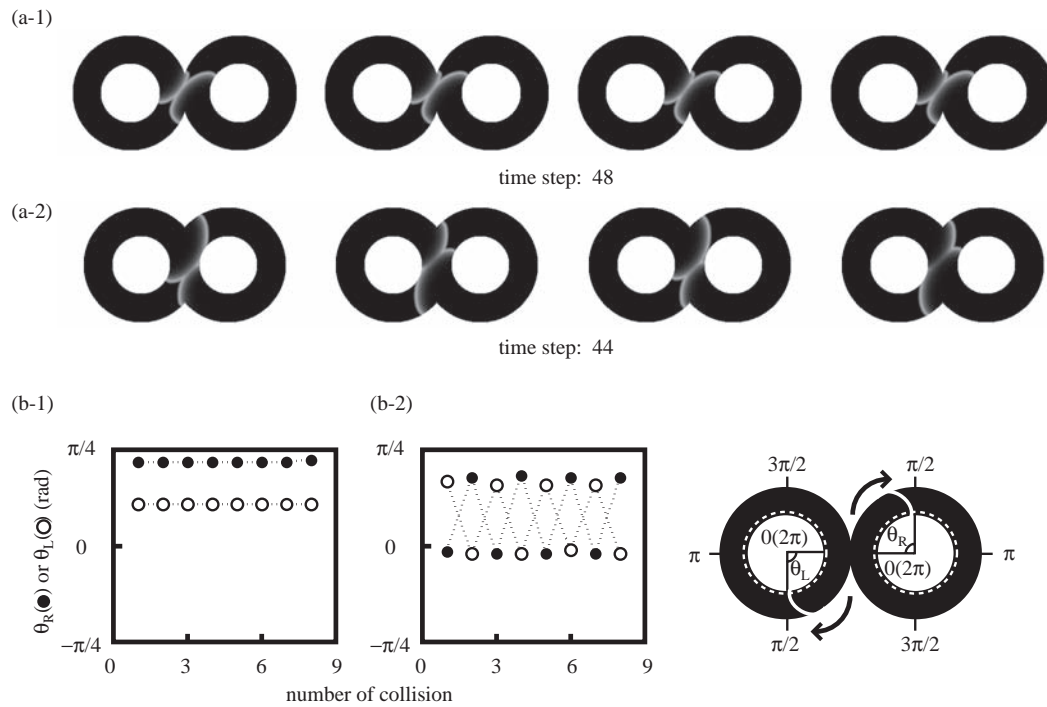
Figure 9.8: Results of a numerical calculation for a reaction field in the shape of a figure "8" composed of two equivalent circular rings based on the modified Oregonator model shown in eqs. (9.20) and (9.21). (a) Snapshots of a typical nature of wave propagation for (a-1) slightly connected rings and (a-2) completely overlapping rings. (b) Phases of the locations of collision versus the number of collision for (b-1) slightly connecting rings and (b-2) completely overlapping rings. The parameters and the initial conditions are the same as those in Fig. 9.7. The shape of the field is $r_{\mathrm{out}}/r_{\mathrm{in}} = 2$ for both (1) and (2), $d/r_{\mathrm{in}} = 2/9$ for (1), and $d/r_{\mathrm{in}} = 1$ for (2) [6].

Part IV

General Conclusion

Chapter 10

Conclusion

10.1 Conclusion

In this thesis, the experimental and theoretical results on the reaction diffusion systems coupled with convection and geometrical effects are demonstrated.

As for the reaction-diffusion systems coupled with convection, the spontaneous motion can be exhibited induced by the spatio-temporal pattern formation in reaction-diffusion systems. At the same time, the convective flow of the field can cause the spatio-pattern formation:

In the BZ reaction system, convective flow in the bulk phase can be observed induced by the repetitive change in interfacial tension of BZ medium (Chapter 3). This convection can cause the spontaneous motion of a small droplet of BZ reaction medium (Chapter 4). In the water-camphor system, convective flow coupled with the surface diffusion of the camphor layer can be observed. This convective flow can affect the spontaneous motion of a camphor disk (Chapter 5). These two systems can be understood as a reaction-diffusion systems coupled with convection through interfacial tension. Some other systems, i.e.: the spontaneous motions of an alcohol droplet in the water-alcohol system, an oil droplet on the glass substrate in the surfactant solution, and a phenanthroline disk in the ferrous sulfate solution are also exhibited (Chapter 6).

As for the boundary effects in reaction-diffusion systems, the characteristics of the chemical wave changes when the system size is comparable to the chemical wave itself. In this part, the anomalous behavior of chemical waves are exemplified:

In Chapter 7, the slowing and stopping of the chemical wave in the narrowing glass capillary is exemplified in BZ reaction. The mechanism is theoretically analyzed related to the surface-volume ratio. The scaling analysis was performed, and the experimental results can be reproduced. In Chapter 8, the narrowing reaction field is achieved using light illumination in photosensitive BZ reaction. The alternative disappearing of the propagating chemical waves are observed. In Chapter 9, the geometry of chemical wave propagating on a circular ring is studied. The two chemical waves on two connected circular rings are also

discussed from the viewpoint of synchronization.

Considering the phenomena in the real world, especially in the living organisms, the rhythmicity, pattern formation, and directional motion should be coupled with each other. The system has a finite size and the boundary of the system should affect seriously. In order to discuss on the mechanism of the nonequilibrium systems, these convective effects and boundary effects cannot be avoided. The discussions in this thesis may help to understand the mechanism on how the convective flow and geometrical effects of the boundary affect the nonequilibrium systems.

10.2   Future problems

In proceeding the studies on the reaction diffusion systems coupled with convective flow or geometrical effects of the boundary, a lot of problems or difficulties have come out and some remained to be unsolved so far. The followings are some of the future problems:

In Part II, several numerical calculations based on the reaction-diffusion-advection equations coupled through the interfacial tension gradient were performed. The numerical results reproduce the experimental results to some extent, but some characteristics cannot be reproduced. For example, in the experiments of the convective flow induced by BZ reaction (Chapter 3), the strong convective flow can be observed before the wave front. On the other hand, in the numerical calculation, strong flow can be observed only near the wave front.

I guess that these differences are due to the nonequilibrium condition. The interfacial tension is defined in the equilibrium state, but in this case, the concentration of the surface-active compounds is not uniform, which means that the system is under nonequilibrium condition. Thus, the interfacial tension cannot be defined in the similar way to that in the equilibrium state. The interfacial tension under nonequilibrium condition should be studied more from both the microscopic and macroscopic points of view.

In Part III, some characteristic behaviors of the chemical wave propagation are presented in the reaction field with the size of 10 μm to 1 mm. In this scale, the singularity is due to the surface-volume ratio. In other words, the condition near the surface is different from that in the bulk phase, and the total behavior changes because the ratio of the region affected from the surface relatively increases.

In a much smaller system, another singularity may happen: the fluctuation of the concentration. In the reaction with an autocatalytic process, such as the BZ reaction, has a state with a little concentration of some chemical compounds. For example, in the BZ reaction, the concentration of the activator is very little during a certain span in the oscillation. The fluctuation of the number of molecules is supposed to be proportional to $N^{1/2}$, where N is the number of molecules. Thus, in a very small system, the fluctuation of the number of

molecule can appear as the fluctuation of the period of the chemical oscillation. This is an interesting problem from the viewpoints of not only physics but also life sciences, since the behavior of the molecules inside the cell should be affected by this fluctuation.

Acknowledgment

I appreciate the discussions with them so much. I cannot write down the name of every member, but I have spent a great time with the colleagues. Active discussions with them, talks on coffee or alcohol, and kind advices from them are the greatest help for me.

I am grateful to Ms. Yoshimi Mayama, Ms. Tomoko Kawakami, Ms. Mami Harada, Ms. Yuka Yamafuji, and Ms. Naoko Yamawaki for their kind support. They have given us the great environment to study in the laboratory.

At last, I am very grateful for all the kind supports from my friends, and my family.

References

[1] H. Kitahata, R. Aihara, N. Magome, and K. Yoshikawa, *J. Chem. Phys.*, **116**, 5666 (2002).

[2] H. Kitahata, *Prog. Theor. Phys. Suppl.*, in press.

[3] H. Kitahata, S. Hiromatsu, Y. Doi, S. Nakata, and M. R. Islam, *Phys. Chem. Chem. Phys.*, **6**, 2409 (2004).

[4] H. Kitahata and K. Yoshikawa, *Physica D*, **205**, 283 (2005).

[5] H. Kitahata, R. Aihara, Y. Mori, and K. Yoshikawa, *J. Phys. Chem. B*, **108**, 18956 (2004).

[6] H. Kitahata, A. Yamada, S. Nakata, and T. Ichino, *J. Phys. Chem. A*, **109**, 4973 (2005).

[7] H. Kitahata, N. Magome, and K. Yoshikawa, *Proc. Slow Dyn. Compl. Sys. (AIP Proc.)*, **708**, 430 (2004).

[8] S. Nakata, Y. Doi, and H. Kitahata, *J. Colloid. Interface. Sci.*, **279**, 503 (2004).

[9] S. Nakata, S. Hiromatsu, and H. Kitahata, *J. Phys. Chem. B*, **107**, 10557 (2003).

[10] K. Nagai, Y. Sumino, H. Kitahata, and K. Yoshikawa, *Phys. Rev. E*, **71**, 065301 (2005).

[11] Y. Sumino, H. Kitahata, K. Yoshikawa, M. Nagayama, S.-i. M. Nomura, N. Magome, and Y. Mori, *Phys. Rev. E*, **72**, 041603 (2005).

[12] H. Kitahata and K. Yoshikawa, *J. Phys.: Condens. Mat.*, **17**, S4239 (2005).

[13] E. Schrodinger, *What is Life?* (Cambridge University Press, Cambridge, 1944).

[14] G. Nicolis and I. Prigogine, *Self-organization in Nonequilibrium Systems* (Wiley & Sons, New York, 1977).

[15] Y. Kuramoto, *Chemical Oscillations, Waves, and Turbulence* (Springer, Berlin, 1984).

[16] H. Mori and Y. Kuramoto, *Dissipative Structures and Chaos* (Springer, Berlin, 1998).

[17] A. M. Turing, *Phil. Trans. R. Soc. London B*, **237**, 37 (1952).

[18] A. N. Zaikin and A. M. Zhabotinsky, *Nature*, **225**, 535 (1970).

[19] R. Kapral and K. Showalter, *Chemical Waves and Patterns* (Kluwer Academic, Dordrecht, 1995).

[20] Y. Hayase, S. Wehner, J. Kuppers, and H. R. Brand, *Phys. Rev. E*, **69**, 021609 (2004).

[21] G. N. Mercer and R. O. Weber, *Proc. R. Soc. Lond. Ser. A*, **453**, 1543 (1997).

[22] Q. Ouyang and H. L. Swinney, *Nature*, **352**, 610 (1991).

[23] V. Castets, E. Dulos, J. Boissonade, and P. de Kepper, *Phys. Rev. Lett.*, **64**, 2953 (1990).

[24] V. K. Vanag and I. R. Epstein, *Science*, **294**, 835 (5543).

[25] K. I. Agladze and V. I. Krinsky, *Nature*, **296**, 424 (1982).

[26] J. D. Murray, *Mathematical Biology* (Springer, Berlin, 1989).

[27] S. Kondo and R. Arai, *Nature*, **376**, 765 (1995).

[28] H. Meinhardt, *Physica D*, **199**, 264 (2004).

[29] A. Hodgkin and A. Huxley, *J. Physiol.*, **117**, 500 (1952).

[30] S. W. Kuffler and J. G. Nicholls, *From Neuron to Brain: A Cellular Approach to the Function of the Nervous System*, (Sinauer Associates, Sunderland, 1984).

[31] R. FitzHugh, *J. Gen. Physiol.*, **43**, 867 (1960).

[32] R. FitzHugh, *Biophys. J.*, **1**, 445 (1961).

[33] J. Nagumo, S. Arimoto, and S. Yoshizawa, *Proc. IRE*, **50**, 2061 (1962).

[34] R. R. Aliev and K. I. Agladze, *Physica D*, **50**, 65 (1991).

[35] F. Gauffre, V. Labrot, J. Boissonade, P. de Kepper, and E. Dulos, *J. Phys. Chem. A*, **107**, 4452 (2003).

[36] O. Steinbock and S. C. Müller, *J. Phys. Chem. A*, **102**, 6485 (1998).

[37] K. Yoshikawa, R. Aihara, and K. I. Agladze, *J. Phys. Chem. A*, **102**, 7649 (1998).

[38] R. Aihara and K. Yoshikawa, *J. Phys. Chem. A*, **105**, 8445 (2001).

[39] A. T. Schaefer, M. E. Larkum, B. Sakmann, and A. Roth, *J. Neurophysiol.*, **89**, 3143 (2003).

[40] P. Vetter, A. Roth, and M. Häusser, *J. Neurophysiol.*, **85**, 926 (2001).

[41] M. Häusser, N. Spruston, and G. J. Stuart, *Science*, **290**, 739 (2000).

[42] V. Gáspár, G. Bazsa, and M. T. Beck, *Z. Phys. Chem.*, **264**, 43 (1983).

[43] L. Kuhnert, *Nature*, **319**, 393 (1986).

[44] L. Kuhnert, K. I. Agladze, and V. I. Krinsky, *Nature*, **337**, 244 (1989).

[45] T. Amemiya, T. Ohmori, and T. Yamaguchi, *J. Phys. Chem. A*, **104**, 336 (2000) .

[46] R. J. Field, E. Körös, and R. M. Noyes, *J. Am. Chem. Soc.*, **94**, 8649 (1972).

[47] R. J. Field and R. M. Noyes, *J. Chem. Phys.*, **60**, 1877 (1972).

[48] J. J. Tyson and P. C. Fife, *J. Chem. Phys.*, **73**, 2224 (1980).

[49] A. B. Rovinsky and A. M. Zhabotinsky, *J. Phys. Chem.*, **88**, 6081 (1984).

[50] L. E. Scriven and C. V. Sternling, *Nature*, **187**, 186 (1960).

[51] H. Linde, P. Schwartz, and H. Wilke, in *Dynamics and Instability of Fluid Interfaces*, ed. T. S. Sφrensen, (Springer-Verlag, New York, 1979).

[52] P.-G. de Gennes, F. Brochard-Wyart, D. Quéré, *Capillarity and wetting phenomena: drops, bubbles, pearls, waves* (Springer, New York, 2004).

[53] K. Yoshikawa, T. Kusumi, M. Ukitsu, and S. Nakata, *Chem. Phys. Lett.*, **211**, 211 (1993).

[54] H. Miike, S. C. Müller, and B. Hess, *Chem. Phys. Lett.*, **144**, 515 (1988).

[55] H. Miike, S. C. Müller, and B. Hess, *Phys. Rev. Lett.*, **61**, 2109 (1988).

[56] H. Miike, S. C. Müller, and B. Hess, *Phys. Lett. A*, **141**, 25 (1989).

[57] J. A. Pojman and I. R. Epstein, *J. Phys. Chem.*, **94**, 4966 (1990).

[58] H. Miike and S. C. Müller, *Chaos*, **3**, 21 (1993).

[59] K. Matthiessen and S. C. Müller, *Phys. Rev. E*, **52**, 492 (1995).

[60] H. Wilke, *Physica*, **86D**, 508 (1995).

[61] K. Matthiessen, H. Wilke, and S. C. Müller, *Phys. Rev. E*, **53**, 6056 (1996).

[62] T. Sakurai, H. Miike, E. Yokoyama, and S. C. Müller, *J. Phys. Soc. Jpn.*, **66**, 518 (1997).

[63] T. Sakurai, E. Yokoyama, and H. Miike, *Phys. Rev. E*, **56**, 2367 (1997).

[64] L. M. Pismen, *Phys. Rev. Lett.*, **78**, 382 (1997).

[65] H. Miike, L. Zhang, T. Sakurai, and H. Yamada, *Pattern Recog. Lett.*, **20**, 451 (1999).

[66] R. J. Field and M. Burger, *Oscillations and Traveling Waves in Chemical Systems* (John Wiley & Sons, New York, 1985).

[67] R. J. Kaner and I. R. Epstein, *J. Am. Chem. Soc.*, **100**, 4073 (1978).

[68] A. A. Amsden and F. H. Harlow, *J. Comp. Phys.*, **6**, 322 (1970).

[69] R. Yoshida, T. Takahashi, T. Yamaguchi, and H. Ichijo, *J. Am. Chem. Soc.*, **118**, 5134 (1996).

[70] Y. Hara and R. Yoshida, *J. Phys. Chem. B*, **109**, 9451 (2005).

[71] S. Rybalko, N. Magome, and K. Yoshikawa, *Phys. Rev. E*, **70**, 046301 (2004).

[72] L. Rayleigh, *Proc. R. Soc. London*, **47**, 364 (1890).

[73] S. Nakata, Y. Iguchi, S. Ose, M. Kuboyama, T. Ishii, and K. Yoshikawa, *Langmuir*, **13**, 4454 (1997).

[74] M. Nagayama, S. Nakata, Y. Doi, and Y. Hayashima, *Physica D*, **194**, 151 (2004).

[75] J. Thomson, *Phil. Mag.*, **10**, 330 (1855).

[76] J. B. Fournier and A. M. Cazabat, *Europhys. Lett.*, **20**, 517 (1992).

[77] V. I. Kovalchuk, H. Kamusewitz, D. Vollhardt, and N. M. Kovalchuk, *Phys. Rev. E*, **60**, 2029 (1999).

[78] N. M. Kovalchuk and D. Vollhardt, *J. Phys. Chem. B*, **104**, 7987 (2000).

[79] N. M. Kovalchuk, V. I. Kovalchuk, and D. Vollhardt, *Colloids Surfaces A*, **198**, 223 (2002).

[80] F. D. dos Santos and T. Ondarçuhu, *Phys. Rev. Lett.*, **75**, 2972 (1995).

[81] P. G. de Gennes, *Physica A*, **249**, 196 (1998).

[82] N. Magome and K. Yoshikawa, *J. Phys. Chem.*, **100**, 19102 (1996).

[83] K. Yoshikawa and N. Magome, *Bull. Chem. Soc. Jpn.*, **66**, 3352 (1993).

[84] Y. Sumino, N. Magome, T. Hamada, and K. Yoshikawa, *Phys. Rev. Lett.*, **94**, 068301 (2005).

[85] Á. Tóth and K. Showalter, *J. Chem. Phys.*, **103**, 2058 (1995).

[86] Á. Tóth, V. Gaspar, and K. Showalter, *J. Phys. Chem.*, **98**, 522 (1994).

[87] J. Masere, D. A. Vasquez, B. F. Edwards, J. W. Wilder, and K. Showalter, *J. Phys. Chem.*, **98**, 6505 (1994).

[88] J. J. Tyson, in *Oscillations and Traveling Waves in Chemical Systems*, eds. R. J. Field and M. Burger (Wiley: New York, 1985).

[89] T. Amemiya, M. Nakaiwa, T. Ohmori, and T. Yamaguchi, *Physica D*, **84**, 103 (1995).

[90] S. Kádár, J. Wang, and K. Showalter, *Nature*, **391**, 770 (1998).

[91] K. Agladze, Á. Tóth, T. Ichino, and K. Yoshikawa, *J. Phys. Chem. A*, **104**, 6677 (2000).

[92] H. Nagahara, T. Ichino, and K. Yoshikawa, *Phys. Rev. E*, **70**, 036221 (2004).

[93] A. T. Winfree, *The Geometry of Biological Time* (Springer-Verlag, Berlin, 1978).

[94] N. G. Rambidi, K. E. Shamayaev, and G. Y. Peshkov, *Phys. Lett. A*, **298**, 375 (2002).

[95] T. Sakurai, E. Mihaliuk, F. Chirila, and K. Showalter, *Science*, **296**, 2009 (2002).

[96] I. Motoike and K. Yoshikawa, *Phys. Rev. E*, **59**, 5354 (1999).

[97] O. Steinbock, P. Kettunen, and K. Showalter, *J. Phys. Chem.*, **100**, 18970 (1996).

[98] T. Ichino, Y. Igarashi, I. N. Motoike, and K. Yoshikawa, *J. Chem. Phys.*, **118**, 8185 (2003).

[99] J. Gorecka and J. Gorecki, *Phys. Rev. E*, **67**, 067203 (2003).

[100] A. Lázár, Z. Noszticzius, H. -D. Försterling, and Z. Nagy-Ungvarai, *Physica D*, **84**, 112 (1995).

[101] O. Steinbock, P. Kettunen, and K. Showalter, *Science*, **269**, 1857 (1995).

[102] I. N. Motoike, K. Yoshikawa, Y. Iguchi, and S. Nakata, *Phys. Rev. E*, **63**, 036220 (2001).

[103] D. Winston, M. Arora, J. Maselko, V. Gáspár, and K. Showalter, *Nature*, **351**, 132 (1991).

[104] Y. Iguchi, R. Takitani, Y. Miura, and S. Nakata, *Rec. Res. Devel. Pure Appl. Chem.*, **2**, 113 (1998).

[105] K. Agladze, R. R. Aliev, T. Yamaguchi, and K. Yoshikawa, *J. Phys. Chem.*, **100**, 13895 (1996).

[106] S. C. Müller, T. Plesser, and B. Hess, *Physica D*, **24**, 87 (1987).

[107] A. Volford, P. L. Simon, H. Farkas, and Z. Noszticzius, *Physica A*, **274**, 30 (1999).

[108] A. Lázár, Z. Noszticzius, H. Farkas, and H. D. Försterling, *Chaos*, **5**, 443 (1995).

[109] A. Lázár, H. -D. Försterling, H. Farkas, P. Simon, A. Volford, and Z. Noszticzius, *Chaos*, **7**, 731 (1997).

[110] S. Nakata, S. Morishima, and H. Kitahata, *J. Phys. Chem. A*, in press.